Evolving Morphology and Excited State Dynamics During Deposition and Thermal Annealing of Organic Thin Films

by

Zachary Scott Walbrun

A dissertation accepted and approved in partial fulfillment of the

requirements for the degree of

Doctor of Philosophy

in Chemistry

Dissertation Committee:

George V. Nazin, Chair

Cathy Y. Wong, Advisor

Tanya Gupta, Core Member

Benjamin J. McMorran, Institutional Representative

University of Oregon

Spring 2025

© 2025 Zachary Scott Walbrun
All rights reserved.

DISSERTATION ABSTRACT

Zachary Scott Walbrun

Doctor of Philosophy in Chemistry

Title: Evolving Morphology and Excited State Dynamics During Deposition and Thermal Annealing of Organic Thin Films

Understanding the structure-function relationship for organic semiconducting materials is critical for developing more efficient organic photovoltaics (OPVs). Charge transfer takes place at the electron donor-acceptor interface and is highly dependent on film morphology. Since organic molecules have weak intermolecular forces, a variety of molecular orientations form when cast into films, which can impact OPV performance. Thermal annealing is a typical post-processing method used to improve sample crystallinity. This thesis first reports on thermal annealing of the prototypical donor-acceptor system, Poly(3-hexylthiophene-2,5-diyl) (P3HT): phenyl-C61-butyric acid methyl ester (PCBM) using in situ linear absorbance and single-shot transient absorption (SSTA). A sequential decay model revealed two different species in neat P3HT films with differing interchain ordering, where the species with less interchain ordering undergoes irreversible changes during thermal annealing. In P3HT:PCBM films, charge transfer increases significantly after passing through the glass transition temperature. This study shows the basis for studying how charge transfer evolves in a nonequilibrium system.

Squaraine (SQ) molecules have a donor-acceptor-donor (D-A-D) structure that leads to inhanced CT. In this study, an inert polymer was used to impede SQ aggregation, allowing for in situ spectroscopic studies of molecular aggregation

during thermal annealing. In situ linear absorption and SSTA measurements during thermal annealing were used to reveal the changes in electronic structure and excited-state dynamics. A sequential decay kinetic model showed that energy transfer occurs between uncoupled and weakly-coupled monomers before annealing and energy transfer occurs between sub-populations of slip-stacked H-aggregates after annealing. We further use an ICT Hamiltonian model to predict the intermolecular spacing and intermolecular charge transfer probability as a function of aggregation. This model shows great promise in predicting both the species present and predicting excitonic behavior for applications in OPVs.

Copper phthalocyanine (CuPc), an electron donor molecule, forms crystallites in a pyramidal structure when cast as a thin film, but the mechanism of aggregation is not yet fully understood. In this work, in situ linear absorption and SSTA measurements revealed a novel intermediate stage during CuPc film deposition. Supersaturated solutions of CuPc showed that the steps of aggregation can be separated with H-aggregates forming in solution and J-aggregates forming in final step of solution evaporation. Films cast from solutions of supersaturated CuPc have a more crystalline structure and global fits to the TA spectra showed that exciton-exciton annihilation becomes more rapid compared to regular films. This study provides the framework for how in situ spectroscopies can be used to design new aggregate structures and control exciton dynamics.

Recent studies of high school / freshman chemistry laboratories show that online activities show some benefit, reducing the number of errors made in the lab and improving scores on post-lab questions. However, their impact on upper division chemistry laboratories have not been investigated. In this three-year study, we measured the impact of interacting with a computer simulation

before an in-lab activity constructing a brightfield microscope in an upper-division physical chemistry laboratory. Students recorded their completion times for activities performed during the laboratory and took the Meaningful Learning in the Laboratory Instrument (MLLI) survey before and after building the microscope. The MLLI measured the students' affective and cognitive experiences before and after the activity. Analysis of completion times showed that students performed the lab activities slightly faster with a narrower distribution of completion times when they had interacted with the simulation beforehand. Analysis of specific survey questions from the MLLI revealed that the students who completed the computer simulation before building the microscope were less worried about making mistakes and finishing on time. This study shows that while a simulation of in-lab activities may not provide any cognitive benefit to students, it may improve their confidence in the laboratory. This thesis includes previously published and unpublished coauthored material.

CURRICULUM VITAE

NAME OF AUTHOR: Zachary Scott Walbrun

GRADUATE AND UNDERGRADUATE SCHOOLS ATTENDED:

University of Oregon, Eugene, OR, USA
University of Wisconsin Eau Claire, Eau Claire, WI, USA

DEGREES AWARDED:

Doctor of Philosophy, Chemistry, 2025, University of Oregon
Bachelor of Science, Chemistry, 2019, University of Wisconsin Eau Claire
Bachelor of Science, Mathematics, 2019, University of Wisconsin Eau Claire

AREAS OF SPECIAL INTEREST:

Organic Thin Films
Ultrafast Spectroscopy
Spectral and Kinetic Modeling

PROFESSIONAL EXPERIENCE:

Graduate Teaching Fellow, University of Oregon, 2019-2025
General Chemistry Lecture Instructor, University of Oregon, Winter 2025

GRANTS, AWARDS AND HONORS:

Emanuel Optical, Molecular, and Quantum Sciences Scholarship, Spring 2025
Department Award for Excellence in the Teaching of Chemistry (Physical Chemistry Lab), 2022-2023
American Chemical Society Physical Chemistry Award, Spring 2019
L.A. Ochrymowycz- Alfred Bader Chemistry Scholarship, Spring 2018
Outstanding Freshman Chemistry Award, Spring 2017
Wisconsin Academic Excellence Award, Spring 2016

PUBLICATIONS:

Walbrun, Z. S.; Nawab, L.; Wong, C. Y. Pre-Lab Simulation of Microscope Building in Upper Division Laboratory Improves Student Confidence. 2025, In progress.

Walbrun, Z. S.; Paulson, A. Y.; Frainey, N. F.; Bodle, W. L.; Wong, C. Y. Novel Intermediate Phase During Film Deposition of Copper Phthalocyanine Revealed with In Situ Spectroscopies. 2025, In progress.

Walbrun, Z. S.; Fisher, R. V.; Wong, C. Y. Evolution of Charge Transfer During Thermal Annealing of a Polymer:Fullerene Thin Film. 2025, Submitted.

Walbrun, Z. S.; Hoban, Á. R.; Paulson, A. Y.; Wiegand, T. J.; Collison, C. J.; Wong, C. Y. Morphology-Dependent Excited-State Dynamics of Squaraine Thin Films during Thermal Annealing. J. Phys. Chem. Lett. 2025, 4456–4462. https://doi.org/10.1021/acs.jpclett.5c00851.

Walbrun, Z. S.; Wong, C. Y. In Situ Transient Absorption During Thermal Annealing of a Polymer: Fullerene Blend. In Frontiers in Optics + Laser Science 2023 (FiO, LS); Optica Publishing Group: Tacoma, Washington, 2023; p JTu5A.8. https://doi.org/10.1364/FIO.2023.JTu5A.8.

Hoban, Á. R.; Walbrun, Z. S.; Wong, C. Y. Aggregation-Dependent Excited-State Dynamics of an Organic Dye Targeted for Photovoltaics. In Frontiers in Optics + Laser Science 2023 (FiO, LS); Optica Publishing Group: Tacoma, Washington, 2023; p JTu5A.10. https://doi.org/10.1364/FIO.2023.JTu5A.10.

Frainey, N. M.; Walbrun, Z. S.; Wong, C. Y. Investigating Aggregation and Excited State Dynamics During Deposition of a Phthalocyanine:Fullerene System. In Frontiers in Optics + Laser Science 2023 (FiO, LS); Optica Publishing Group: Tacoma, Washington, 2023; p JTu5A.9. https://doi.org/10.1364/FIO.2023.JTu5A.9.

Walbrun, Z. S.; Wong, C. Y. In Situ Measurement of Evolving Excited-State Dynamics During Deposition and Processing of Organic Films by Single-Shot Transient Absorption. Annu. Rev. Phys. Chem. 2023, 74 (1), 267–286. https://doi.org/10.1146/annurev-physchem-102722-041313.

Walbrun, Z. S.; Leibfried, L. C.; Hoban, Á. R.; Rasmussen, B. C.; Wiegand, T. J.; Collison, C. J.; Wong, C. Y. Effect of Thermal Annealing on Aggregation of a Squaraine Thin Film. *MRS Advances* **2022**, *7* (12), 239–244. https://doi.org/10.1557/s43580-022-00215-4.

Wilson, K. S.; Walbrun, Z. S.; Wong, C. Y. Single-Shot Transient Absorption Spectroscopy Techniques and Design Principles. *Spectrochim Acta A Mol Biomol Spectrosc* **2021**, *253*, 119557. https://doi.org/10.1016/j.saa.2021.119557.

ACKNOWLEDGEMENTS

Graduate school has been quite a journey and I have so many people to thank for getting me to this point. To my advisor, Cathy Wong, for being the best mentor I could possibly ask for. Through your guidance, I have grown not only scientifically, but also as a person. You've taught me how to be a better writer, think about problems scientifically, and how to help other graduate students. Graduate school and my future would not have been the same without your mentorship, so thank you for everything.

To Kara Pezzi, the reason this all began. Kara was my high school chemistry teacher who would do anything to help students. Chemistry was a struggle for me at first, but Kara would be at school before and after hours to help students with whatever they needed. She taught me all the joys of chemistry and even if it was a struggle, I shouldn't give up. Thank you Kara for everything.

To all the students that I've mentored and taught over the 6 years - I've truly enjoyed every moment. Teaching holds a special place in my heart and it helped get me through graduate school. Thank you.

To everyone in the Wong lab over the years - you all have been like family for me. I wouldn't be here without all of you. To Marty - it was so fun working with you and doing nanocrystal syntheses during my rotation. I'm really glad that I got to know you and become so close to you. You've been there for some of the hardest and most frustrating moments of grad school and I appreciate you so much for that. To Laila - thank you for really bringing the lab back together after COVID and being there as the only other graduate student for two years. Both the lab and I wouldn't be how they are without you. To Alyssa and Racheal - it's

been an absolute joy mentoring both of you, seeing you both thrive in the lab, and hearing all the jokes in the office. I'm really glad that both of you are here. I want to especially mention Laura and Áine, the squaraine squad. Third year of graduate school was really difficult for me and you both really kept me going. I'm really lucky to have both of you in my life.

To Tanya Gupta, I can't possibly put into words how much I appreciate you. Thank you for being such an amazing mentor over the course of my years as head TA and when I became instructor of record. I have truly learned so much from you and really enjoyed working with you. Thank you for always being so supportive of everything.

I have to take a second to acknowledge beverages. Parker - thank you for all the espresso, great chats, and fun spin classes over the years. I still think about the song with 8 blocks from the Hamza's class and how crazy that was. It's been an absolute joy and you've been a great friend. Dario - the crisp beverages got us through so much. I've always enjoyed our chats about teaching and random memes. Thanks for being such a great friend.

To my parents, brother, and Jackson, you all got to hear it all. The late nights grading, working on papers, dealing with failed experiments, and troubleshooting code for weeks. Especially all the late night calls with my parents when they were trying to go to bed. Thank you for dealing with it all, it means more than you could possibly put into words.

This thesis is dedicated to my parents. I couldn't have done this without all of your support over the years.

TABLE OF CONTENTS

Chapter Page

I. INTRODUCTION 23

1.1. Organic Semiconductors 23

1.2. Donor-Acceptor Systems 24

1.3. Solution Processing and Morphology 26

1.3.1. Solution Processing 26

1.3.2. Post-Processing Techniques 28

1.3.3. Morphology and Electronic Structure 29

1.4. Spectroscopic Measurements 32

1.4.1. Transient Absorption 34

1.4.2. Single-Shot Transient Absorption 36

1.4.2.1. Time Delay and Resolution 38

1.4.2.2. Pulse Energy 40

1.4.2.3. Beam Flattening 42

1.4.2.4. Dynamic Background Correction 45

1.4.2.5. Spatial Heterogeneity 47

1.4.3. Summary 48

II. THERMAL ANNEALING OF DONOR-ACCEPTOR BLEND FILMS 49

2.1. Experimental Details 52

2.2. Neat P3HT Films 54

2.2.1. Linear Absorption 54

2.2.2. Single-Shot Transient Absorption 55

2.2.3. Kinetic Modeling 56

Chapter Page

2.3. P3HT:PCBM Films 60
2.3.1. Linear Absorption 60
2.3.2. Single-Shot Transient Absorption 61
2.3.3. Kinetic Modeling 61
2.4. Summary 62
III. THERMAL ANNEALING OF DONOR-ACCEPTOR-DONOR FILMS 64
3.1. $DHSQ(OH)_2$ 67
3.1.1. Experimental Details 67
3.1.2. Linear Absorption 67
3.1.3. Single-Shot Transient Absorption 67
3.1.4. Kinetic Modeling 69
3.2. $DBSQ(OH)_2$ 75
3.2.1. Experimental Details 75
3.2.2. Linear Absorption 75
3.2.3. Single-Shot Transient Absorption 77
3.2.4. Kinetic Modeling 78
3.2.5. Intermolecular Charge Transfer Hamiltonian 83
3.2.6. Summary 90
IV. FILM DEPOSITION 92
4.1. Copper Phthalocyanine 92
4.1.1. Experimental Details 94
4.1.2. Results 95
4.1.3. Summary 103
V. PHYSICAL CHEMISTRY LABORATORY STUDY 104
5.1. Experimental 106

Chapter Page

5.2. Results 108

5.3. Summary 112

APPENDICES

A. PUMP POWER CALCULATION 114

B. SUPPLEMENTAL INFORMATION FOR MICROSCOPY STUDY 116

B.1. Year 1 Tutorial Worksheet 116

B.2. In-Lab Procedure 118

B.3. Simulation Procedure 128

B.4. Surveys 135

REFERENCES CITED 140

LIST OF FIGURES

Figure Page

1. (a) HOMO-LUMO diagram for an electron donor (blue) and electron acceptor (orange). Side view of electron donor (blue) and electron acceptor (orange) deposited on a substrate (grey) in a (b) bilayer, (c) bulk heterojunction, and (d) intercalated bilayer. 26

2. Film deposition techniques. Solid orange and dashed orange arrows represent solution deposition and solvent evaporation, respectively, while red arrows show motion of deposition apparatus. 28

3. Linear absorption spectra of P3HT films spin coated from a solution of 10 mg/mL (red), 5 mg/mL (blue), and drop casted from a solution of 0.2 mg/mL (black). 29

4. Orientation of parallel transition dipole moments with angle, θ. 30

5. Energy diagram showing the energy level splitting resulting from (a) J-aggregates, (b) H-aggregates, and (c) oblique aggregates. Transitions to a dark and bright state are indicated with dashed arrow with red x and solid arrows, respectively. 30

6. Simulated absorbance spectra using the Holstein-like Hamiltonian for monomers (black), J-aggregates (red), and H-aggregates (blue). The following parameters were used for the simulation: 2 molecules, 4 total vibrational quanta, $\epsilon_0 = 12000$ cm^{-1}, $\omega_0 = 1300$ cm^{-1}, $\lambda^2 = 0.5$. The coupling J_{mn} was 0 cm^{-1} for monomers, -500 cm^{-1} for J-aggregates, and 500 cm^{-1} for H-aggregates. 31

7. Cartoon of possible TA signals. 37

Figure Page

8. SSTA apparatus. Ti:Sa, titanium:sapphire laser; BS, beam splitter; OPA, optical parametric amplifier; PC, prism compressor; CHP, optical chopper; RR, retroreflector; Ar(g), pressurized argon gas cell; SLM, spatial light modulator; CYL, cylindrical lens. Sample stage shown in blue. 37

9. Angled beams (a) or echelon optics (b) can be used to spatially encode the time delay between the pump (blue) and probe (grey), with dashed lines showing the beam propagation direction. 38

10. (a) Schematic illustrating parameters that determine time delay. Pump-probe time delay is different at the top and bottom of a column of sample that is measured using a single detector pixel, resulting in loss of time resolution. (b) Time range for three different overlap line lengths at the sample and (c) time smear for three different film thicknesses as a function of angle between the pump and probe pulse. 39

11. (a) White light spectrum generated from an argon tube at a differential pressure of 0.56 bar. (b) Corresponding percent standard deviation. 42

12. (a) Intensity of a Gaussian spatial beam profile can be redistributed into a flat-top profile using an SLM. (b) Pump beam focused to the sample plane using a cylindrical lens. Inset shows a top-down view of the bowtie shape at the sample plane. (c) Pump beam imaged with fluorescent sample showing initial bowtie shape (black) and after imparting variable focal length (grey). 44

13. (a) Stage and film temperature as a function of time. (b) Linear absorption spectra of a P3HT film at the temperatures indicated by colored markers in (a). (c) Peak positions during annealing and cooling from Gaussian fitting. 54

14. SSTA spectra of a P3HT film measured during (a) heating at 30°C, (b) 140°C, and (c) cooling at 30°C. (d), (e), and (f) show spectral slices from (a), (b), (c), respectively. 56

Figure Page

15. Globally fit EADS to SSTA measurements of P3HT films during annealing and cooling using Equation 2.1. (a) A_1 and (e) A_2 as a function of heating. (b) and (f) show slices from (a) and (e) at temperatures given by color. 0-0:0-1 ratios for (c) A_1 and (g) A_2 as a function of annealing and cooling. (d) Short and (h) long time constant as a function of heating and cooling. 57

16. (a) Linear absorbance spectra for a film of neat P3HT (blue) and 1:8 P3HT:PMMA (red). (b) Schematic indicating J- and H-aggregates in bulk P3HT. 58

17. Linear absorbance spectra for pre-annealed (blue, solid) and non-pre-annealed (red, dashed) P3HT films (a) before and (b) after annealing. 59

18. Globally fit EADS to SSTA measurements of P3HT films that began as pre-annealed during annealing and cooling using Equation 2.1. (a) A_1 and (e) A_2 as a function of heating and cooling. (b) and (f) show slices from (a) and (e) at temperatures given by color. 0-0:0-1 ratios for (c) A_1 and (g) A_2 as a function of annealing and cooling. (d) Short and (h) long time constant as a function of heating and cooling. 59

19. (a) Linear absorption spectra of a P3HT:PCBM film during heating and cooling. Peak (b) positions and (c) amplitudes as a function of time from Gaussian fitting. 60

20. SSTA spectra of a P3HT:PCBM film measured during (a) heating at 30°C , (b) 140°C, and (c) cooling at 30°C. (d), (e), and (f) show spectral slices from (a), (b), (c), respectively. 61

21. Globally fit EADS to SSTA measurements of P3HT:PCBM films during heating and cooling using Equation 2.1. (a) A_1 and (d) A_2 as a function of heating and cooling. (b) and (e) show slices from (a) and (d) at temperatures given by color. (d) Short and (h) long time constant as a function of heating and cooling. 62

22. Linear absorbance spectra for DBSQ$(OH)_2$:PMMA films with varying wt% SQ and corresponding cartoons. 66

Figure Page

23. (a) Temperature ramp of stage (black) and top surface of a glass slide (grey). Triangles indicate when spectroscopic measurements were conducted. (b) A film (blue) on a heated sample stage with slit that allows pump (black) and probe (purple) to pass. (c) Pump spectrum (black) overlaid with absorbance of DHSQ(OH)$_2$:PMMA film at 2 min (blue) and 58 min (red). 68

24. SSTA measured at (a) 2 min and (b) 58 min. Above, spectral slices at pump-probe time delays of 0.2-0.5 ps, 14.5-15.5 ps, and 49.5-50.5 ps. On the right, transients at 560 nm, 610 nm, and 640 nm. 69

25. The kinetic model for (a) uncoupled and weakly-coupled monomers, (b) uncoupled, weakly-coupled, and pi-stacked molecules, (c) isolated pi-stacked molecules. States with lower oscillator strength shown in dashed lines. Cartoons illustrate the species present. Higher energy excited states that do not participate in the kinetic model but are bleached in the calculated TA spectra are also pictured. Model parameters reported in text. The grey dashed arrows indicate transitions that were excited by the 640 nm pump pulse. 72

26. SSTA spectra measured at 2 min (pre-annealing, blue) and 58 min (post-annealing, red). (b) Simulated spectra at the same pump-probe time delays. The same parameters were used for shared transitions in multiple models: $\tau^{u}_{1-0} = 40$ ps, $\tau^{w}_{1-0} = 500$ ps, $\tau^{\pi}_{1-0} = 60$ ps, $\tau_{u-w} = 5$ ps, $\tau_{u-\pi} = 5$ ps. Weights of model 1 : model 2: model 3 are 0.47:0.29:0.24 at 2 min and 0.00:0.30:0.70 at 58 min. 74

27. (a) Structure of DBSQ(OH)$_2$ (R=Bu) with the electron accepting squarylium ring in orange and the nitrogen-containing electron donating arms in blue. (b) Heating stage temperatures (black) and slide temperatures (grey) are plotted over annealing time. Scans marked with colored diamonds in (b) at 100°C (pink), 125°C (orange), 135°C (gold), 140°C (green), 145°C (blue), 155°C (purple) correspond to linear absorption of an 8% wt SQ film in panel (c). (d) Cartoon of uncoupled monomer, weakly-coupled monomer, and slip-stacked H-aggregate at three different temperatures. 76

28. SSTA of an 8% wt SQ film taken at 2 min, 100°C (a) and at 53.5 min, 160°C (c) during thermal annealing. Transients from (a) are plotted at 540 nm (red), 600 nm (orange), and 670 nm (blue) in (b). Transients from (c) are plotted at 540 nm (red), 600 nm (orange), and 655 nm (blue) in (d). Data were logarithmically binned into 100 bins along the time delay axis. Fits to transients (dashed black) start at 400 fs. 79

29. A_1 (a) and A_2 (d) from EADS fits of SSTA data from a low weight percent SQ film as a function of annealing time. Spectral slices from (a,d) are plotted at 7 min, 110°C (blue), 28.5 min, 130°C (orange), and 52 min, 160°C (red) in panels (b,e). Corresponding time constants from A_1 (c) and A_2 (f) as a function of annealing time. 81

30. Cartoon of neutral and ionic adiabatic basis states. 83

31. Energy of the HA (black) and CT (grey) states as a function of interplanar spacing (z), before mixing with the intermolecular charge transfer term. 87

32. Linear absorbance data (a) and fits from the ICT Hamiltonian (b) shown from 27 min (100°C) to 53.5 min (160°C). Slices from (a,b) are plotted at 32 min, 110°C (blue) and 47 min, 155°C (green) in (c). Fits are shown as a dashed black trace compared to the data. (d) Slip-stacked SQ dimer cartoon with listed Cartesian axis and arm length (l). (e) Interplanar spacing and (f) intermolecular charge transfer integral as a function of thermal annealing. 88

33. (a) Linear absorbance, (b) A_1, (c) A_2 measured at 52 min (160°C). Fits of ICT Hamiltonian (grey) to measured spectra (black) provide interplanar spacing of 4.98 Å, 6.15 Å, and 4.76 Å, respectively. 89

34. Fit from ICT Hamiltonian for linear absorption data at 53.5 min with the broadening as best fit of 24 nm (grey) and broadening decreased to 12 nm (black). Peak at 590 nm not observed in linear absorption spectrum due to overlap of peaks. 90

Figure Page

35. (a) Cartoon depiction of CuPc (blue rectangles) nanoribbon growth. Arrows represent face-on growth with different interactions with the edges of the CuPc molecules. Purple – glass interaction, orange – glass and side-side interaction, red – side-side interaction. (b) In situ linear absorption during the solution (pink), intermediate (orange), and film (green) stages. Chemical structure of CuPc inset. 96

36. SSTA spectra from (a) 30 s, (b) 70 s, (c) 110 s during deposition binned over six pixels on the time delay axis. Spectral slices from (a), (b), and (c) shown in (d), (e), and (f), respectively. 97

37. (a) In situ mass measurements during film deposition. A larger substrate and volume of solution was used, leading to a longer deposition time. Linear absorption spectra were taken concurrently to identify the stage as solution (orange), intermediate (purple), or film (blue). (b) Linear absorption spectra at times given by markers in (a) and for the film stage (blue). 98

38. AFM images of CuPc films cast from (a) 0.5 mg/mL and (b) supersaturated solutions. 99

39. Linear absorbance spectra of (a) supersaturated solution (black) overlayed with the thin film cast from supersaturated solutions (blue) and (b) the regular thin film (red) and the thin film cast from supersaturated solutions (blue). (c) Relationship between the peak wavelength of the higher energy peak and the concentration of the CuPc solution prior to casting. Brickstone packing structure inset. 99

40. TA spectra of (a) normal CuPc films and (b) supersaturated CuPc films. (c) and (d) show spectral slices from (a) and (b), respectively. 102

41. Global fit amplitudes for films cast from a (a) 0.5 mg/mL and (b) supersaturated solution. 102

42. (a) Microscope from in-lab activity. (b) Image from microscopy simulation showing rays of light (red lines) after passing through lenses (blue). Sample plane shown as a blue line. 107

Figure Page

43. (a) Worksheet grade and (b) total time on in-lab activities for no simulation and simulation groups. Mean and median indicated with circle and x, respectively. Error bars represent one standard deviation from the mean. 109

44. Time spent on sections c (4f imaging system), d (collecting light from the lamp), e (setting up Köhler illumination), and g (wavelength dependence of focal point and resolution) for no simulation versus simulation. Mean and median indicated with circle and x, respectively. Error bars represent one standard deviation from the mean. 110

45. Box and whisker plots for (a) MLLI Q2 (to worry about finishing on time), (b) MLLI Q9 (to be nervous about making mistakes), and (c) MLLI Q18 (to get nervous when handling equipment) after the in-lab activity for the no simulation versus simulation group. Ratings are given as 1 = disagree and 10 = agree. 111

46. Box and whisker plots of additional survey questions A-G given after the in-lab activity for the simulation group. Outliers lie 1.5 times the interquartile range away from the edges of the box and are represented by circles. 112

B.1. Rail that ensures horizontal alignment of your optics, with lamp and sample holder. 119

B.2. Optical elements you will use in this lab. 119

B.3. Optical elements that include lenses that you will use in this lab. 120

B.4. Parts needed to install an optic on the rail. 120

LIST OF TABLES

Table Page

1. EADS spectra fit parameters for ICT Hamiltonian. 89

2. Additional questions given to simulation group after in-lab activity. . . . 111

B.1. Lens radius and distance from lens to focal point. 129

B.2. Focal length dependence on wavelength 130

B.3. Survey before performing in-laboratory activities 136

B.4. Survey after performing in-laboratory activities 137

B.5. Survey item classification 138

B.6. Additional survey questions 139

CHAPTER I

INTRODUCTION

Includes material from:

Walbrun, Z. S.; Wong, C. Y. In Situ Measurement of Evolving Excited-State Dynamics During Deposition and Processing of Organic Films by Single-Shot Transient Absorption. *Annu. Rev. Phys. Chem.* **2023**, *74 (1)*, 267–286.

1.1 Organic Semiconductors

Organic semiconducting materials show great promise for organic photovoltaic (OPV) and organic light-emitting diode (OLED) applications owing to their solution processability, compatibility with flexible substrates, and chemical tunability.[1–6] Organic semiconductors are excitonic materials owing to their relatively low dielectric constants, with electron–hole binding energies in the hundreds of millielectron volts. Excitons are photogenerated in OPV materials, and the constituent electrons and holes must overcome their binding energy to become charge separated before they can migrate to electrodes. This is typically accomplished with a combination of organic materials, one an electron donor and the other an electron acceptor, so that excitons encountering an interface between these two materials may split to form a charge transfer state. This physical separation can lower the binding energy and promote further separation of charges. Conversely, charges are injected into an OLED device, and electrons and holes must migrate, meet, and recombine to emit a photon.[7] Thus, molecules in OLED devices are designed to promote photoluminescence (PL) by tuning spin-orbit coupling, the relative energies of singlet and triplet states, and the transition rates between them.[8,9] OLEDs have already reached viability and are competitive in the marketplace. OLEDs are already found in televisions and cell phones, leveraging

their energy efficiency, brightness, and large field of view. They are also thinner and lighter than traditional LEDs and can be deposited onto flexible plastic substrates, which may enable their usage in wearable electronics and health care devices such as biosensors and phototherapeutics.[10–12] Meanwhile, OPVs are just reaching commercial viability. The efficiency of OPVs has historically lagged behind other types of photovoltaics, with a slow rate of efficiency improvement[13] despite significant research efforts. However, the development of nonfullerene electron acceptors over the past decade is driving a rejuvenation of interest. The first single-junction OPV using a nonfullerene acceptor (NFA) to exceed the champion efficiency of a fullerene-based device was at 13.1% in 2017[14], and efficiencies have climbed rapidly since then, with an efficiency of 19.2% reported in 2022.[15]

1.2 Donor-Acceptor Systems

Typical organic semiconducting materials used in devices have either electron donating (D) or accepting character (A). When these materials are combined, electron donor molecules donate an electron to electron acceptor molecules. Materials can be classified as electron donating or accepting by comparing the energy levels of the highest occupied molecular orbital (HOMO) and the lowest unoccupied molecular orbital (LUMO), shown in **Figure 1a**. Both the HOMO and LUMO for the electron acceptor are lower in energy compared those of the electron donor.

When the donor or acceptor materials absorb a photon, an excited electron-hole pair (exciton) is created. The electron lies in the LUMO and the hole lies in the HOMO of the material that is photoexcited. This exciton may diffuse through the material and encounter a donor-acceptor interface. If the donor material is excited, the excited electron in the donor LUMO can transfer to the acceptor

LUMO. Conversely, if the acceptor is excited, the electron from the donor HOMO can transfer to the acceptor HOMO. Both scenarios are examples of charge transfer (CT), as the electron lies in the acceptor LUMO and the hole lies in the donor HOMO. If these charges can overcome Coulomb attraction, they can separate.

When electron donor and acceptor materials are cast separately, a bilayer (**Figure 1b**) is formed. A bulk heterojunction (**Figure 1c**) is formed if the materials are cast together. To optimize the donor-acceptor interfacial area while having larger domains, an intercalated bilayer (**Figure 1d**) can be formed. Controlling the morphology of the donor and acceptor layers can change the donor-acceptor interfacial area, which is critical for optimizing device efficiency. By controlling the morphology of this active layer, the rates of these processes can be changed. For example, using a bulk heterojunction or intercalated layer increases the donor-acceptor interfacial area compared to a bilayer, leading to an increased probability of forming a CT exciton.

One of the most common electron donor-acceptor systems is 3-hexylthiophene-2,5-diyl (P3HT):phenyl-C61-butyric acid methyl ester (PCBM), a blend of a polymer and a fullerene derivative. However, the highest reported efficiency was 5.5% for this system.[16] As typical fullerene-based acceptors have limited spectral absorption in the UV-visible spectrum and have limited tunability, NFAs have been synthesized and investigated. Since 2015, there have been major developments in the realm of NFAs, such as rylene diimides and fused-ring electron acceptors (FREAs). FREAs are molecules that contain two acceptor moieties and one donor moiety in an A-D-A structure. The use of a non-fullerene acceptor, ZY-4Cl, in conjunction with P3HT has increased the efficiency to 10.7%[17], showing that devices made with P3HT are still promising.

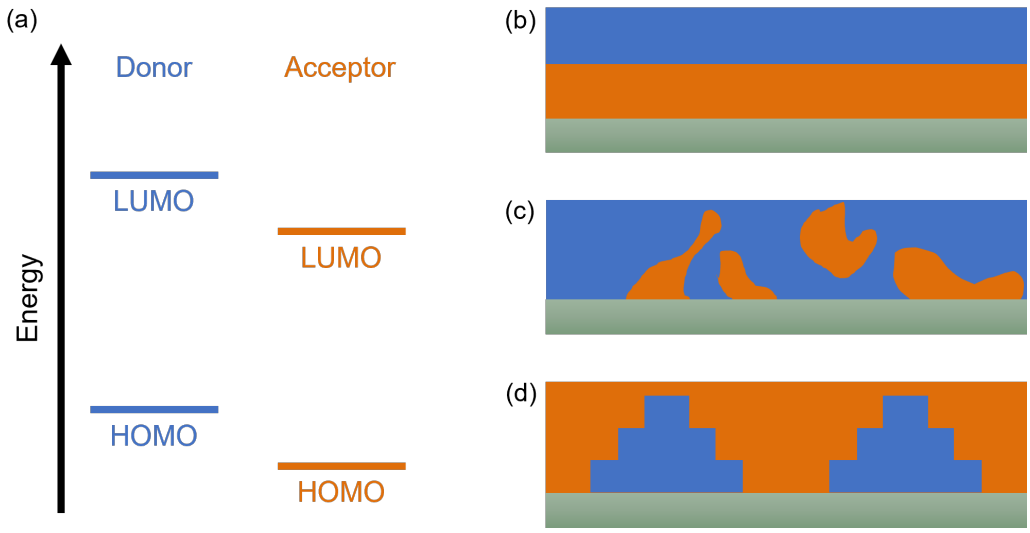


Figure 1. (a) HOMO-LUMO diagram for an electron donor (blue) and electron acceptor (orange). Side view of electron donor (blue) and electron acceptor (orange) deposited on a substrate (grey) in a (b) bilayer, (c) bulk heterojunction, and (d) intercalated bilayer.

Electron donor-acceptor-donor (D-A-D) molecules, such as squaraines (SQ) have electron donating and electron accepting moieties on the same molecule, leading to enhanced CT. One previous downfall of using organic semiconductors in PVs was the limited efficiency, but this has been improved with the introduction of electron donor-acceptor-donor and acceptor-donor-acceptor molecules. These organic molecules have been designed to absorb more of the sun's emission and be very planar which leads to increased pi-pi stacking, and thus greater efficiency.[18–21] An example of this kind of material is studied in **Chapter 3** and the concepts from this study will be useful and analogous to future work on A-D-A molecules.

1.3 Solution Processing and Morphology

1.3.1 Solution Processing. Solution processability is one of the primary potential benefits of organic semiconductors. A typical organic thin film has both amorphous and crystalline components that result from weak

intermolecular forces between organic molecules. If the solvent evaporates rapidly during film deposition, molecules may be kinetically trapped in a disordered and unstable configuration. The resultant film morphology is highly dependent on the solution preparation and film deposition technique.[22]

Some of the many methods that can be used to deposit solutions of organic semiconductors[22] are shown in **Figure 2**. Drop casting and spin coating are commonly used in academic research laboratories to produce small-area films. Drop casting involves casting a solution on a substrate and allowing the solvent to evaporate, oftentimes resulting in a coffee-ring effect[23] and nonuniform films. Drop cast films are formed over the course of seconds to hours, depending on deposition conditions such as temperature. If the deposition takes longer, molecules are able to adopt a thermodynamically preferred orientation during deposition. Spin coating, in which solution is deposited onto a spinning substrate and excess solution is flung away in seconds to leave a thin film, results in more uniform films[22,24], but a significant amount of solution is wasted. Dip coating involves dipping a substrate in a solution and withdrawing it at a constant rate. Printing processes using a brush, spray nozzle, blade, or slot-die are amenable to roll-to-roll production methods that can rapidly yield large-area films.[3,25,26] Manufacturing these films on a large scale could increase manufacturing speed, decrease cost, and require less energy compared with the methods used to produce all-inorganic devices.[27] With all these methods, varying the deposition time and temperature of the substrate or solution can drastically change the film morphology.

When solvent leaves the film rapidly, the remaining organic molecules can adopt kinetically trapped packing structures, resulting in heterogeneity in aggregate structure and amorphous regions.[28,29] Variations in molecular arrangement and

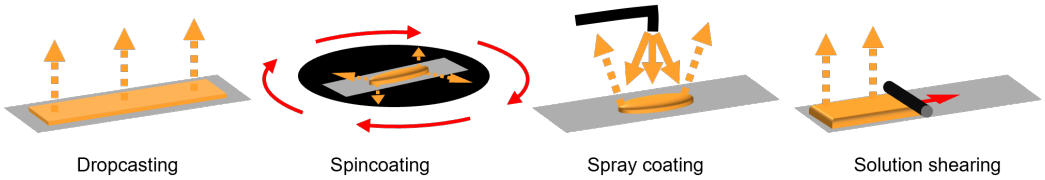


Figure 2. Film deposition techniques. Solid orange and dashed orange arrows represent solution deposition and solvent evaporation, respectively, while red arrows show motion of deposition apparatus.

the resulting distribution of electronic coupling between organic molecules can dramatically affect the wave functions and energies of the electronic states, as well as the transition rates between them. This can result in exciton or carrier traps and other local geometries that affect dynamics, exciton migration, and charge transport. In a film with multiple components, such as the electron donor and acceptor in an OPV, deposition and postprocessing can also affect the structure and extent of the interface between the two systems. Changes to this interface can affect exciton diffusion, charge transfer, and charge separation.[30–32] An example of how film deposition conditions change molecular aggregation and electronic structure is given in **Figure 3**.

1.3.2 Post-Processing Techniques. Postdeposition processing techniques such as thermal or solvent annealing can modify photophysics by increasing the number of ordered aggregates.[30,33–35] In a more rapid solution deposition, molecules may be kinetically trapped in a disordered and unstable configuration. Both solvent and thermal annealing can cause the molecules to rearrange into a more thermodynamically favored configuration, but overannealing can lead to larger domains that limit the formation of CT excitons. For a thin film of P3HT:PCBM, as thermal annealing proceeds, P3HT domains become more crystalline, leading to an increase in the hole mobility for P3HT.[34] The PCE of

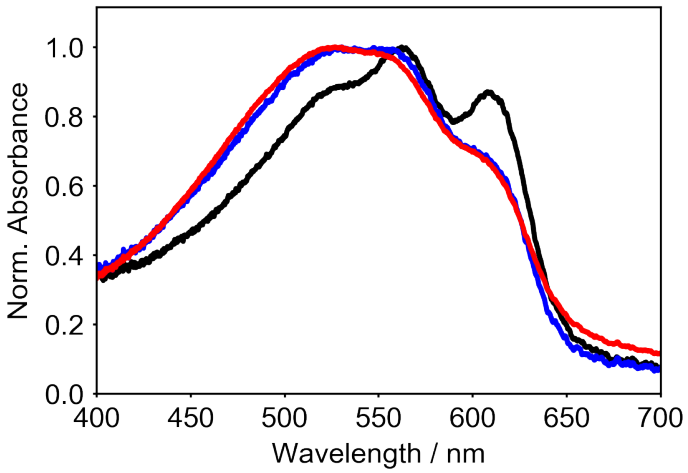


Figure 3. Linear absorption spectra of P3HT films spin coated from a solution of 10 mg/mL (red), 5 mg/mL (blue), and drop casted from a solution of 0.2 mg/mL (black).

SQ:PCBM films is strongly dependent on phase separation, which can be changed by varying the ratio of SQ:PCBM or by thermal annealing.[36–38] There is clearly a delicate balance between domain size and donor-acceptor interfacial area which impacts device performance that is difficult to reveal though ex situ measurements, so in situ measurements can be used to help.

1.3.3 Morphology and Electronic Structure. Transition dipole moments (TDMs) of individual chromophores are proximal in films which results in electronic coupling. Both the proximity and orientation of TDMs determine the degree of electronic coupling, which influences the electronic structure, and thus the absorption lineshape. The electronic coupling (J) is a function of the transition dipole moment (μ), θ, dielectric constant (ϵ), and the distance (R) between TDMs, shown with the equation listed in **Figure 4**. J-aggregates have negative electronic coupling and H-aggregates have positive electronic coupling. If parallel TDMs are oriented in a tip-to-tail fashion with an angle (θ) less than 54.7° (**Figure 4**), they are referred to as J-aggregates. The higher energy dimer state is dark (**Figure**

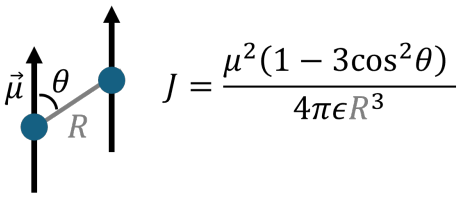


Figure 4. Orientation of parallel transition dipole moments with angle, θ.

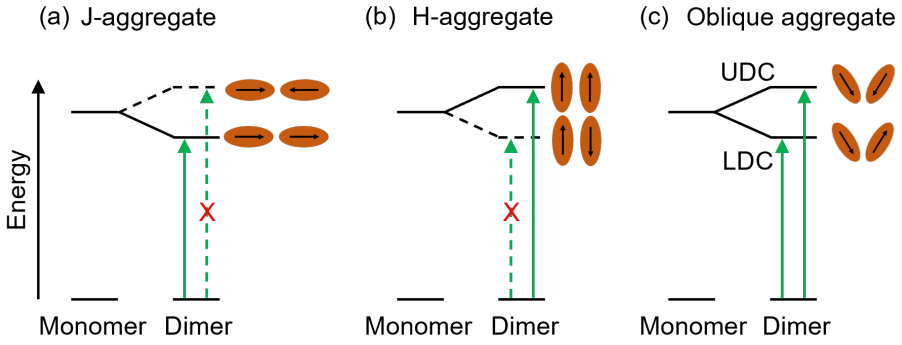


Figure 5. Energy diagram showing the energy level splitting resulting from (a) J-aggregates, (b) H-aggregates, and (c) oblique aggregates. Transitions to a dark and bright state are indicated with dashed arrow with red x and solid arrows, respectively.

5a), resulting in a redshift of the absorption spectrum compared to the monomer. An increase of the 0-0 vibronic peak intensity relative to the 0-1 vibronic peak intensity is also observed. If parallel TDMs are oriented in a face-to-face fashion with θ between 54.7° and 90°(**Figure 4**), they are referred to as H-aggregates. The lower energy dimer state is dark (**Figure 5b**), resulting in a blueshift of the absorption spectrum compared to the monomer. For H-aggregates, an increase of the 0-1 vibronic feature relative to the 0-0 vibronic feature is observed.

In some cases, H- and J- aggregates can coexist, either as an HJ-aggregate[39,40], or as a mixture of H- and J-aggregates.[41] TDMs can also be oriented in an herringbone packing structure (oblique aggregates), which results in Davydov splitting.[42] For oblique aggregates, both dimer states are bright states (**Figure 5c**),

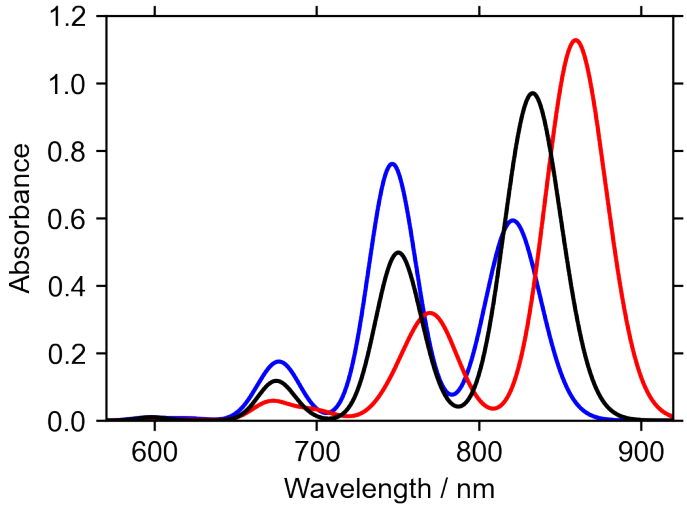


Figure 6. Simulated absorbance spectra using the Holstein-like Hamiltonian for monomers (black), J-aggregates (red), and H-aggregates (blue). The following parameters were used for the simulation: 2 molecules, 4 total vibrational quanta, $\epsilon_0 = 12000$ cm^{-1}, $\omega_0 = 1300$ cm^{-1}, $\lambda^2 = 0.5$. The coupling J_{mn} was 0 cm^{-1} for monomers, -500 cm^{-1} for J-aggregates, and 500 cm^{-1} for H-aggregates.

which yields a double-hump spectrum in linear absorption. The two states resulting from Davydov splitting are referred to as the Upper Davydov Component (UDC) and Lower Davydov Component (LDC). The UDC has H-like character and the LDC has J-like character. However, Davydov splitting only occurs when there is more than one molecule per unit cell.[43]

A Holstein-like Hamiltonian that accounts for electronic energy, vibrational energy, nuclear shift, and electronic coupling can be used to model molecular aggregates in **Equation 1.1**.

$$\hat{H} = \epsilon_0 \sum_n \hat{a}_n^\dagger \hat{a}_n + \omega_o \sum_n \hat{b}_n^\dagger \hat{b}_n + \sum_n \sum_{n \neq m} J_{mn}(\hat{a}_m^\dagger \hat{a}_n + \hat{a}_m \hat{a}_n^\dagger) + \omega_0 \sum_n \hat{a}_n^\dagger \hat{a}_n [\lambda(\hat{b}_n^\dagger + \hat{b}_n) + \lambda^2] \tag{1.1}$$

Where ϵ_0 is the electronic transition energy, ω_0 is the vibrational transition energy, J_{mn} is the electronic coupling, λ^2 is the Huang-Rhys parameter. The electronic raising and lowering operators are $\hat{a}_n^\dagger$ and $\hat{a}_n$, respectively. Similarly,

the vibrational raising and lowering operators are given by $\hat{b}_n^\dagger$ and $\hat{b}_n$, respectively. This problem is simplified by reducing the number of excitations to a two-particle approximation, given by following basis states: $|n, v; m, v'\rangle$. In each basis state, n is the electronically excited particle, v and v' are the vibrational quanta for the particles n and m respectively. This model has one electronically excited particle with vibrational excitation and one particle in the electronic ground state with vibrational quanta. This assumption is valid for small to medium coupling values.[44,45] With even smaller coupling values, a one-particle[46] approximation is valid, but with very large coupling values a three-particle approximation is needed.[47] The Holstein-like Hamiltonian can be used to model linear absorption spectra and determine the electronic coupling (J), informing on the type of aggregates in a sample.

1.4 Spectroscopic Measurements

Performing in situ optical measurements during film formation or processing requires that light be incident on the film and a detector. Some methods of film casting and processing can be difficult to adapt to transmissive measurement. For example, light cannot be transmitted through the metal chuck of a typical spincoater which holds the substrate and is driven by a motor. Homebuilt spincoaters can be creatively designed to circumvent this problem by using the motor to drive a pulley, which actuates and spins a second pulley with a hollow center.[48,49] Processing methodologies like annealing can also be adapted to optical measurements.[33] For example, the solvent can pass through a cell with two opposing transparent faces. If the film is deposited on one internal transparent face, optical measurements can be conducted during solvent annealing.[50] Transmissive measurements can also be conducted during thermal annealing and film deposition,

as discussed in **Chapters 2-4**, by constructing an electrical heating stage with a hole in its surface to allow optical transmission.

Many types of optical spectroscopy are amenable to in situ measurement during the formation and processing of organic films. In situ linear absorbance, reflectance, photoluminescence (PL), optical ellipsometry, Raman, and infrared spectroscopic measurements have all been reported[33,48–58] during some change in an organic film sample. Additionally, in situ x-ray scattering measurements can provide incredible structural insights into film formation.[59–62] Utilizing multiple modalities of in situ measurement yields a more complete picture of both the evolving structure and photophysics of organic systems. However, the process of film formation and the morphology of the resulting films are often different from one film to the next. Thus, the multiple modalities should optimally measure the same film deposition. Otherwise, the different measurements could be reporting on quite different film formation processes, and their results should not be correlated. Creative instrument design strategies can enable multimodal measurements during film formation[55,63], such as absorption and PL. The two measurements can occur at slightly different locations on the film to prevent scatter from the white light source from contaminating the PL measurement. However, organic films are also commonly spatially heterogeneous. The precise morphology of the film in two measured spots may not be the same.

Multiple optical measurements can occur on the same spot on the sample by using strategies described by Buchhorn et al.[49] The white light source and excitation laser for absorbance and PL measurements can be alternately switched on, and transmission of the white light and sample emission after photoexcitation are collected by the same fiber and collimated with a lens. A

controller synchronizes these light sources with the phase of an optical chopper with reflective blades, transmitting the PL and reflecting the white light. The transmitted PL can then pass through an emission filter before passing through the optical chopper again. Both the white light and PL are focused and collected by the same fiber after the optical chopper, and measured with the same spectrometer. This enables rapid, alternating measurements of the same spot on the sample, while also ensuring that the white light used for the absorbance measurement does not contaminate the PL measurement.

1.4.1 Transient Absorption. TA is a time-resolved pump-probe spectroscopy that can measure the transition rates between stationary states in a sample. A pulsed laser is used to excite the sample and probe the absorption of the excited sample. The time resolution of the instrument is optimized by compressing the laser pulses using a prism compressor, grating compressor, or chirped mirrors. The output from the laser is typically split using a beamsplitter, with one of the resulting beams serving as the pump and the other as the probe. The pump pulse energy must be sufficient to excite a small population of excitons in the sample, with typically <1% of the absorbers excited within the measured sample volume.[64] A parametric amplifier can tune the wavelength of the pump pulses to be resonant with the sample to generate a population of excited species. The probe pulse typically has a broadband spectrum generated by focusing into some transparent medium, but can also be narrower band for so-called 'one-color' measurements. A white light continuum is more useful for investigating a larger wavelength range and is necessary to fully explore the excited state dynamics for a system of interest. When a pulsed laser is focused into some transparent medium or gas, this causes a change in the index of refraction, referred to as the optical Kerr effect. The optical

Kerr effect causes a shift in the phase of the pulse. The change of phase leads to a frequency shift of the pulse, called self-phase modulation (SPM). **Equation 1.2** represents the simplest model of the change in frequency caused by SPM[65]:

$$\omega(t) = \omega_0 - \frac{n_2 \omega_0 z}{c} \frac{\partial I(t)}{\partial t} \tag{1.2}$$

Where n_2 is the second order refractive index, ω_0 is the initial frequency, and z is the propagation distance. Assuming a Gaussian pulse of $I(t) = I_0 e^{-t^2/\tau^2}$,

$$\omega(t) = \omega_0 + \frac{2 n_2 \omega_0 z t}{c \tau^2} I(t) \tag{1.3}$$

Equation 1.3 shows the dependence of the pulse power, time, and propagation distance on the resulting white light continuum. More details on white light generation (WLG) are given in **Section 1.4.3.2**.

This probe pulse interacts with the sample at some time after the pump generates excited species. The time delay between the pump and probe pulse is often controlled using a retroreflector on a high-precision motorized translation stage. The pump pulse toggles between being blocked and being let through to the sample using an optical chopper. Both the pump and probe pulses are focused to a spot on the sample, and the transmitted probe is sent to a spectrograph, which typically consists of a dispersive grating and a detector array. TA signal is the change in transmission (ΔT) owing to illumination by the pump pulse. This can then be converted to differential optical density:

$$\Delta OD = -\log(\Delta T/T + 1) \tag{1.4}$$

After the pump pulse interacts with the sample, the probe pulse can interact with the sample, resulting in three possible observed signals (**Figure 7**). Ground state bleach (GSB) occurs when the population of the ground state decreased from pump excitation, resulting in the ground state absorption being less with pump

excitation. This signal results in a negative ΔOD. This signal appears at similar wavelengths to linear absorption. Stimulated emission (SE) occurs when the probe pulse interacts with an already excited population, causing that population to return to the ground state. As more photons are being released in this process, the ΔOD is negative. This signal appears at similar wavelengths to fluorescence. Excited-state absorption (ESA) occurs when the probe excites a population that was already excited by the pump pulse to a higher energy excited state. As less photons are incident on the detector, this signal results in a positive ΔOD. The resultant TA signal is typically a combination of these three signals. TA measurements can elucidate the growth and decay of populations of non-emissive excited states after photoexcitation, which steady state spectroscopy cannot provide.[66–74] The limitation of traditional TA is that measurements at each pump-probe time delay occur in series, typically by translating the retroreflector between each measurement. As a result, many minutes to a few hours of measurement are typically required to achieve a reasonable signal-to-noise ratio (SNR). This limits traditional TA to the study of systems that are stable for the duration of that measurement.

1.4.2 Single-Shot Transient Absorption. Single-shot transient absorption (SSTA) addresses the limitations of traditional TA instruments by simultaneously measuring signal at a range of pump-probe time delays. The instrument design used in the Wong lab is shown in **Figure 8**. The two primary strategies for spatial encoding are depicted in **Figure 9**. Angled beams can spatially encode the time delay at the sample position,[75–83] or transmissive or reflective echelons can encode the time delay at the back focal plane of the lens prior to the sample.[84–91] The time delay between the pump and probe must vary

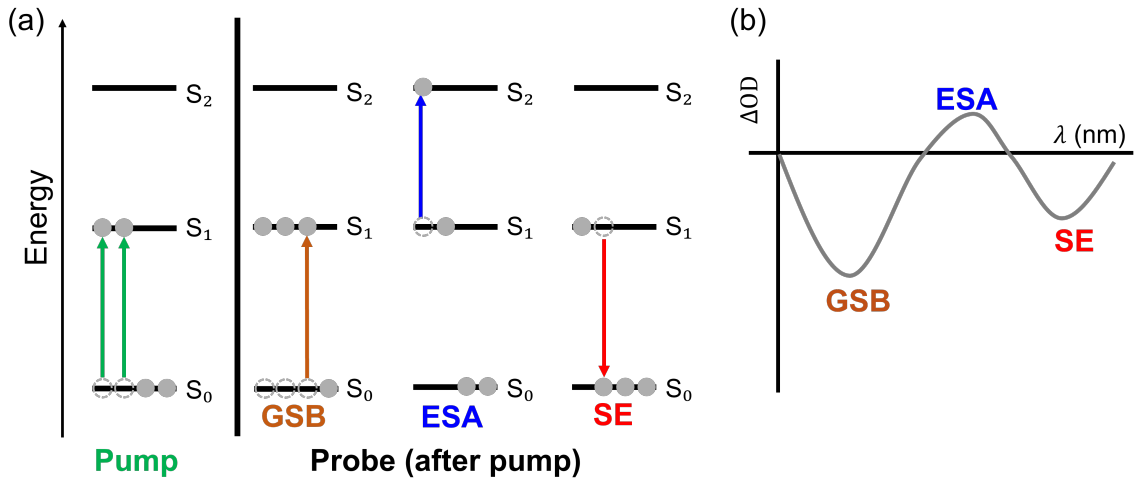


Figure 7. Cartoon of possible TA signals.

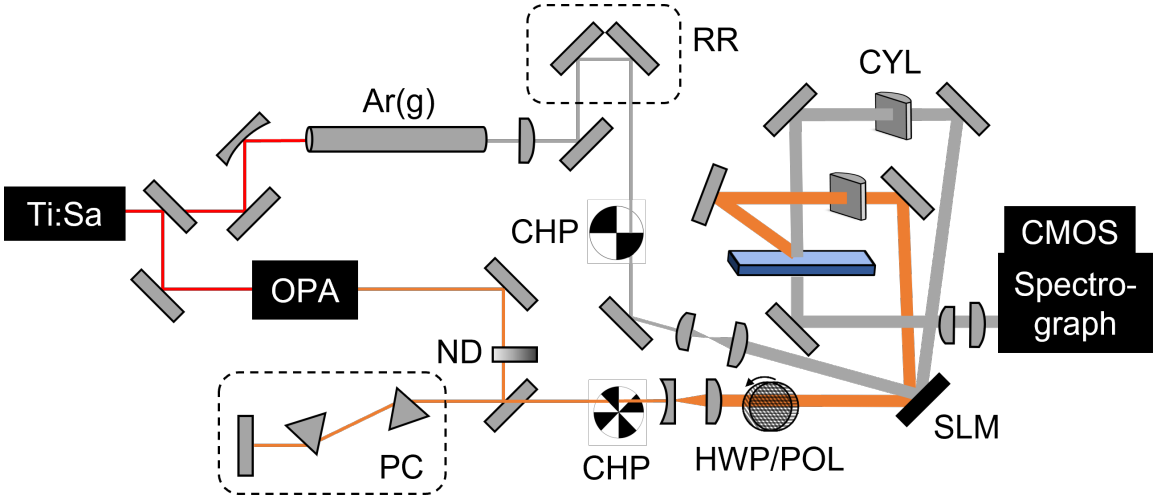


Figure 8. SSTA apparatus. Ti:Sa, titanium:sapphire laser; BS, beam splitter; OPA, optical parametric amplifier; PC, prism compressor; CHP, optical chopper; RR, retroreflector; Ar(g), pressurized argon gas cell; SLM, spatial light modulator; CYL, cylindrical lens. Sample stage shown in blue.

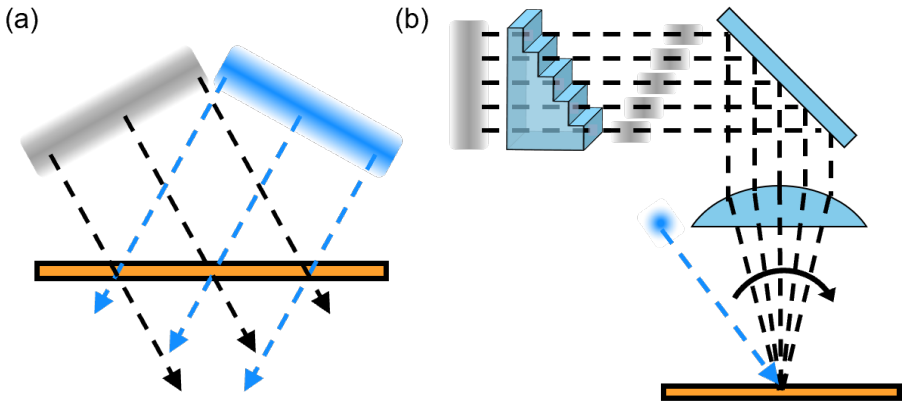


Figure 9. Angled beams (a) or echelon optics (b) can be used to spatially encode the time delay between the pump (blue) and probe (grey), with dashed lines showing the beam propagation direction.

as a function of location in the sample plane (**Figure 9a**) or the back focal plane (**Figure 9b**), and the probe beam at that plane must be imaged onto an array detector after it has passed through the sample. When spatial encoding occurs at the back focal plane, the pump and probe pulses can then be focused to a spot at the sample plane, as is typical for a traditional TA measurement. When spatial encoding occurs at the sample plane, the measured area must be larger, which enables higher pulse energies to be used and can improve the SNR, but requires a relatively spatially homogeneous sample.

The fundamental elements of an SSTA instrument are similar to those for a traditional TA instrument, with a few notable differences. Here, we focus on spatial encoding the pump-probe time delay at the sample plane, similar to **Figure 9a**, but some of the issues discussed below also apply to spatial encoding in the back focal plane.

1.4.2.1 Time Delay and Resolution. The range of the pump-probe time delay is $t_{range} = d \sin\theta / c$, where d is the length of the line of overlap between the pump and probe at the sample position, θ is the angle between the pump and

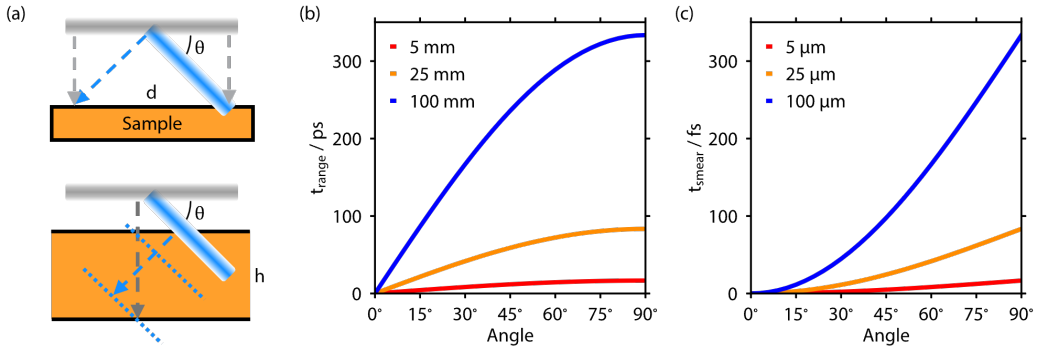


Figure 10. (a) Schematic illustrating parameters that determine time delay. Pump-probe time delay is different at the top and bottom of a column of sample that is measured using a single detector pixel, resulting in loss of time resolution. (b) Time range for three different overlap line lengths at the sample and (c) time smear for three different film thicknesses as a function of angle between the pump and probe pulse.

probe wave fronts, and c is the speed of light, **Figure 10a**. Longer lines of overlap on the sample enable greater pump-probe time delay ranges, **Figure 10b**, but the desire to measure a longer line of sample must be tempered with the increased pulse energy, optic size, and sample size needed.

While the angle between the beams can be increased to elongate the pump-probe time delay range, this can also reduce time resolution, particularly when measuring thick samples, **Figure 10c**. The column of sample traversed by a particular region of the probe beam will have been excited by different regions of the pump beam, **Figure 10a**. This effectively smears the pump-probe time delay within the thickness of the sample. The extent of this smearing is $t_{smear} = h(1 - \cos\theta)/c$, where h is the sample thickness. Note that this is a simplified expression that does not account for the refractive index of the sample.[92] If t_{smear} is less than the duration of the pump pulse itself, the sample thickness and angle will not have much impact on the time resolution. The angle can thus be chosen with the sample thickness, pulse duration, and anticipated dynamics in

mind, to optimize the time delay range and resolution. For example, as typical time constants are in the tens to hundreds of picoseconds for exciton diffusion, and as fast as a hundred femtoseconds for charge separation,[93] t_{smear} should be <100 fs if these processes are of interest. **Figure 10c** illustrates that a 100 μm film will not limit the time resolution of an instrument if $\theta < 45°$. Films with $h < 25$ μm will not have a significant impact on time resolution for any θ. For measurements during film deposition, the thickness of the layer of deposited solution, which is significantly thicker than the resulting film, may affect time resolution.

The resulting spatially encoded pump-probe time delay range is imaged onto an array detector. If a broadband probe is used, the light will be dispersed by a spectrograph prior to arrival at the detector. Thus, each two-dimensional image contains a transient spectrum, and the time delay and wavelength reported by each pixel is determined by a calibration procedure.[75]

1.4.2.2 Pulse Energy. Measuring a line of sample in an SSTA instrument requires more pulse energy than that required for the equivalent measurement of a spot in a typical TA instrument. Ideally, the pump should excite an organic film to near the upper limit of its linear regime, such that the SNR can be optimal while avoiding exciton-exciton interactions. The energy density required for this can vary widely from <10 μJ/cm^2 to >400 μJ/cm^2 for different organic systems.[94–98] Even at the high end of this range, a pump pulse need only be 0.3 μJ for a 300 μm spot, typical for a traditional TA instrument. However, if the pump is spread over a 20 mm x 300 μm line for angled beam SSTA, the required pulse energy becomes 25 μJ. Some higher repetition rate fs-laser systems may not be able to deliver the required pulse energy after accounting for the conversion efficiency of

an optical parametric amplifier and energy losses at the optics that interact with the pump.

The need for increased pulse energies also applies to the probe. A pulsed white light continuum for broadband TA measurements is typically generated by focusing the fundamental of a fs-laser into a crystal of sapphire or calcium fluoride.[65] The conversion efficiency of the incident pulse at its original wavelength to the broadband pulse is typically quite low, for example only ∼2% in sapphire.[92] Despite this low efficiency, sapphire is capable of producing sufficient broadband pulse energies for TA measurements of small sample spots. In any spatially encoded SSTA measurement the probe pulse must be imaged onto multiple pixels, with each pixel encoding some particular pump-probe delay time. Thus, more probe photons are necessary to achieve a similar SNR. The simplest way to increase the energy of the broadband pulse for a spatially encoded SSTA measurement is to increase the pulse energy input into the sapphire. However, when the laser-induced damage threshold of the material is exceeded, the intense electric field of femtosecond laser pulses can induce avalanche ionization in solid media, which irreversibly damages the material. Although sapphire has a relatively high damage threshold (5-10 J/cm^2 using 100 fs pulses),[99] it is not capable of generating adequate broadband pulse energy for measurements using a spatially encoded time delay without damage.

Damage can be avoided and adequate broadband probe energies can be achieved by utilizing non-solid media for continuum generation. High pulse energies have been reported when generation occurs in liquid jets[100–102] and in gas cells.[103] Although the conversion efficiency may be significantly lower than in solid media, their resistance to avalanche ionization enables the use of intense input pulses that

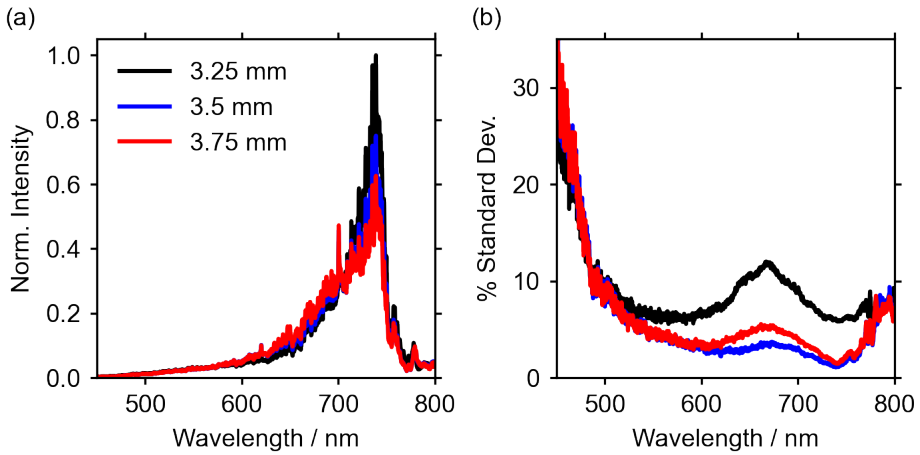


Figure 11. (a) White light spectrum generated from an argon tube at a differential pressure of 0.56 bar. (b) Corresponding percent standard deviation.

more than compensate for the lower conversion inefficiency. Continuum generation in an argon gas cell is an example of this. Continuum generation occurs over a short distance in the center of a >1 m long cell, with long focal lengths into and out of the cell preventing damage to the input and output cell windows. Many factors impact conversion efficiency and spectral stability for a gas cell, such as focal length, the diameter of an iris before the cell, pulse duration, gas pressure, and gas identity.[92,104] White light stability is poor at smaller iris diameters and at higher diameters becomes unstable again (**Figure 11**) and can lead to burning of the windows of the argon cell. Although the efficiency of a gas cell may be well-under 1%, this is offset by the increased input energy, yielding an output energy that is sufficient for SSTA measurements.

1.4.2.3 Beam Flattening. Accurate TA measurements using a spatially encoded pump-probe time delay require that the pump and probe both have a relatively flat spatial profile at the plane where spatial encoding occurs, either the sample plane or the back focal plane. If a Gaussian spatial profile is used, a larger population of excited species will be photogenerated for pump-

probe time delays encoded by the middle of a focal line or the middle of the back focal plane. This could result in different dynamics owing to interactions between these excited species (e.g. exciton-exciton annihilation), which would make the spatially encoded measurement inaccurate. Those same areas would then be measured with larger probe intensity, yielding a greater SNR, while the edges of the spatially encoded region would be measured with weaker probe intensity and have a lower SNR. This is the primary reason why many of the SSTA instruments have such short pump-probe time delay ranges – in these instruments, only the central, relatively flat portion of a Gaussian beam profile is utilized for the spatially encoded time delay. The time delay range can be expanded by flattening the spatial profile of the pump and probe pulses such that the pulse energy is equally distributed over the measured line of sample.

If the input beam is close to Gaussian, commercially available aspherical lenses can shape the beam to a top-hat profile, which can be used in the back focal plane of an imaging system, or further focused to a flat line using a cylindrical optic. If the initial beam profile is not adequately Gaussian, the output from this optical system may not be adequately flat. In this case, geometric beam shaping can be performed on both the pump and probe pulses using a phase-only spatial light modulator (SLM). For the system described here, a SLM is used to reshape both the pump and the probe. Variable phase is imparted to light that interacts with each pixel of the SLM, which can cause the SLM to act similarly to a lens or prism, adjusting the convergence and translation of parts of the beam, **Figure 12a**. While the phase map needed to shape an imperfect Gaussian profile to a top-hat is not analytically known, numerical methods can be applied to get close to an even spatial profile.[83] Calibration and normalization can account for any small

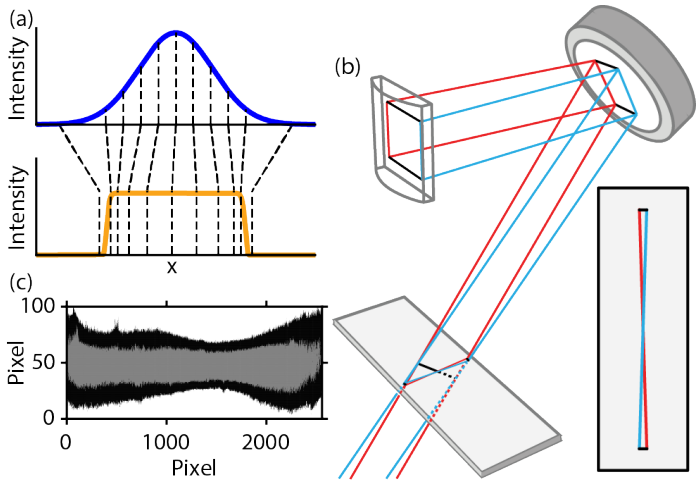


Figure 12. (a) Intensity of a Gaussian spatial beam profile can be redistributed into a flat-top profile using an SLM. (b) Pump beam focused to the sample plane using a cylindrical lens. Inset shows a top-down view of the bowtie shape at the sample plane. (c) Pump beam imaged with fluorescent sample showing initial bowtie shape (black) and after imparting variable focal length (grey).

remaining variations in the spatial profile of either the pump or the probe, so long as the measured sample is excited in the linear regime.[75] However, post-processing of the data cannot change the SNR measured at different locations. When using a pump beam with a non-uniform spatial profile, the areas with lower incident energy density will have a lower density of excited species and thus a reduced SNR. Similarly, the regions measured with lower probe energy will also suffer from a lower SNR. Thus, measurements using closer to perfect top-hat spatial profiles and with incident power close to the upper limit of the linear excitation regime will have a better SNR.

If the pump is focused to a line to spatially encode the time delay, one subtle consideration is that the pump pulse energy should ideally be uniform over both the length and width of the line projected by the pump onto the sample. If the pump pulse is not incident normal to the sample, the focal line produced by a cylindrical lens will also be angled relative to the sample. Thus, even if the

pump is focused to a perfectly evenly illuminated line, its projection onto the sample plane will appear to be shaped like a bowtie, with more energy density at the center compared to the edges, **Figure 12b**. The overall pulse energy would have to be lowered to avoid exciton-exciton interactions in the center, lowering the measured SNR at the edges. This is an argument for using an SLM to shape the beam instead of a simple aspheric lens, as its phase map can be modified to provide variable focal length lensing to avoid the bowtie shape at the sample plane.[92] The pump beam is difficult to image directly, but a fluorescent sample can be used to determine the intensity profile of the beam before and after implementing the variable focal length with an SLM, **Figure 12c**.

1.4.2.4 Dynamic Background Correction. Traditional TA measurements utilize a single optical chopper in the pump beam line such that the transmission of the probe pulse with (T_1) and without (T_0) pump photoexcitation of the sample can be measured and compared to yield the differential transmission ($\Delta T = T_1 – T_0$). Any light that is incident on the detector but is not altered by the presence of the pump (e.g. ambient light) will not be included in ΔT. The pump itself, however, can cause additional detected light that is unrelated to the differential transmission. In particular, the pump can cause sample PL and scatter, and if any of this light is incident on the detector it will contribute to the apparent ΔT as it is also modulated by the presence or absence of the pump. As the pump-induced PL and scatter do not change as a function of pump-probe delay time, the contribution of this light to ΔT is not typically a significant issue – the constant baseline in the measured transients and can be simply subtracted during data processing. These contributions are more problematic if they vary as a function of the pump-probe delay, as may be the case for a spatially encoded time delay, and

if these contributions change as a function of real-time, as is likely for an evolving sample. An additional optical chopper placed in the probe beam line can allow these background contributions to be subtracted for each measured transient. If the frequency of the chopper in the pump beam is double or half that of the chopper frequency in the probe beam, all four possible combinations of the pump and probe pulses can be detected: T_{11}, T_{10}, T_{01}, and T_{00}, where $T_{pump\ probe}$ is the transmission, 0 represents a blocked pulse, and 1 a pulse incident on the sample. T_{10} accounts for the pump-induced scatter and PL and T_{00} is signal present when neither pump nor probe are incident on the sample, including dark current and ambient light.[105] The differential transmission can be calculated as

$$\frac{\Delta T}{T} = \frac{(T_{11} - T_{10}) - (T_{01} - T_{00})}{(T_{01} - T_{00})} \tag{1.5}$$

and then converted to ΔOD. This correction technique is critical when measuring evolving organic films, as the PL and scatter are likely to undergo significant changes. The PL detected can vary spatially, resulting in a varying contribution to the ΔT signal as a function of a spatially encoded time delay as opposed to appearing as a constant baseline. Thus, its contribution must be measured separately and subtracted. The PL decreases significantly when the molecules aggregate to form a thin film, thus requiring that its contribution be continually measured during any change from solution to film. Additionally, the film may have small structural features that cause pump scatter, and these contributions must also be subtracted. Note that scatter subtraction does not entirely eliminate the impact of scatter. As TA is the measure of a very small signal (ΔT) on top of a large transmission signal, a large dynamic range is needed. Scatter consumes some of that dynamic range, leaving less for the signal from transmission and the small fraction that comprises the differential transmission.[105]

The incorporation of dual choppers to measure these background contributions also increases the time needed to perform each measurement, and thus the time needed to attain an adequate SNR. However, each individual corrected transient still only requires a few ms, and the measurement will be accurate as long as the sample does not significantly change during those few ms. Averaging multiple spectra will still accurately report the dynamics during that averaged time period.

1.4.2.5 Spatial Heterogeneity. Organic thin films may be spatially heterogeneous, which can place limitations on SSTA. This does not pose a problem for SSTA measurements if the pump-probe time delay is spatially encoded at the back-focal plane, as the same sample volume will be measured for each time delay. Heterogeneity can, however, pose a problem if the time delay is encoded at the sample plane. In this type of SSTA measurement, each pixel of the detector corresponds to a particular region of the sample, and that pixel reports the ensemble TA measurement for some particular pump-probe time delay. Thus, heterogeneity within each small sample volume is averaged in that ensemble measurement and does not present a problem. On the other hand, heterogeneity between the small sample volumes does present a significant problem, as the dynamics within each small volume may be different and thus the transient built from a series of these small volumes would not be accurate. A motorized actuator can be used to translate the sample during a measurement to effectively increase the size of the ensemble being measured by each pixel.[83,105] The rate and distance needed for sample translation depends on the size of the spatial features in the sample and the number of pixels onto which the probe is imaged.

1.4.3 Summary. Compared to a traditional TA spectrometer, the SSTA spectrometer (**Figure 8**) used in this thesis includes an argon tube for white light generation with sufficient power, a SLM for reshaping the beam profiles from Gaussian to flat-top, and a secondary chopper for a dynamic background calculation. These are essential components because typical white light sources for TA measurements cannot provide enough power, uniform excitation and probing of the sample is necessary for accurate meaurements of excited state dynamics, and organic thin films have a large contribution of pump scatter that evolves during in situ measurements that must be corrected for. SSTA has allowed for in situ measurements of excited state dynamics during evolution of a sample with reasonable SNR in ∼30 s. SSTA was used to investigate polymer: fullerene blend films and donor-acceptor-donor films during thermal annealing (**Chapter 2,3**) and donor films during film deposition (**Chapter 4**).

CHAPTER II

THERMAL ANNEALING OF DONOR-ACCEPTOR BLEND FILMS

Includes material from:

Walbrun, Z. S.; Fisher, R. V.; Wong, C. Y. Evolution of Charge Transfer During Thermal Annealing of a Polymer:Fullerene Thin Film. **2025**, Submitted.

Organic semiconducting materials show great promise for use in organic photovoltaics (OPVs) owing to their chemical tunability, energy efficiency, and solution processibility[1–3,6,106], but their power conversion efficiency (PCE) has historically lagged behind all-inorganic devices.[13,106] One of the most studied organic semiconducting material combinations, poly(3-hexylthiophene-2,5-diyl) (P3HT): phenyl-C61-butyric acid methyl ester (PCBM), can only reach a top PCE of 5%[107], primarily limited by the low absorption of visible light by PCBM. OPVs are the focus of renewed attention owing to the development of non-fullerene electron acceptors.[6,15,108,109] OPVs prepared with a non-fullerene electron acceptor in conjunction with P3HT have yielded a PCE of 10.7% after thermal annealing[17], demonstrating the promise of P3HT when combined with a suitable acceptor.[110] In this paper, we use P3HT and PCBM as a model system to demonstrate a methodology for measuring how the excitonic processes change during thin film processing and present a framework for using measured dynamics to determine the evolving sub-populations of polymer morphologies. This is an ideal model system for initial analysis, as PCBM, a fullerene derivative, does not exhibit significant ordering in blend films[111] and its absorption spectrum does not significantly overlap with P3HT. Thus, the P3HT:PCBM measurements reported here can focus on the behavior of the P3HT. This can be used as a basis for comparison with future

measurements of P3HT with non-fullerene acceptors, which will likely absorb light in the visible region and exhibit annealing-induced molecular ordering.[112]

OPVs are composed of an active layer containing organic semiconducting materials sandwiched by electron and hole transfer layers and electrodes. The active layer is typically comprised of a combination of electron donor and acceptor materials. A photogenerated exciton in the active layer must diffuse to a donor-acceptor interface to form a charge transfer (CT) exciton, where the electron and hole reside in the acceptor and donor materials, respectively. These charges separate if they can overcome their binding energy. Active layer morphology has a major impact on electronic structure, which affects the rates of these processes. The structure of P3HT aggregates in thin films are difficult to predict, as they contain a heterogeneous distribution of kinetically trapped aggregates due to the weak intermolecular forces between organic molecules.[28,29,113,114] For a semiconducting polymer where each monomer is a chromophore, the electronic structure of the organic semiconductor changes as a result of electronic coupling between monomers, which depends on the proximity and orientation of their transition dipole moments (TDMs).[115] In P3HT, the TDM for each monomer lies along the backbone of the polymer chain. In a straight P3HT chain, monomers are aligned head-to-tail such that their TDMs are colinear. This intrachain ordering results in negative electronic coupling and is called J-aggregation. H-aggregation occurs when monomers are aligned face-to-face with parallel TDMs, which occurs if separate segments of a P3HT chain undergo $\pi - \pi$ stacking. This interchain ordering results in positive electronic coupling. In some cases, H- and J- aggregates can coexist as an HJ-aggregate[39,40] or as a mixture of H- and J-aggregates.[41] In P3HT films, intra- and interchain order coexist, leading to HJ aggregates with

electronic coupling determined by the relative amount of H- and J- aggregation. The relative intensity of the 0-0 and 0-1 vibronic features is a useful indicator of the degree of intra- and inter-chain ordering, which manifests as J- and H-aggregation, respectively.[39,116] Intra- (inter-) chain order will generally cause the absorption spectrum to red- (blue-) shift, and the 0-0:0-1 peak intensity ratio to increase (decrease).

Typically, the effect of interchain ordering in P3HT films dominates over intrachain ordering, to yield absorption spectra that are primarily H-like in character. However, spectra that exhibit more J-like character have been observed in single-crystal P3HT,[117,118] P3HT nanofibers,[119] and P3HT:polyethylene oxide (PEO) films washed with water.[120] Even in P3HT films with dominant H-like character, fluorescence measurements can show variations in interchain order.[121,122] Oh et al. reported that solution preparation methods drastically change the structure of P3HT in solution, as P3HT solvated at lower temperatures adopts a rod-like conformation, while higher temperatures yield a coil-like conformation.[123,124] P3HT and P3HT:PCBM films that are spin coated from a solution of coil-like P3HT exhibit less interchain order.[124] P3HT:PCBM films that are spin coated typically result in an amorphous film with minimal crystallinity as indicated by the lack of vibronic features in its linear absorption spectrum.[74]

Solvent and thermal annealing are common OPV processing techniques that improve PCE by increasing the extent of crystallinity and homogeneity in the active layer.[34,114] In P3HT:PCBM films, thermal annealing causes phase separation, leading to larger, more crystalline of P3HT domains with higher carrier mobility.[34,125–130] Performing in situ measurements during thermal annealing provides insight into the relationship between structure and function.

In situ XRD measurements of P3HT films by Joshi et al. show a decrease in the $\pi - \pi$ stacking distance and increase in lamellar spacing during annealing that reverted to their original geometry during cooling.[131] Pingel et al. used linear absorption measurements during thermal annealing to show that pre-melting of the P3HT chains below the melting point caused a decrease in the conjugation length of the polymer that reverted to its original conjugation length upon cooling.[132] Agostinelli et al. collected in situ grazing-incidence wide-angle X-ray scattering (GIWAXS) measurements of P3HT:PCBM during thermal annealing and found an initial crystallization event during which the disordered P3HT monomers formed aggregates. Further annealing of the P3HT:PCBM films lead to aggregate growth.[130] A combination of in situ current-voltage and GIWAXS measurements by Treat et al. showed that an increase in PCE is observed with the formation of P3HT crystallites with $\pi - \pi$ stacks formed parallel to the substrate.[133] To complement these in situ measurements of structure, we aim to understand how thermal annealing affects the fate of excitons by using in situ electronic spectroscopies. Here, we report on changes induced by thermal annealing and subsequent cooling by applying in situ linear absorption and single-shot transient absorption (SSTA) to neat P3HT films and P3HT:PCBM blends. This methodology can be used for future studies of other donor: acceptor pairs, such P3HT with non-fullerene acceptors.

2.1 Experimental Details

P3HT (Ossila, 24.480 kDa, 93.6% regioregularity) and PCBM (Solaris Chem, 99.5% purity) were both used without further purification. Solutions of P3HT, P3HT:PCBM, and P3HT:PMMA were prepared at 10 mg/mL, 10:10 mg/mL, and 10:80 mg/mL in chloroform, respectively. Solutions were heated to

40°C and stirred at ∼650 revolutions per minute (RPM) for ∼4 hours. Prior to film deposition, glass substrates were cleaned with acetone and methanol. 100 μL of solution were deposited onto the cleaned slides and then spin coated for 30 seconds at 6000 RPM.

Linear absorption and SSTA measurements were conducted on a homebuilt electric heating stage with a slit in the center, allowing light to pass through for in situ measurements. Films were annealed within four hours of deposition, with the sample stage temperature increasing from 30°C to 140°C, increasing by 10°C every 5 minutes. Cooling occurred passively over the course of ∼3 hours. Film temperature was recorded using an IR thermometer (FLIRTG54, emissivity 0.95), **Figure 13a**.

The output of a 7 W, 1 kHz Ti:Sa laser at 800 nm (Coherent Astrella) was split into pump and probe pulses. The desired pump wavelength was selected using an optical parametric amplifier to be 520 nm, resonant with P3HT and P3HT:PCBM films. A prism compressor in the pump beam path yielded ∼80 fs pulses at the sample position. The probe was focused into a 1.6 m homebuilt argon cell with a differential pressure of 0.55 bar for white light generation. The path length of the probe was controlled by a retroreflecting mirror on a translation stage (Newport).

A phase-only spatial light modulator employing geometric beam shaping reshaped the profiles of the pump and probe from Gaussian to flat-top. Cylindrical lenses focused both the pump and probe to a ∼22 mm x ∼85 μm line on the sample. The pump was incident on the sample at an angle of 55° with respect to the probe to generate the spatially encoded time delay. The probe passed through the 25 μm slit of a spectrograph (Princeton Instruments) and was imaged

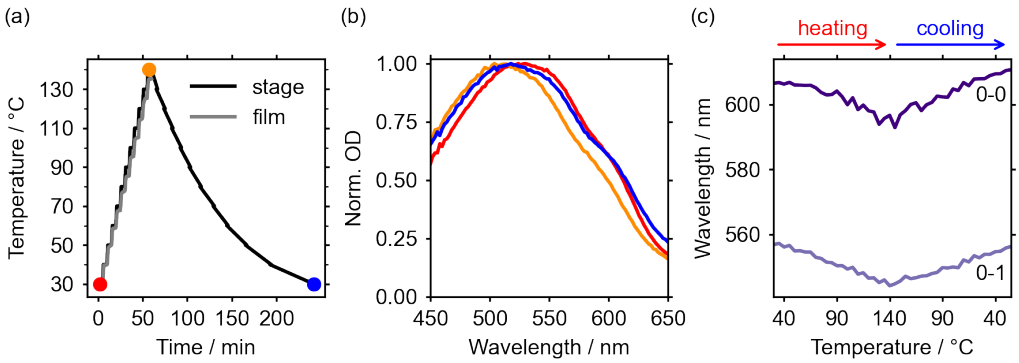


Figure 13. (a) Stage and film temperature as a function of time. (b) Linear absorption spectra of a P3HT film at the temperatures indicated by colored markers in (a). (c) Peak positions during annealing and cooling from Gaussian fitting.

on a CMOS camera (Andor Zyla). A 30 groove/mm grating was used in the spectrograph resulting in a wavelength range of ∼170 nm. SSTA measurements were collected in 30 s with a time delay range of ∼60 ps[75,92,134] and used pulse energies of 402 nJ and 10 nJ for the pump and probe at the sample stage, respectively.

2.2 Neat P3HT Films

2.2.1 Linear Absorption. Linear absorption spectra measured during thermal annealing and subsequent cooling of a neat P3HT thin film are shown in **Figure 13b**. The absorption spectrum of P3HT is composed mainly of three vibronic features at ∼610 nm, ∼560 nm, and ∼510 nm, as well as one broad peak at ∼450 nm associated with amorphous P3HT. The linear absorption spectra were fit to a weighted sum of four Gaussians representing these four features to determine the peak positions as a function of annealing and cooling, **Figure 13c**.

A clear blue-shift in both the 0-0 and 0-1 peaks is observed in the absorption spectrum during heating. As the films are cooled, both the 0-0 and 0-1 peaks redshift to near their original positions before annealing began. This

reversible blue-shift for P3HT has been characterized as a shortening of the conjugation length by pre-melting of the polymer at domain edges.[132,135–137] The pre- and post-annealed linear absorption spectra are nearly identical, except for a slightly higher 0-0:0-1 ratio for the post-annealed spectrum, likely due to an increase in intrachain ordering. It is well known that annealing polymer films can cause an irreversible increase in crystallinity,[131,138–140] dependent on film thickness[131] and molecular weight.[140] As this change is not clearly observed using linear absorption measurements, we turn to the excited state dynamics to see whether it will be sensitive to this change in crystallinity.

2.2.2 Single-Shot Transient Absorption. Excited state dynamics is of great importance for organic semiconductors, particularly the timescale and efficiency of exciton diffusion, charge transfer, and charge separation. Excited state dynamics has been previously characterized using transient absorption (TA) for a variety of P3HT film morphologies[74,97,128,137,141] and P3HT:PCBM films before and after thermal annealing.[34,74,127,128] However, TA measurements have not been collected during thermal annealing of either type of sample due to the timescale of annealing compared to typical TA acquisition times. Here, we report the first in situ TA measurements during thermal annealing and cooling of P3HT and P3HT:PCBM films using SSTA.

SSTA spectra were measured during the annealing and cooling process using the temperature ramping scheme described in **Figure 13a**. Prior to annealing (**Figure 14a,d**), two ground state bleach (GSB) features are observed at ∼550 nm and ∼600 nm that are associated with the 0-1 and 0-0 transitions, respectively. As annealing proceeds, the spectrum blue-shifts (**Figure 14b,e**), owing to decreased

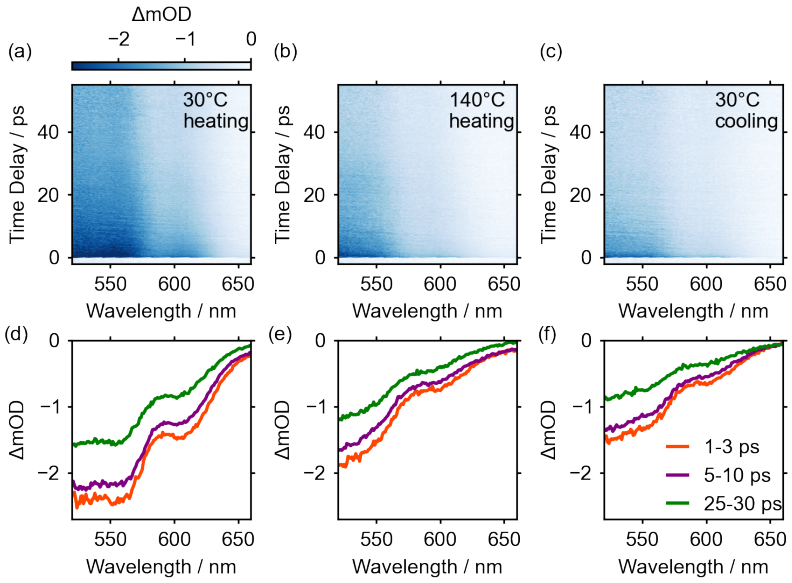


Figure 14. SSTA spectra of a P3HT film measured during (a) heating at 30°C, (b) 140°C, and (c) cooling at 30°C. (d), (e), and (f) show spectral slices from (a), (b), (c), respectively.

P3HT conjugation length. As the film is cooled back to room temperature, the spectrum redshifts to near its original position (**Figure 14c,f**).

2.2.3 Kinetic Modeling. These transient spectra were globally fit with evolution associated difference spectra (EADS) using two exponentials, **Equation 2.1**. In this model, the species with spectrum A_1 is excited with the pump and must undergo energy transfer with a time constant of τ_1 to the species with spectrum A_2. The species with spectrum A_2 decays to its ground state with a time constant of τ_2.

$$\Delta OD(t,\lambda) = A_1(\lambda)e^{-t/\tau_1} + A_2(\lambda)\left(\frac{\tau_2}{\tau_1-\tau_2}e^{-t/\tau_1} + \frac{\tau_2}{\tau_2-\tau_1}e^{-t/\tau_2}\right) \qquad (2.1)$$

At the beginning of annealing, A_2 has a smaller 0-0:0-1 intensity ratio than A_1 (**Figure 15c,g**) implying that the P3HT aggregates that contribute to A_2 have more interchain ordering, and that excitons are funneled to the more highly ordered

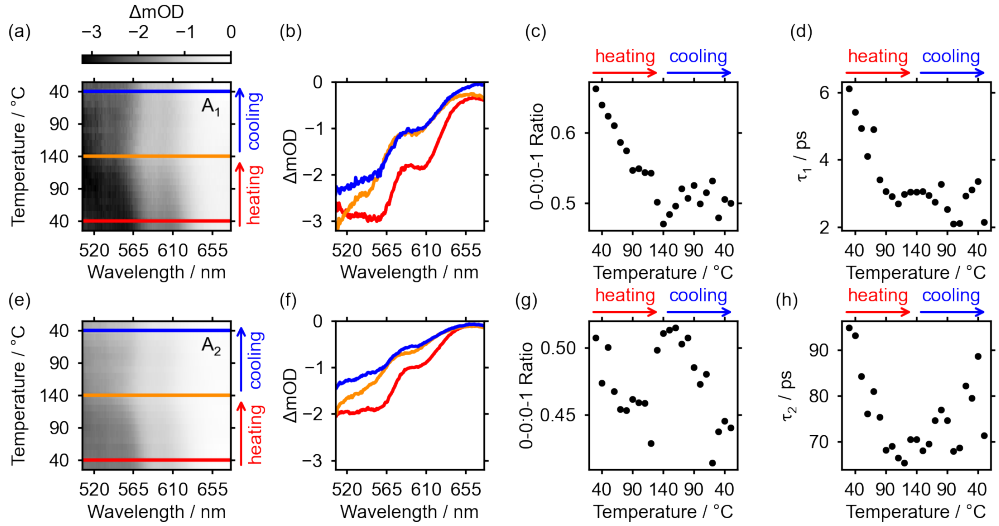


Figure 15. Globally fit EADS to SSTA measurements of P3HT films during annealing and cooling using Equation 2.1. (a) A_1 and (e) A_2 as a function of heating. (b) and (f) show slices from (a) and (e) at temperatures given by color. 0-0:0-1 ratios for (c) A_1 and (g) A_2 as a function of annealing and cooling. (d) Short and (h) long time constant as a function of heating and cooling.

aggregates. The time constant of this transition agrees with previous reports of 3 ps[74] energy transfer between P3HT aggregate species. As thermal annealing and cooling proceeds, the 0-0:0-1 ratio in the A_1 spectrum approaches 0.5, indicating the irreversible formation of more ordered H-aggregates. The A_1 spectrum blue-shifts during annealing and this shift is not fully reversed upon cooling, showing a persistent increase in interchain order. The A_2 spectrum undergoes a blue-shift during heating that is reversed upon cooling, similar to the linear absorbance spectra, indicating a temporary change in conjugation length during annealing. The 0-0:0-1 ratios in the A_2 spectra change significantly less compared to A_1, suggesting that A_2 arises from aggregates that already exhibit interchain order prior to heating. After annealing and cooling, the 0-0:0-1 ratios for A_1 and A_2 are similar. Based on these observations, A_1 and A_2 are assigned to the P3HT aggregates that

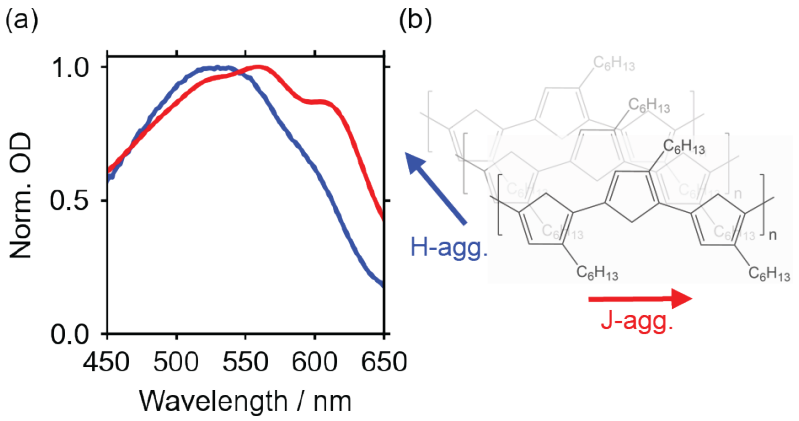


Figure 16. (a) Linear absorbance spectra for a film of neat P3HT (blue) and 1:8 P3HT:PMMA (red). (b) Schematic indicating J- and H-aggregates in bulk P3HT.

began, before annealing, with less and more interchain order, respectively, but have similar structures after annealing.

To support our assignment of A_1 to P3HT aggregates with less interchain order, P3HT was dispersed in an inert polymer matrix of polymethyl methacrylate (PMMA) to disrupt the H-aggregation of P3HT chains. As the concentration of PMMA is increased in the P3HT films, the 0-0:0-1 intensity ratio increased, exhibiting less H-like character (**Figure 16**). However, the 0-0:0-1 ratio never surpassed unity, implying that H-aggregate character is dominant in the P3HT:PMMA films, similar to the peak intensity ratios observed in neat P3HT films. This is consistent with previous reports of P3HT:PMMA blends.[142]

Due to weak intermolecular forces between organic molecules, many different configurations of P3HT can be observed in films before annealing. These differences are sometimes subtle and may not be observable with linear absorption. We have also measured neat P3HT films that produced identical linear absorption spectra (**Figure 17**), but significantly different dynamics. EADS fits to the SSTA spectra showed a larger population of P3HT aggregates with significant interchain ordering

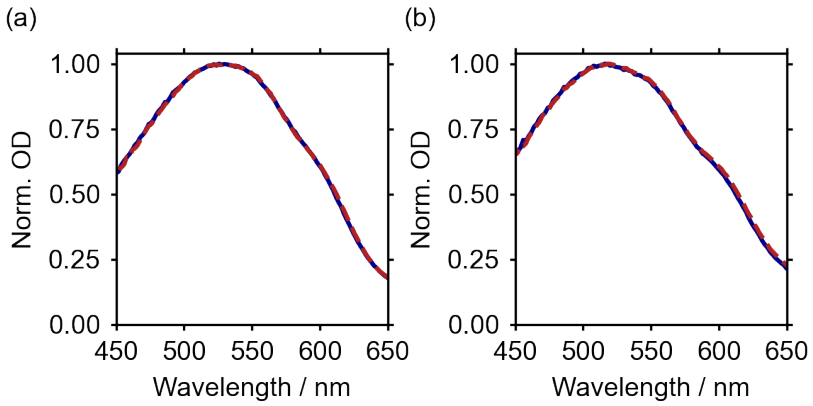


Figure 17. Linear absorbance spectra for pre-annealed (blue, solid) and non-pre-annealed (red, dashed) P3HT films (a) before and (b) after annealing.

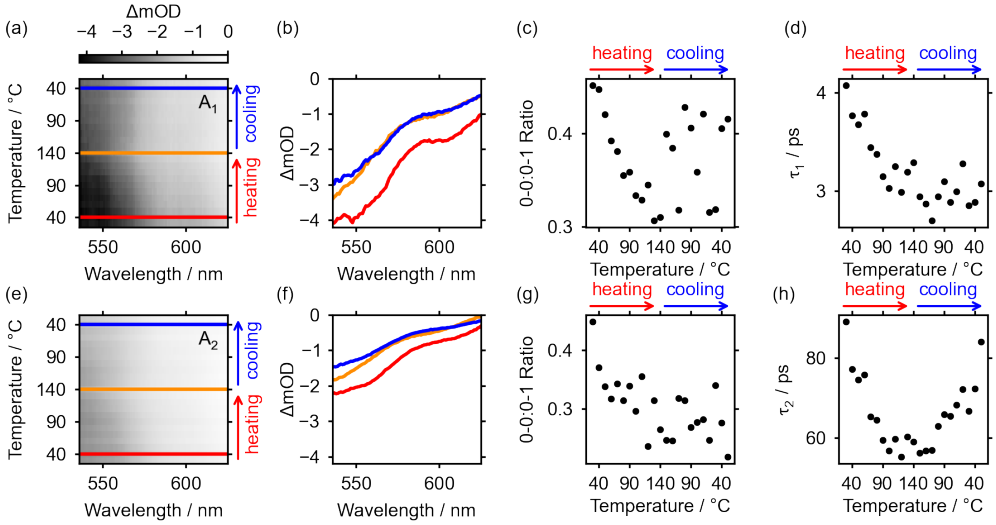


Figure 18. Globally fit EADS to SSTA measurements of P3HT films that began as pre-annealed during annealing and cooling using Equation 2.1. (a) A_1 and (e) A_2 as a function of heating and cooling. (b) and (f) show slices from (a) and (e) at temperatures given by color. 0-0:0-1 ratios for (c) A_1 and (g) A_2 as a function of annealing and cooling. (d) Short and (h) long time constant as a function of heating and cooling.

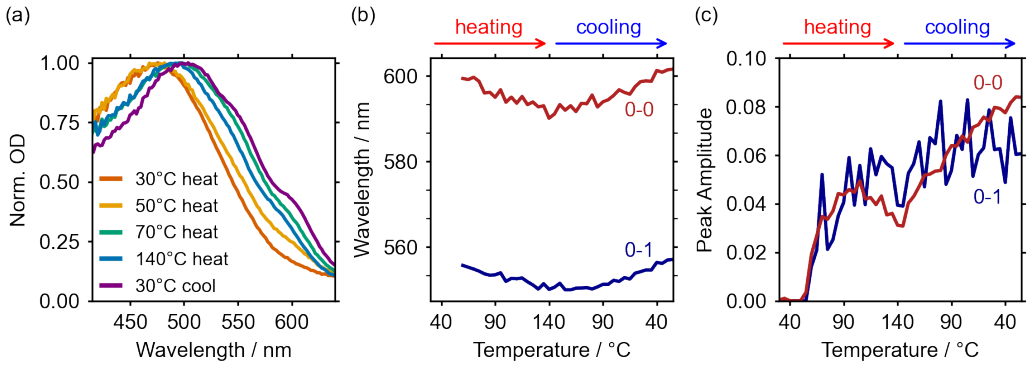


Figure 19. (a) Linear absorption spectra of a P3HT:PCBM film during heating and cooling. Peak (b) positions and (c) amplitudes as a function of time from Gaussian fitting.

prior to thermal annealing, and thus the thermal annealing and cooling process resulted in minimal persistent change to P3HT structure and exciton dynamics (**Figure 18**).

2.3 P3HT:PCBM Films

2.3.1 Linear Absorption. Linear absorption spectra measured during thermal annealing and cooling of a P3HT:PCBM thin film (**Figure 19a**) were fit to a weighted sum of four Gaussians. Peak positions as a function of annealing and cooling are shown in **Figure 19b**.

The absorption spectrum of as-cast films resembles that of P3HT in solution, indicative of amorphous morphology. An increase in the vibronic structure is observed as the films are heated from 30°C to 60°C (**Figure 19c**), indicating the formation of crystalline domains from amorphous P3HT. This occurs as the P3HT:PCBM film passes through its glass transition temperature at ~50°C.[143] A blue-shift is observed as heating continues, ascribed to a decrease in P3HT conjugation length. As the film is cooled back to room temperature, the absorption spectrum red-shifts as the conjugation length rises. An increase in the 0-0 vibronic feature intensity is also observed, indicating increased intrachain ordering.

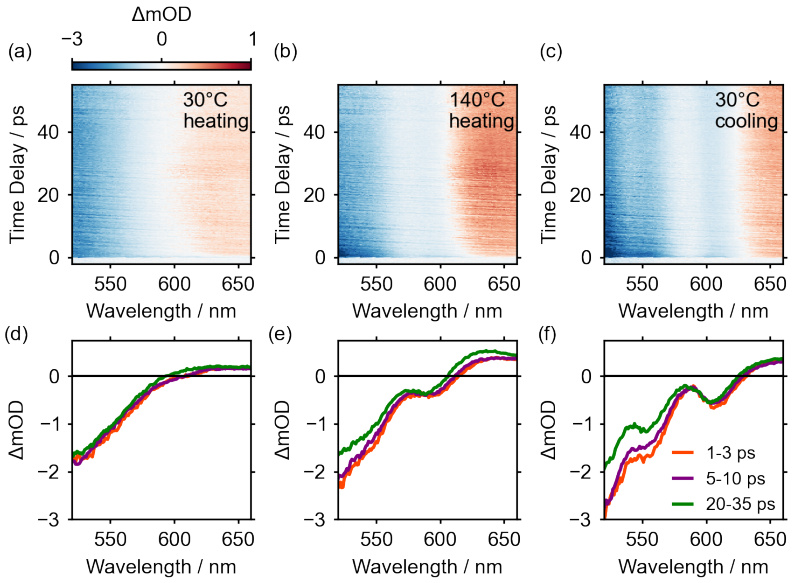


Figure 20. SSTA spectra of a P3HT:PCBM film measured during (a) heating at 30°C , (b) 140°C, and (c) cooling at 30°C. (d), (e), and (f) show spectral slices from (a), (b), (c), respectively.

2.3.2 Single-Shot Transient Absorption. SSTA spectra measured during the heating and cooling of a P3HT:PCBM film are shown in **Figure 20**. The negative GSB spectrum is similar to that of neat P3HT (**Figure 14**) and an additional positive ESA feature at ∼660 nm is ascribed to polarons in P3HT, indicating charge transfer between P3HT and PCBM.[34,74] Before annealing (**Figure 20a,d**), the GSB signal decays with a single time constant of ∼270 ps. As annealing proceeds, a more rapid ∼5 ps decay of the GSB emerges (**Figure 20b,e**) simultaneous with the growth of signal from polarons, indicating increased charge transfer. The growth of polaron signal relative to GSB as amorphous P3HT gains crystalline order shows that annealing is beneficial for charge transfer.

2.3.3 Kinetic Modeling. An EADS model was used to fit the SSTA spectra during annealing and cooling (**Figure 21**). The transients at 30°C and 40°C during heating were best fit with one exponential decay, as the fast charge

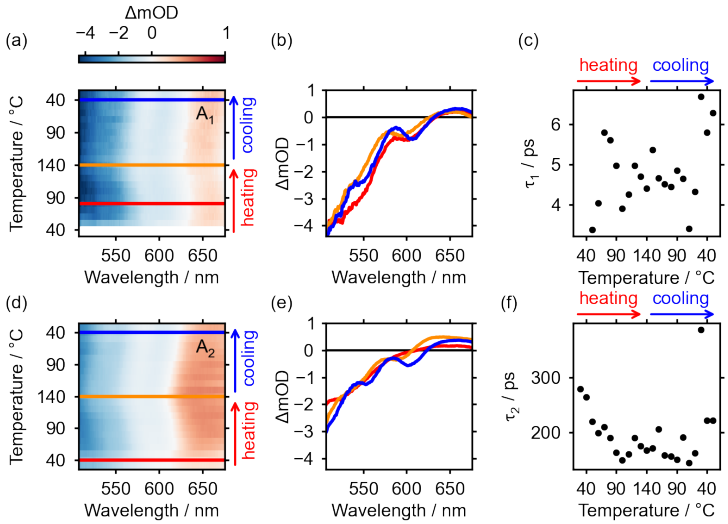


Figure 21. Globally fit EADS to SSTA measurements of P3HT:PCBM films during heating and cooling using Equation 2.1. (a) A_1 and (d) A_2 as a function of heating and cooling. (b) and (e) show slices from (a) and (d) at temperatures given by color. (d) Short and (h) long time constant as a function of heating and cooling.

transfer process is not yet evident. Once the glass transition temperature (50°C) is reached, a second exponential is necessary to fit the faster process that emerges. The new time constant (τ_1) is ~5 ps, which is consistent with the decay of the GSB signal and the slight rise of the ESA signal observed in **Figure 20** and with previous reports of the charge transfer rate in annealed P3HT:PCBM films.[34] Both A_1 and A_2 have spectral features that become more pronounced as cooling proceeds (**Figure 21b,e**), indicating that the P3HT is becoming more crystalline. We assign A_1 to excitons in P3HT, as its spectrum has negligible ESA from P3HT polarons. The larger ESA contribution in A_2 suggests that this spectrum represents the charge transfer state between P3HT and PCBM.

2.4 Summary

We used a combination of in situ linear absorbance and SSTA measurements to track the evolving aggregation and excited state dynamics during annealing and

cooling of P3HT and P3HT:PCBM films. SSTA spectra of neat P3HT films were modeled with EADS and revealed the presence of two species, which begin with less and more P3HT interchain ordering prior to thermal annealing. Both species exhibited a reversible spectral blue-shift owing to the pre-melting of P3HT domain edges, but only the species with less interchain ordering had an irreversible increase in ordering with annealing. SSTA spectra of P3HT:PCBM films revealed that passing through the glass transition temperature increased charge transfer. EADS fits revealed the spectra for P3HT excitons and the P3HT:PCBM charge transfer state. In sum, P3HT:PCBM was used as a model system to demonstrate how polymer ordering and charge transfer can be measured during thermal annealing of electron donor-acceptor systems. This model provides the basis for future studies of other donor-acceptor systems, such as P3HT and non-fullerene acceptors.

CHAPTER III

THERMAL ANNEALING OF DONOR-ACCEPTOR-DONOR FILMS

Includes material from:

Walbrun, Z. S.; Leibfried, L. C.; Hoban, Á. R.; Rasmussen, B. C.; Wiegand, T. J.; Collison, C. J.; Wong, C. Y. Effect of Thermal Annealing on Aggregation of a Squaraine Thin Film. *MRS Advances* **2022**, *7* (12), 239–244.

Walbrun, Z. S.; Hoban, Á. R.; Paulson, A. Y.; Wiegand, T. J.; Collison, C. J.; Wong, C. Y. Morphology Dependent Excited-State Dynamics of Squaraine Thin Films During Thermal Annealing. *J. Phys. Chem. Lett.* **2025**, 4456–4462.

Squaraine (SQ) dyes are donor-acceptor-donor (D-A-D) molecules consisting of an electron accepting squarylium center and two electron donating arms, each with a nitrogen center. SQ molecules can be economically manufactured and solution-processed, and the resulting films can exhibit significant absorption of the solar spectrum. Their absorption spectrum can be chemically tuned by modifying the molecular structure or by influencing their molecular packing in films. SQ molecules with linear side chains and four phenyl ring hydroxyl groups typically form H-aggregates,[144,145] whereas Davydov splitting and J-aggregation are more commonly observed in SQ molecules with bulky side chains[144,146,147] or those with greater hydrogen bonding interactions.[144,145] Some SQ molecules, such as 1,3-bis[4-(N,N-diethylamino)-2-hydroxyphenyl]squaraine (DESQ(OH)), have two different polymorphs, one of which exhibits Davydov splitting while the other exhibits intermolecular charge transfer (ICT).[43,148] In the following sections, I have investigated 2,4-bis(4-dibutylamino-2,6-dihydroxyphenyl)cyclobutane-1,3-dione ($DBSQ(OH)_2$) and 2,4-bis(4-dihexylamino-2,6-dihydroxyphenyl)cyclobutane-1,3-dione ($DHSQ(OH)_2$). Films of these SQs exhibit two peaks in their absorbance

spectra. The two peaks can arise from Davydov splitting in other SQ molecules,[42] but both of these SQ molecules have a triclinic crystal structure with only one molecule per unit cell, precluding this possibility.[43]

X-ray diffraction measurements of these SQ molecules predict the formation of slip-stacked H-aggregates.[43] Owing to the Coulombic attraction between the squarylium center of one SQ monomer and the nitrogen-containing arm of a neighboring SQ monomer, the optically allowed H-aggregate (HA) state is destabilized and the CT state is stabilized relative to a non-slip-stacked aggregate. The destabilized HA and stabilized CT state are near-degeneracy, allowing them to mix.[43] The mixing of the bright H-aggregate state and nominally dark CT state results in peaks for two optically active states in the linear absorption spectrum. These spectra have been previously modeled with an intermolecular charge transfer (ICT) Hamiltonian that accurately describes the double-hump spectrum for SQ molecules.[43]

SQ molecules can be co-deposited with an inert polymer, such as poly(methyl methacrylate) (PMMA), to trap the SQs as monomers dispersed within the polymer matrix, illustrated in **Figure 22**. When molecular aggregation is impeded in films with PMMA, SQ molecules are primarily thought to exist as monomers, with varying orientation and distance between molecules. Calculations using a distribution of intermolecular distances and rotationally averaged intermolecular orientations have found that the intensity of the 0-1 vibronic absorption peak increases as the concentration of SQ increases.[149] This trend is shown in **Figure 22**. Thus, the increased intensity of this feature has been ascribed to the presence of SQ molecules that are randomly oriented but close enough to each other to be weakly electronically coupled.

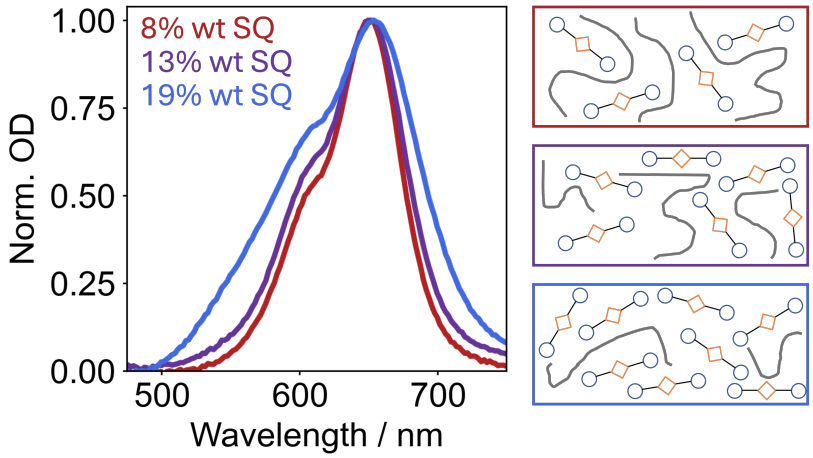


Figure 22. Linear absorbance spectra for DBSQ(OH)$_2$:PMMA films with varying wt% SQ and corresponding cartoons.

When unimpeded by PMMA, these SQ molecules forms slip-stacked H-aggregate stacks in thin films.[36] As SQ:PMMA thin films are thermally annealed, the populations of uncoupled and weakly-coupled monomers evolve into H-aggregates.[36,150] As the morphology of SQ films change, the excited-state dynamics also evolve. Previous transient absorption (TA) measurements of DBSQ(OH)$_2$:PMMA films before thermal annealing revealed energy transfer from monomer to weakly-coupled species and from monomer to H-aggregates.[149] However, the excited-state dynamics during thermal annealing remain unexplored. In the following sections, I discuss the measurements of evolving electronic structure and excited-state dynamics during thermal annealing using in situ linear absorption and single-shot transient absorption (SSTA) spectroscopy. By analyzing these data using a sequential decay kinetic model and an ICT Hamiltonian I have developed a molecular-level picture of the evolving intermolecular interactions during the aggregation process.

3.1 DHSQ(OH)$_2$

3.1.1 Experimental Details. A solution of 1.1 mg DHSQ(OH)$_2$ and 9.5 mg PMMA in 1 mL of chloroform was spin-cast onto a glass slide at 1500 RPM. The films were annealed from 90°C to 140°C, increasing by 10°C every 10 minutes, **Figure 23a**, on an electric hot plate with a slit in the middle, allowing light transmission for concurrent single-shot transient absorption (SSTA) and absorbance measurements. The pump (419 nJ) and the probe (10 nJ) were spread over an overlap region of ∼25 μm × 20 mm. SSTA and absorbance measurements were collected at 2 minutes and 58 minutes, which we refer to as pre- and post-annealing, respectively. Each SSTA measurement used a camera image size of 2560 × 180 pixels, and 3750 SSTA measurements were averaged over 60 s.

3.1.2 Linear Absorption. Absorbance spectra measured at 2 min and 58 min during annealing are shown in **Figure 23c** along with the pump spectrum. The height of the shoulder peak observed at 610 nm pre-annealing is attributed to weak Coulombic interactions between randomly oriented squaraine molecules. Even before annealing DHSQ(OH)$_2$:PMMA films, there are H-aggregates present, evidenced by the peak at 560 nm. Thermal annealing results in the formation of pi-stacked H-aggregates with absorbance at 560 nm and 648 nm.

3.1.3 Single-Shot Transient Absorption. The SSTA spectra measured pre- and post-annealing are shown in **Figure 24**. Before annealing, excitons are primarily photogenerated in monomers owing to their overlap with the pump spectrum. The pre-annealing spectrum exhibits a rapidly decaying ground state bleach (GSB) feature at 640 nm, corresponding to recovery of unexcited monomer. The rapid decay of signal at 640 nm and concomitant growth of the features at 610 nm and 560 nm suggests the migration of excitons from

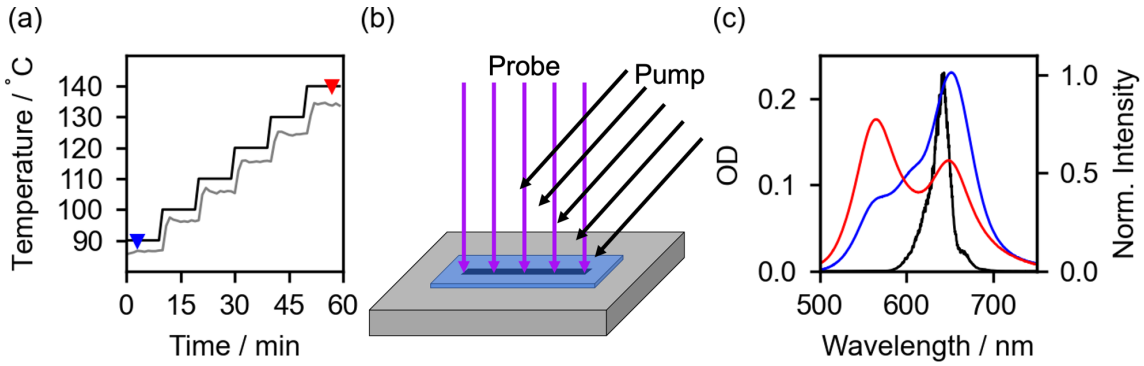


Figure 23. (a) Temperature ramp of stage (black) and top surface of a glass slide (grey). Triangles indicate when spectroscopic measurements were conducted. (b) A film (blue) on a heated sample stage with slit that allows pump (black) and probe (purple) to pass. (c) Pump spectrum (black) overlaid with absorbance of $DHSQ(OH)_2$:PMMA film at 2 min (blue) and 58 min (red).

initially photoexcited uncoupled monomers to weakly-coupled molecules and H-aggregates.[149] Stronger positive electronic coupling between pi-stacked SQ molecules with a smaller intermolecular distance results in a blue-shifted absorption peak and a decreased 0-0:0-1 peak ratio.[36,151] In a similar SQ molecule (with butyl side chains) H-aggregates were found to have a lower energy excited state with substantial intermolecular CT character, owing to the proximity of the nitrogen atoms to the squarylium rings of neighboring molecules in the aggregate. This type of CT state is mixed with the excitonic state, giving it enough oscillator strength to produce a peak at 648 nm in absorbance spectra, overlapping with the monomer peak.[43] Energy transfer is expected from the initially excited uncoupled monomers to weakly-coupled monomers and to pi-stacked H-aggregates. Exciton population in each of these SQ configurations will bleach the optical transitions observed in their linear absorbance spectra. The growth of these bleach features and the decay of the main monomer peak at 640 nm as a function of pump-probe delay time is apparent in the TA spectrum of the pre-annealed film, **Figure 24a**.

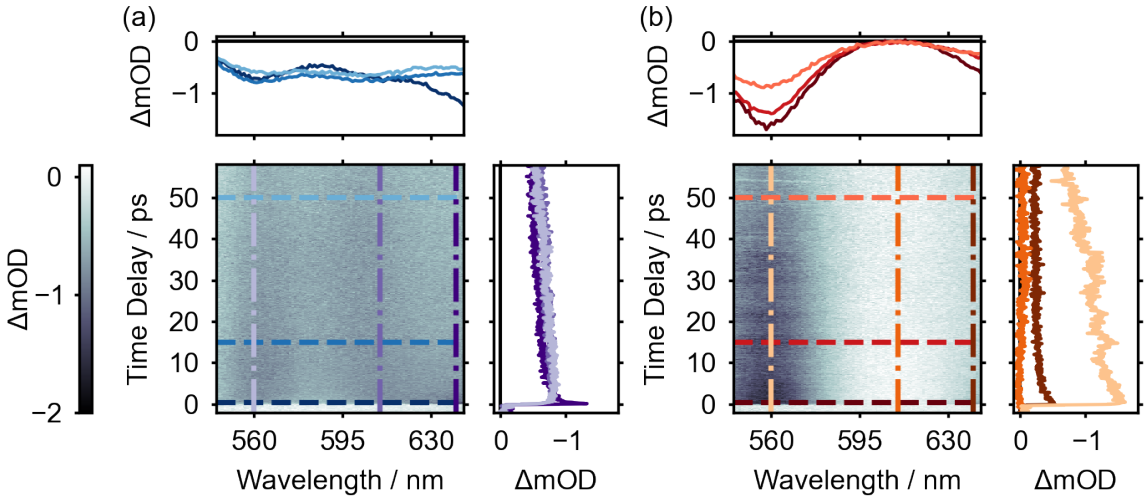


Figure 24. SSTA measured at (a) 2 min and (b) 58 min. Above, spectral slices at pump-probe time delays of 0.2-0.5 ps, 14.5-15.5 ps, and 49.5-50.5 ps. On the right, transients at 560 nm, 610 nm, and 640 nm.

In the post-annealing spectrum, the features ascribed to both the uncoupled and weakly coupled monomer at 640 nm and 610 nm, respectively, have almost vanished and a strong GSB signal ascribed to H-aggregates is observed at 560 nm.[36] Growth of the H-aggregate and shoulder features is not observed in the SSTA spectrum of the post-annealed film, **Figure 24b**. This film is expected to be comprised of almost entirely pi-stacked H-aggregates, and the laser excitation is resonant with their lower-energy CT state. Thus, the excitons can be directly photogenerated in H-aggregates in post-annealed films.

3.1.4 Kinetic Modeling. The observations described above motivate the kinetic model pictured in **Figure 25**. Three separate models are used to describe the different film morphologies during thermal annealing. The first model represents regions of the film without pi-stacked H-aggregates and the last model describes regions of the film with only H-aggregates and without monomers. The second model describes film regions with a population of uncoupled monomers,

weakly-coupled monomers, and pi-stacked H-aggregates in close enough proximity for energy transfer.

The model without pi-stacked H-aggregates, **Figure 25a**, includes the excitonic state of SQ monomers that are uncoupled and weakly coupled to other monomers, S^u_{10} and S^w_{10}, respectively, and their ground states, S^u_{00} and S^w_{00}. Excitons can recombine from either excited state with rates of k^u_{1-0} and k^w_{1-0} for the uncoupled and weakly-coupled monomers, respectively, and energy can transfer from the uncoupled to the weakly-coupled monomers with a rate of k^{u-w}. The second model, **Figure 25b**, duplicates the first model, but also includes the pi-stacked H-aggregate excited state, S^π_1, and ground state, S^π_0. The rate of energy transfer from monomers to pi-stacked H-aggregates is $k^{u-\pi}$. Reverse transitions were not necessary to adequately replicate the trends in the data, so these transitions were excluded. The third model, **Figure 25c**, only considers pi-stacked H-aggregates. The S^π_1 state, with a similar energy to that of the S^u_{10} state, has been attributed to an intermolecular CT state within the pi-stacked H-aggregate[43].

The master equations used to describe the models are:

$$\begin{bmatrix} \frac{dS^u_{10}}{dt} \\ \frac{dS^u_{00}}{dt} \\ \frac{dS^w_{10}}{dt} \\ \frac{dS^u_{00}}{dt} \end{bmatrix} = \begin{bmatrix} -(k^u_{1-0} + k^{u-w}) & 0 & 0 & 0 \\ k^u_{1-0} & 0 & 0 & 0 \\ k^{u-w} & 0 & -k^w_{d-0} & 0 \\ 0 & 0 & k^w_{d-0} & 0 \end{bmatrix} \begin{bmatrix} S^u_{10} \\ S^u_{00} \\ S^w_{10} \\ S^u_{00} \end{bmatrix} \tag{3.1}$$

$$\begin{bmatrix} \frac{dS_{10}^{u}}{dt} \\ \frac{dS_{00}^{u}}{dt} \\ \frac{dS_{10}^{w}}{dt} \\ \frac{dS_{00}^{u}}{dt} \\ \frac{dS_{1}^{\pi}}{dt} \\ \frac{dS_{0}^{\pi}}{dt} \end{bmatrix} = \begin{bmatrix} -(k_{1-0}^{u} + k^{u-w} + k^{u-\pi}) & 0 & 0 & 0 & 0 & 0 \\ k_{1-0}^{u} & 0 & 0 & 0 & 0 & 0 \\ k^{u-w} & 0 & -k_{d-0}^{w} & 0 & 0 & 0 \\ 0 & 0 & k_{d-0}^{w} & 0 & 0 & 0 \\ k^{u-\pi} & 0 & 0 & 0 & -k_{1-0}^{\pi} & 0 \\ 0 & 0 & 0 & 0 & k_{1-0}^{\pi} & 0 \end{bmatrix} \begin{bmatrix} S_{10}^{u} \\ S_{00}^{u} \\ S_{10}^{w} \\ S_{00}^{u} \\ S_{1}^{\pi} \\ S_{0}^{\pi} \end{bmatrix} \tag{3.2}$$

$$\begin{bmatrix} \frac{dS_{1}^{\pi}}{dt} \\ \frac{dS_{0}^{\pi}}{dt} \end{bmatrix} = \begin{bmatrix} -k_{1-0}^{\pi} & 0 \\ k_{1-0}^{\pi} & 0 \end{bmatrix} \begin{bmatrix} S_{1}^{\pi} \\ S_{0}^{\pi} \end{bmatrix} \tag{3.3}$$

Equation 3.1 describes the monomer and weakly-coupled model, **Equation 3.2** describes all species, and **Equation 3.3** is the pi-stacked model. The one dimensional matrix on the left-hand side of each equality is the change in the population of each relevant state during timestep t, while the matrix on the far right is their current population. To construct the initial populations we assume that all excitons are initially photogenerated in uncoupled monomers for model 1. In model 2, it is assumed that there is a starting population of excitons in pi-stacked H-aggregates and uncoupled monomers. Model 3 has the population of excitons starting as only in pi-stacked H-aggregates.

A weighted sum of the three models is used to simulate the population dynamics. The weights of the models were assigned based on three-Gaussian fits of the absorbance spectra. The fraction of pi-stacked molecules was estimated as the ratio of the height of the 560 nm peak compared to the maximal height of the feature, occurring at the latest time point where full aggregation was assumed. The weight of the first model was set as the fraction of molecules that are not pi-stacked. The fraction of the remaining molecules that were weakly coupled

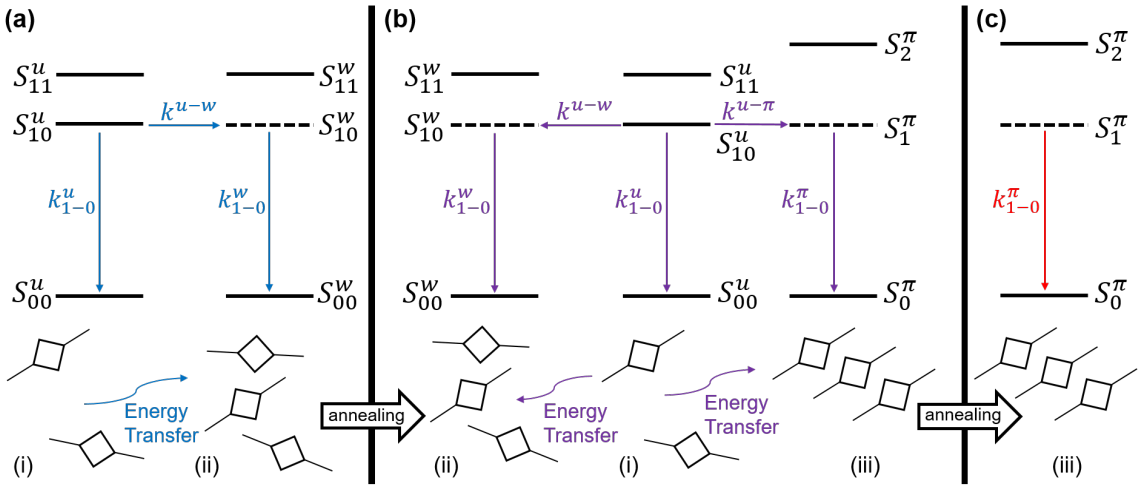


Figure 25. The kinetic model for (a) uncoupled and weakly-coupled monomers, (b) uncoupled, weakly-coupled, and pi-stacked molecules, (c) isolated pi-stacked molecules. States with lower oscillator strength shown in dashed lines. Cartoons illustrate the species present. Higher energy excited states that do not participate in the kinetic model but are bleached in the calculated TA spectra are also pictured. Model parameters reported in text. The grey dashed arrows indicate transitions that were excited by the 640 nm pump pulse.

was determined by the height of the shoulder feature at 610 nm compared to its maximal height. The weight of the second model was set to be the fraction of weakly coupled molecules, with the weight of the third model being one minus the other two weights.

All features observed in the TA spectra are assumed to originate from GSB. All transitions shown in **Figure 25** as well as transitions from the respective ground states to the S_{11}^u, S_{11}^w, and S_2^π states are bleached. The intensity of the bleach is derived from the populations of each state and the peak ratios, discussed below. With the first and second model, the first vibronic state for the monomers is also bleached, which gives rise to the shoulder feature at 610 nm. In the second and third models, the H-aggregate absorbance feature at 560 nm is also bleached when there is excited H-aggregate population. Simulated TA spectra are calculated

by using the populations of each electronic state from the kinetic model to weight the amplitude of Gaussian line shapes centered at the wavelengths of features in the linear absorbance spectrum. The population of S_{10}^{u} bleaches both the $S_{10}^{u} \leftarrow S_{00}^{u}$ and $S_{10}^{w} \leftarrow S_{00}^{w}$ transitions, so this population weights the amplitude of Gaussians centered at 640 nm and 610 nm. The relative intensity of these two features was assumed to be 1:0.2, estimated from computations by Zheng et al.[149] Similarly, the population of S_{10}^{w} bleaches both the $S_{10}^{u} \leftarrow S_{00}^{u}$ and $S_{10}^{w} \leftarrow S_{00}^{w}$ transitions, so this population also weights the amplitude of Gaussians centered at 640 nm and 610 nm, this time with a relative intensity of 1:0.65 estimated from Zheng et al[149]. The population in S_{1}^{π} bleaches both the $S_{10}^{u} \leftarrow S_{00}^{u}$ and $S_{1}^{\pi} \leftarrow S_{0}^{\pi}$ transitions, so this population weights the amplitude of Gaussians centered at 640 nm and 560 nm, with relative intensities of 0.3:1, estimated from the absorption spectrum of the post-annealed film. The precise center-wavelengths and broadening parameters were extracted from three-Gaussian fits of the absorbance spectra.

Figure 26a shows TA spectra averaged from 0.2-0.5 ps, 14.5-15.5 ps, and 49.5-50.5 ps for a DHSQ$(OH)_2$:PMMA film measured at 2 min and 58 min during thermal annealing. **Figure 26b** depicts transients simulated using the models described above at 0.3 ps, 15 ps, and 50 ps. A best-fit of the rates and relative weights of the three models has not yet been obtained, and the simulated spectra shown here are merely utilizing user-defined guesses. A time constant of 500 ps was selected for the transition anticipated to have lower oscillator strength ($S_{10}^{w} \leftarrow S_{00}^{w}$) and shorter time constants (60 ps and 40 ps) were assumed for the $S_{1}^{\pi} \leftarrow S_{0}^{\pi}$ and $S_{10}^{u} \leftarrow S_{00}^{u}$ transitions, respectively. Even without a best-fit, there is general agreement between the model and the experimental data. Increased signal intensity at 610 nm in the SSTA spectrum of the film pre-annealing is evidence of energy

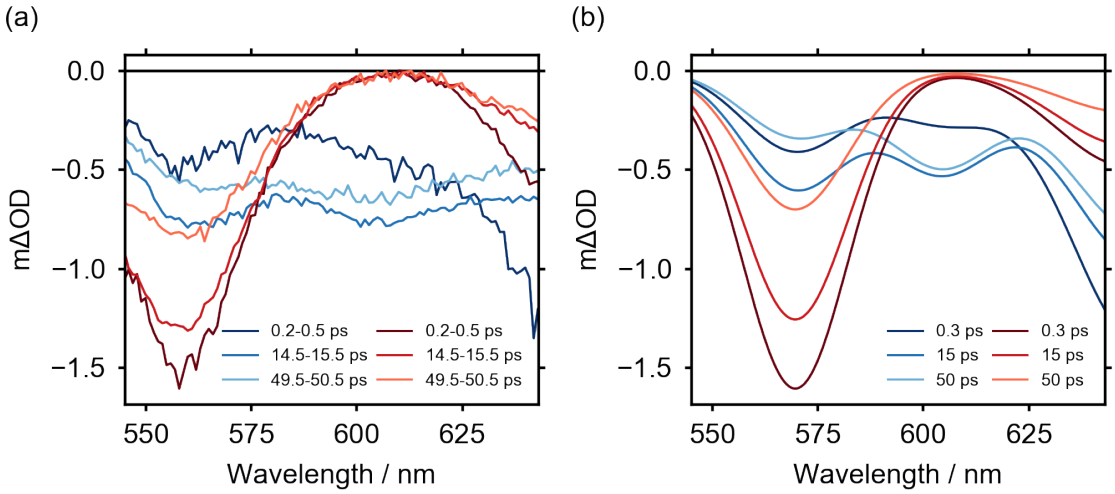


Figure 26. SSTA spectra measured at 2 min (pre-annealing, blue) and 58 min (post-annealing, red). (b) Simulated spectra at the same pump-probe time delays. The same parameters were used for shared transitions in multiple models: $\tau^{u}_{1-0} =$ 40 ps, $\tau^{w}_{1-0} = 500$ ps, $\tau^{\pi}_{1-0} = 60$ ps, $\tau_{u-w} = 5$ ps, $\tau_{u-\pi} = 5$ ps. Weights of model 1 : model 2: model 3 are 0.47:0.29:0.24 at 2 min and 0.00:0.30:0.70 at 58 min.

transfer from the excited uncoupled monomers to the weakly coupled monomers. Similarly, the 560 nm feature represents GSB of pi-stacked aggregates as a result of energy transfer from photoexcited monomer to the aggregates. The 5 ps value selected for τ_{u-w} and $\tau_{u-\pi}$ in our model is a reasonable rate for FRET between an organic donor-acceptor pair.[152] Post-annealing, the SSTA spectrum displays the bleach features associated with H-aggregates immediately after photoexcitation, suggesting that excitons are directly photogenerated in the pi-stacked H-aggregates in these films. Reasonable agreement between the experimental and simulated spectra was attained when assuming that the third model, with only pi-stacked H-aggregates, is dominant for the post-annealed film. However, inclusion of the second model is required to account for slower initial decay of the H-aggregate feature than would be expected for pure H-aggregates.

Further refinement of the model and the identification of best-fit parameters may yield better agreement for the relative magnitudes of the three primary spectral features. One major weakness of this model is trying to determine the absorption spectra for all the species present. The next section describes a kinetic model that returns the spectra of species present.

3.2 DBSQ(OH)$_2$

3.2.1 Experimental Details. Solutions of DBSQ(OH)$_2$: PMMA in chloroform were made with concentrations of 1.2: 15.5 mg/mL (8% wt SQ). ~0.3 mL aliquots were spin cast (Ossila spin coater) onto glass slides at 2000 RPM for 20 s. Prior to spin coating, glass slides were scrubbed with acetone. Films were placed on a homebuilt electric heating stage with a slit that allows for in situ optical measurements. Concurrent absorption and single-shot transient absorption (SSTA) measurements of DBSQ(OH)$_2$:PMMA films were collected at the time points indicated in the heating ramp shown in **Figure 27b**. The temperature ramp begins at a temperature where minimal annealing was shown to occur. The temperature is ramped by 5-10°C every 5 minutes and ends at a temperature where the film was fully annealed. Stage temperature was monitored every minute by recording the temperature setting of the stage and slide temperature was measured every minute during the heating ramp using an IR thermometer (FLIR TG54 Spot Infrared Thermometer) with the emissivity set to 0.95. SSTA images collected were 2560 x 180 pixels, averaged over 30 seconds of measurement time. The wavelength range for each image was 522 nm to 691 nm. The pump and probe energy used for these measurements were 283 nJ and 10 nJ, respectively.

3.2.2 Linear Absorption. The absorbance of a DBSQ(OH)$_2$:PMMA film (8% wt SQ) was measured while the temperature was increased as shown in

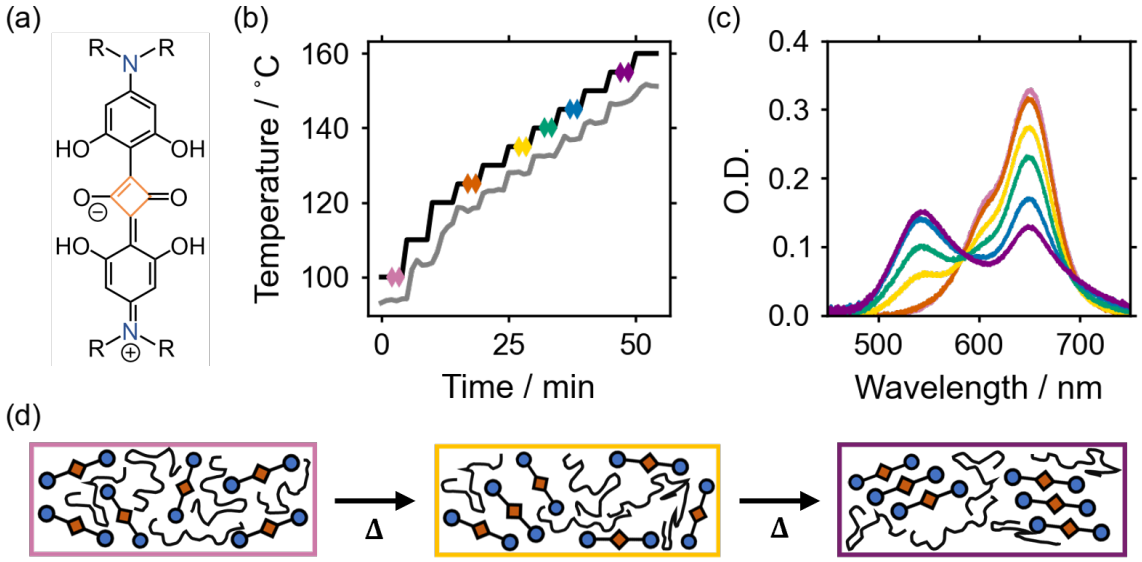


Figure 27. (a) Structure of DBSQ(OH)$_2$ (R=Bu) with the electron accepting squarylium ring in orange and the nitrogen-containing electron donating arms in blue. (b) Heating stage temperatures (black) and slide temperatures (grey) are plotted over annealing time. Scans marked with colored diamonds in (b) at 100°C (pink), 125°C (orange), 135°C (gold), 140°C (green), 145°C (blue), 155°C (purple) correspond to linear absorption of an 8% wt SQ film in panel (c). (d) Cartoon of uncoupled monomer, weakly-coupled monomer, and slip-stacked H-aggregate at three different temperatures.

Figure 27b. The absorption spectra (**Figure 27c**) at the beginning of annealing primarily show absorption from the monomer at ∼660 nm, with a small shoulder at ∼600 nm. These two peaks correspond to the 0-0 and 0-1 vibronic transitions for uncoupled monomers.[149] As the weight percentage of $DBSQ(OH)_2$ is increased, the amplitude of the 0-1 feature grows relative to the 0-0 feature, indicating a larger population of weakly H-coupled monomers.[149,150] This trend shows that coupling and H-aggregation are impeded in as-cast films by the addition of PMMA. While both uncoupled and weakly-coupled monomers absorb at both ∼660 nm and ∼600 nm, their peak intensity ratios differ. For simplicity, the features at ∼660 nm and ∼600 nm will be ascribed to uncoupled and weakly-coupled monomers, respectively, for the remainder of the manuscript. As annealing proceeds, a decline of the uncoupled and weakly-coupled monomer features is observed concurrently with growth of the double-hump CT-HA spectrum, revealing that uncoupled and weakly-coupled monomer populations are forming CT-HA species. A clear isosbestic point is observed at ∼585 nm providing evidence for conversion between species.

3.2.3 Single-Shot Transient Absorption. Using pump pulses centered at 665 nm, SSTA was measured concurrently with absorbance, using the heating scheme described in **Figure 27b**. Prior to annealing, ground state bleach (GSB) of the uncoupled and weakly-coupled monomer appears at ∼670 nm and ∼600 nm (**Figure 28a**). A rise of the signal at ∼600 nm occurring simultaneously with the decay of the feature at ∼670 nm is observed during the first ∼3 ps of the excited-state dynamics (**Figure 28b**) and is attributed to energy transfer from uncoupled monomers to weakly-coupled monomers[149,150]. The final scan collected in the annealing experiment reveals GSB signal from the CT-HA at ∼540

nm and ∼670 nm, with almost no remaining signal at ∼600 nm (**Figure 28c,d**). Previously reported TA spectra of neat DBSQ(OH)$_2$ films, which consist primarily of H-aggregates, indicate the presence of a weak excited-state absorption (ESA) transition at ∼620 nm.[153] This ESA feature overlaps with GSB in neat films of DBSQ(OH)$_2$, resulting in minimal observed TA signal. When weakly-coupled monomers are present, as in our spectra measured prior to annealing, the ESA feature is completely obscured by the negative GSB signal from these weakly-coupled monomers. As the population of weakly-coupled monomers decreases during annealing, the negative GSB signal from monomers diminishes, leaving the ESA and GSB from the H-aggregates, which balance each other to yield near-zero TA signal (**Figure 28**).

The pump, centered at 665 nm, excites H-aggregates at the lower-energy CT-HA peak (∼670 nm), resulting in a slower decay compared to measurements before annealing. When aggregates are excited via the lower-energy CT-HA state, the transition to the higher-energy CT-HA state will also be bleached, resulting in the TA signal observed at 540 nm. Since the population of monomers and weakly-coupled species is insignificant (*vide infra*), energy transfer from monomers to H-aggregates is not observed, and the GSB recovers without any further energy transfer.

3.2.4 Kinetic Modeling. The SSTA measurements during thermal annealing were fit to evolution associated decay spectra (EADS)[154] that model two species with two sequential decays (**Equation 3.4**), where A_1 and A_2 each represent an amplitude spectrum as described below:

$$\Delta OD(t,\lambda) = A_1(\lambda)e^{-k_1 t} + A_2(\lambda)\left(\frac{k_1}{k_2 - k_1}e^{-k_1 t} + \frac{k_1}{k_1 - k_2}e^{-k_2 t}\right) \qquad (3.4)$$

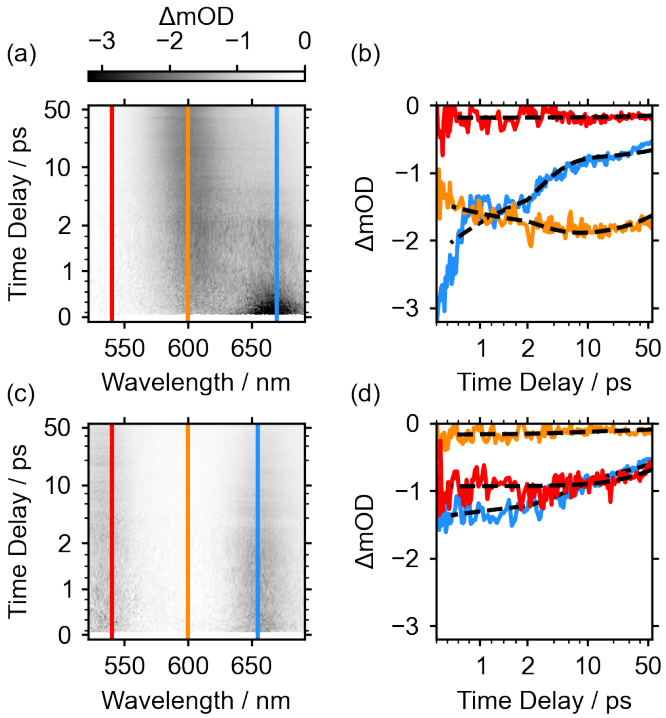


Figure 28. SSTA of an 8% wt SQ film taken at 2 min, 100°C (a) and at 53.5 min, 160°C (c) during thermal annealing. Transients from (a) are plotted at 540 nm (red), 600 nm (orange), and 670 nm (blue) in (b). Transients from (c) are plotted at 540 nm (red), 600 nm (orange), and 655 nm (blue) in (d). Data were logarithmically binned into 100 bins along the time delay axis. Fits to transients (dashed black) start at 400 fs.

For this model, the first species is excited by the pump pulse and undergoes energy transfer with rate k_1 to a second species, which decays to the ground state with rate k_2. This model is used for all SSTA data over the course of annealing, producing $A_1(\lambda)$ and $A_2(\lambda)$ spectra and k_1 and k_2 rates as a function of annealing time. The EADS fits began at 400 fs as shorter time delays are likely too early to be able to discern the intermolecular energy transfer.

The A_1 and A_2 spectra before annealing correspond to the spectra of the monomer and weakly-coupled species, respectively. The amplitude spectrum for the first species (A_1) shows much higher signal from uncoupled monomer (∼670 nm) and decays within ∼2 ps (**Figure 29a**). A_2 primarily has signal from weakly-coupled species and decays within ∼200 ps (**Figure 29d**). As annealing proceeds, A_1 loses intensity from monomers and gains intensity from the higher energy CT-HA state (∼540 nm), owing to direct pump excitation. There is a similar trend with a growth observed in A_2 of the higher energy CT-HA that corresponds with a loss in intensity from weakly-coupled species. Thus, these EADS spectra show that energy transfer from the monomer to weakly-coupled species dominates until the population of H-aggregates increases during thermal annealing.

Both A_1 and A_2 exhibit a double-humped spectrum at the end of annealing, implying that the pump initially photogenerates excitons in H-aggregates with the spectrum of A_1, and these excitons then decay to a different population of H-aggregates with spectrum A_2. The pump may also excite any remaining monomers or weakly-coupled species in the sample. The spectral overlap of the lower-energy CT-HA feature and primary uncoupled monomer feature at ∼670 nm makes it difficult to ascertain the relative contribution of the two types of species, but the signal at ∼600 nm can help, since it more distinctly represents weakly-coupled

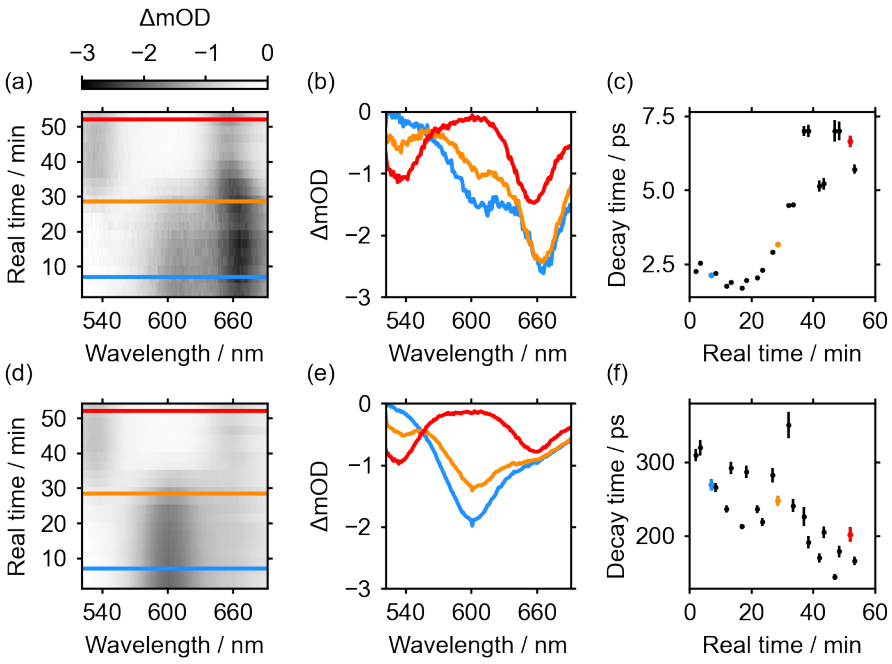


Figure 29. A_1 (a) and A_2 (d) from EADS fits of SSTA data from a low weight percent SQ film as a function of annealing time. Spectral slices from (a,d) are plotted at 7 min, 110°C (blue), 28.5 min, 130°C (orange), and 52 min, 160°C (red) in panels (b,e). Corresponding time constants from A_1 (c) and A_2 (f) as a function of annealing time.

monomers. As discussed above, if uncoupled or weakly-coupled monomers were present, the negative GSB signal at ∼600 nm from the monomers would dominate over the positive ESA feature from H-aggregates at ∼620 nm. When only H-aggregates are present, the ESA and GSB features nearly cancel to yield minimal observed signal. The near-zero TA signal at ∼600 nm in A_1 and A_2 indicates an absence of either uncoupled or weakly-coupled monomers after thermal annealing. This result shows the necessity of SSTA and EADS modeling for understanding phase separation in thin films with more than one component, such as bulk heterojunctions.

After annealing has finished, DBSQ(OH)$_2$:PMMA films have a population that primarily consists of slip-stacked H-aggregates, as indicated by the presence of a double-hump spectrum in both A_1 and A_2 from the EADS fits (**Figure 29**). Since no monomers remain in the system, the changing ratio of the higher energy to lower energy CT-HA states likely results from changing interplanar spacing within the H-aggregates. If less PMMA resides between monomers within an H-aggregate, a decrease in average interplanar spacing would be observed. This would lead to a stabilization of the dark CT state (i.e. a decrease in the energy of this stationary state) and a destabilization of the H-aggregate bright state (i.e. an increase in the energy of this stationary state). Since the oscillator strength of the mixed CT-H-aggregate (CT-HA) states originates solely from the H-aggregate bright state, the CT-HA state that is closer in energy to the H-aggregate bright state has a larger oscillator strength.[43] Therefore, as the CT state decreases in energy and the HA state increases in energy, the higher (lower) energy CT-HA state has more (less) oscillator strength. Thus, in a linear absorption spectrum, a larger high:low energy CT-HA peak amplitude ratio corresponds to smaller

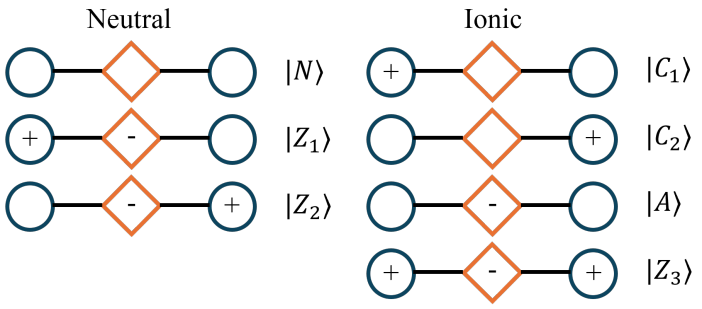


Figure 30. Cartoon of neutral and ionic adiabatic basis states.

interplanar spacing. The CT-HA high:low energy ratio is about ∼0.7 for A_1 and ∼1.2 for A_2 (**Figure 29b,e**), confirming that A_2 has more tightly packed monomers within a slip-stacked H-aggregate. This destabilizes the HA state and stabilizes the CT state compared to A_1.

3.2.5 Intermolecular Charge Transfer Hamiltonian. To quantitatively understand the influence of intermolecular packing on electronic structure, the absorption spectra and EADS spectra were modeled with an ICT Hamiltonian based on the essential states model (ESM)[155]. The ESM has been previously applied to simulate linear absorption of D-A-D systems including squaraines[37,43,155–157]. A diabatic basis for the monomer states is created using the ESM, which includes the neutral (N) and zwitterionic (Z_1, Z_2) states (**Figure 30**). The subscripts 1 and 2 denote the nitrogen-containing SQ arm that hosts the positive charge in the zwitterion. The ESM has previously been extended[36] to include the possible ionic monomer states that can appear in a dimer. Each arm can host a cation (C_1, C_2) or the center can host a negative charge (A). Alternatively, both arms and the center can be charged to form a zwitterion (Z_3) with net +1 charge.

Neutral monomer states or ionic monomer states form the resultant neutral dimer states. The dimer states are direct products of the monomer states, with the

overall charge of the dimer state being neutral. Neutral dimer states are composed of neutral monomer states and ionic dimer states are composed of ionic monomer states. The full ICT Hamiltonian is a sum of the monomer, charge separated, Coulombic, and intermolecular charge transfer terms, where the sum is over all molecules, n:

$$\hat{H} = \sum_{n} \hat{H}_{n}^{mon} + \hat{H}^{CS} + \hat{V} + \hat{H}^{inter} \tag{3.5}$$

The overall monomer term is a sum of the electronic, vibrational, and vibronic terms. The electronic term for the monomer (**Equation 3.6**) includes the energy of the neutral zwitterionic states (η_z) and the intramolecular charge transfer integral (t_z):

$$\hat{H}_{n}^{mon,el} = \eta_z \sum_{a=1,2} |Z_{a,n}\rangle \langle Z_{a,n}| - t_z \sum_{a=1,2} (|N_n\rangle \langle Z_{a,n}| + h.c.) \tag{3.6}$$

This equation is summing over the arms (a) in the D-A-D molecule. The intramolecular charge transfer term accounts for the transfer of an electron from the donor arms to the acceptor center on the D-A-D molecules, and the reverse process. The vibrational term (**Equation 3.7**) is defined in terms of the raising and lowering operators ($b_{a,n}^{\dagger}$, $b_{a,n}$) and the vibrational energy $\hbar\omega_{vib}$, and contributes for both the neutral and ionic states:

$$\hat{H}_{n}^{mon,vib} = \hbar\omega_{vib} \sum_{a} b_{a,n}^{\dagger} b_{a,n} \tag{3.7}$$

The vibronic term for the monomer (**Equation 3.8**) is defined in terms of the raising and lowering operators and the Huang-Rhys factor (λ^2):

$$\hat{H}_{n}^{mon,vibron} = \hbar\omega_{vib}\lambda \sum_{a} (b_{a,n}^{\dagger} + b_{a,n} + \lambda) |Z_{a,n}\rangle \langle Z_{a,n}| \tag{3.8}$$

The Huang-Rhys parameter accounts for the nuclear shift for the zwitterionic states relative to the neutral state. The charge separation term

(**Equation 3.9**) includes the energies of the ionic states (η_{CT}) and intramolecular charge transfer:

$$\hat{H}^{CS,el} = \eta_{CT} \sum_{n} |A_n\rangle \langle A_n| + \eta_z \sum_{n} |Z_{3,n}\rangle \langle Z_{3,n}| - t_z \sum_{a,n} (|Z_{3,n}\rangle \langle C_{a,n}| + h.c.) \quad (3.9)$$

The intramolecular charge transfer in **Equation 3.9** accounts for the transfer of an electron from the donor arm that the cation is not on to the acceptor center, and the reverse process. The vibrational component for the charge separation term is accounted for with **Equation 3.7**. The vibronic terms for the charge separated Hamiltonian are:

$$\begin{aligned} \hat{H}^{CS,vibron} = {} & \hbar\omega_{vib}\lambda \sum_{a,n} (b^{\dagger}_{a,n} + b_{a,n} + \lambda) |Z_{3,n}\rangle \langle Z_{3,n}| \\ & + \hbar\omega_{vib}\lambda_{CT} \sum_{a,n} (b^{\dagger}_{a,n} + b_{a,n} + \lambda_{CT})(|C_{a,n}\rangle \langle C_{a,n}| + |A_n\rangle \langle A_n|) \end{aligned} \quad (3.10)$$

Within the vibronic term (**Equation 3.10**), the Huang-Rhys factor (λ^2) accounts for the nuclear shift for the zwitterionic state ($|Z_{3,n}\rangle$) compared to the neutral state. The charge transfer Huang-Rhys factor (λ^2_{CT}) is defined for the cation and anion states and describes the nuclear shift compared to the neutral state. The monomer and CS Hamiltonian terms are combined and diagonalized to yield the adiabatic states. The Coulombic and intermolecular charge transfer terms are treated as a perturbation to the diagonalized Hamiltonian from the monomer and CS terms.

The Coulombic term (**Equation 3.11**) accounts for Coulombic attraction and repulsion between charged sites on the monomers in an aggregate:

$$\hat{V} = \frac{1}{4\pi\epsilon\epsilon_0} \sum_{S} \sum_{n>m} \sum_{q_n(S),q_m(S)} \frac{q_n(S) q_m(S)}{|\mathbf{r_{q_n}}(S) - \mathbf{r_{q_m}}(S)|} |S\rangle \langle S| \quad (3.11)$$

This equation sums over the states (S), over all molecules n and m in an aggregate, and all charged sites on molecules n and m for a given state (S).

Charges on sites for molecules n and m are given by $q_n(S)$ and $q_m(S)$, respectively. The distance between the sites is $|\mathbf{r_{q_n}}(S) - \mathbf{r_{q_m}}(S)|$, ϵ_0 is the vacuum permittivity, and $\epsilon = 3$ is the dielectric constant. The distance calculations involve the length of the squaraine arm (l), the slip-stack distance (x), in-plane shift (y), and interplanar spacing (z) distances between the sites. The intermolecular charge transfer term (**Equation 3.12**) couples the neutral and ionic dimer states with the intermolecular charge transfer integral (t_{CT}):

$$\begin{aligned}\hat{H}^{inter} = -t_{CT} \sum_n (&|N_n N_{n+1}\rangle \langle A_n C_{1,n+1}| + |N_n N_{n+1}\rangle \langle C_{2,n} A_{n+1}| + |A_n C_{1,n+1}\rangle \langle Z_{2,n} Z_{1,n+1}| \\ &+ |C_{2,n} A_{n+1}\rangle \langle Z_{2,n} Z_{1,n+1}| + |Z_{1,n} Z_{1,n+1}\rangle \langle C_{1,n} A_{n+1}| + |Z_{2,n} Z_{2,n+1}\rangle \langle A_n C_{2,n+1}| \\ &+ |Z_{3,n} A_{n+1}\rangle \langle Z_{1,n} N_{n+1}| + |A_n Z_{3,n+1}\rangle \langle N_n Z_{2,n+1}| + h.c.)\end{aligned} \tag{3.12}$$

The states paired in the above equation describe the movement of an electron from one monomer to another monomer in a neutral dimer state (overall charge of zero), to form an ionic dimer state, or the reverse. The parameters used for the fit were $\eta_z = 0.69$ eV, $t_z = 1.05$ eV, $\hbar\omega_{vib} = 0.16$ eV, $\eta_{CT} = 1.37$ eV, $\lambda^2 = 1$, $\lambda_{CT}^2 = 0.5$ eV, $l = 6.60$ Å, $x = 3.47$ Å, $y = 1.84$ Å, and 2 vibrational quanta. Gaussian broadening of 24 nm and an overall spectral shift of 0.045 eV was applied. The x and y values between monomers were taken from reports of crystal structure.[43]

Both the Coulombic and the intermolecular charge transfer terms are treated as a perturbation to determine how the original states are impacted. Coulombic attraction arises from interactions of charged sites of neighboring monomers, which are highly dependent on intermolecular packing. With the Coulombic term, the energy of the first CT state stabilizes as the interplanar spacing (z) between molecules decreases. The CT state becomes degenerate with

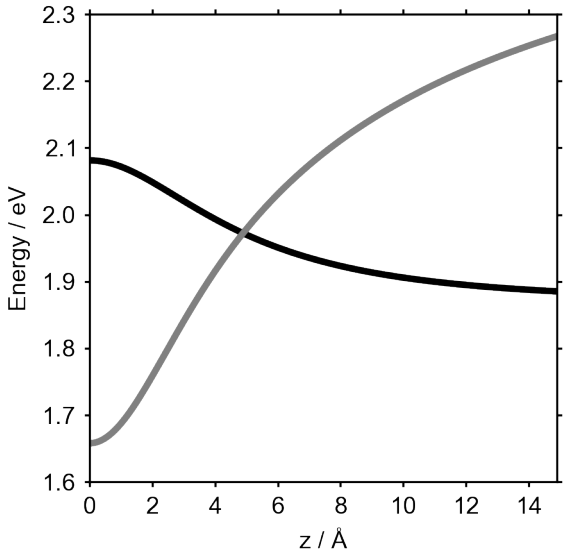


Figure 31. Energy of the HA (black) and CT (grey) states as a function of interplanar spacing (z), before mixing with the intermolecular charge transfer term.

the HA state at an interplanar spacing value of 5 Å. Further reduction in the interplanar spacing causes the CT state to shift lower in energy relative to the H-aggregate state (**Figure 31**). The intermolecular charge transfer term effectively couples the neutral and the ionic dimer states through the charge transfer integral (t_{CT}). The inclusion of the intermolecular charge transfer term leads to the formation of a new feature at ∼550 nm.

The linear absorption spectra were fit using the ICT Hamiltonian to reveal how interplanar spacing changes with annealing. As the molecules form aggregates in a thin film, the interplanar spacing (z) would be expected to decrease. Simultaneously, the intermolecular electron transfer integral (t_{CT}) would be expected to increase, as electron transfer becomes more probable as monomers become closer. Both the interplanar spacing and intermolecular charge transfer integral were extracted by best-fitting to experimental spectra. The measured linear absorption spectra from the start of H-aggregation to the end of annealing

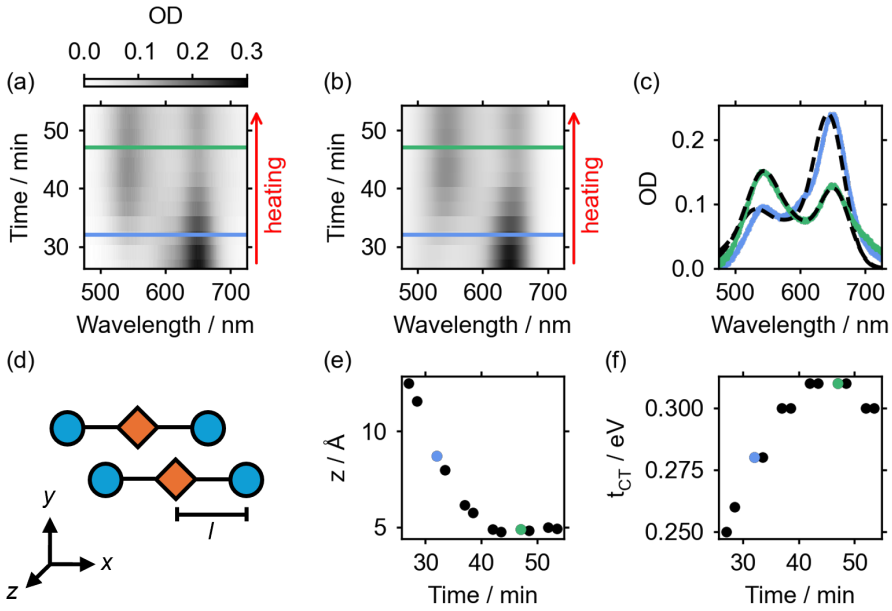


Figure 32. Linear absorbance data (a) and fits from the ICT Hamiltonian (b) shown from 27 min (100°C) to 53.5 min (160°C). Slices from (a,b) are plotted at 32 min, 110°C (blue) and 47 min, 155°C (green) in (c). Fits are shown as a dashed black trace compared to the data. (d) Slip-stacked SQ dimer cartoon with listed Cartesian axis and arm length (l). (e) Interplanar spacing and (f) intermolecular charge transfer integral as a function of thermal annealing.

were well-fit with the ICT Hamiltonian. **Figure 32** illustrates that the interplanar spacing is initially ∼10 Å when H-aggregates begin to form. As annealing proceeds, the interplanar spacing decreases until all monomers and weakly-coupled aggregates have been converted to H-aggregates. In addition to the interplanar spacing decrease, t_{CT} was found to increase with annealing, indicating more probable electron transfer.

The EADS spectra in our measured wavelength range are entirely negative and primarily report on the GSB of excited molecules and aggregates. We compare the positive amplitudes of A_1 and A_2 to the absorbance spectra modeled by the ICT Hamiltonian. The final H-aggregate spectra from EADS were fit using the same parameters described above for the linear absorbance, except for t_{CT},

	A_1	A_2
t_{CT} (eV)	0.34	0.38
Broadening (eV)	16	18
Spectral shift (eV)	0.026	0.034

Table 1. EADS spectra fit parameters for ICT Hamiltonian.

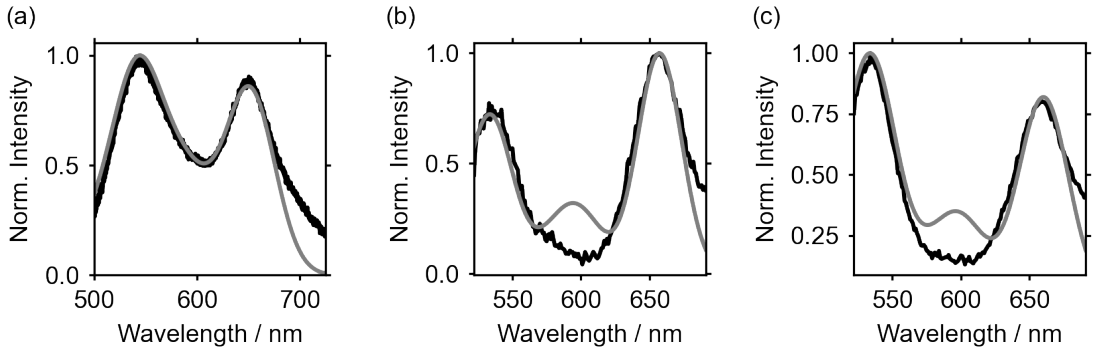


Figure 33. (a) Linear absorbance, (b) A_1, (c) A_2 measured at 52 min (160°C). Fits of ICT Hamiltonian (grey) to measured spectra (black) provide interplanar spacing of 4.98 Å, 6.15 Å, and 4.76 Å, respectively.

broadening, and the spectral shift, which are listed in **Table 1**. Both EADS spectra were well fit and compared with linear absorption in **Figure 33**.

Both fits to EADS spectra have smaller broadening and larger t_{CT} compared to the linear absorption, leading to a distinct vibronic feature at ∼600 nm that is obscured in the linear absorption fits (**Figure 34**). The EADS amplitude spectra for H-aggregates exhibits minimal TA signal at 600 nm owing to the overlap between GSB and ESA features, as discussed above. However, since the ICT Hamiltonian only simulates absorbance transitions from the ground state (i.e. GSB) and not ESA, a positive absorptive feature remains at 600 nm in the modelled spectra. As predicted, the species represented by A_2 has a smaller interplanar spacing (4.76 Å) compared to A_1 (6.15 Å). The linear absorption spectrum is best fit with an interplanar spacing value (4.98 Å) that is in between the values for A_1 and A_2, representing an average value for the interplanar spacing

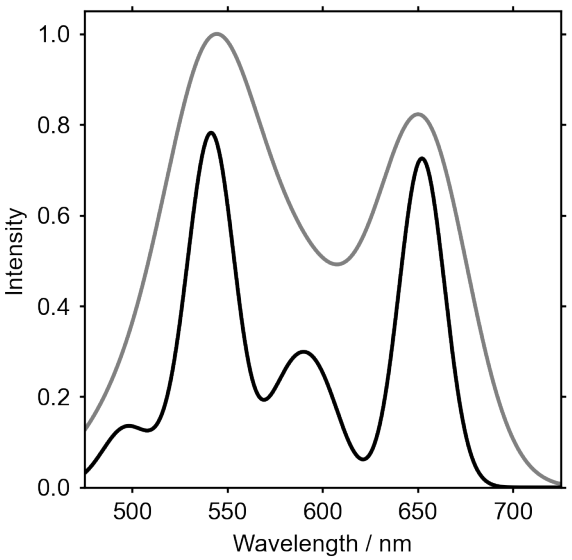


Figure 34. Fit from ICT Hamiltonian for linear absorption data at 53.5 min with the broadening as best fit of 24 nm (grey) and broadening decreased to 12 nm (black). Peak at 590 nm not observed in linear absorption spectrum due to overlap of peaks.

for all H-aggregates present in the film. Linear absorption cannot discern between species present in the film, but by modeling SSTA data with EADS and the ICT Hamiltonian, the distribution of packing geometries can be determined.

3.2.6 Summary. In summary, the formation of H-aggregates in films of DBSQ(OH)$_2$:PMMA during thermal annealing was tracked using concurrent linear absorbance and single-shot transient absorption (SSTA) measurements. Excited-state dynamics were modeled using a sequential decay model with two species. Our EADS model revealed that unannealed films contain monomers that undergo energy transfer to weakly-coupled monomers. As annealing proceeds, our model shows that the species present begin to transition into slip-stacked H-aggregates. After annealing, both species in our model contain no monomers, but instead are composed entirely of slip-stacked H-aggregates, differing only in their average interplanar spacing.

Our EADS and ICT Hamiltonian model suggests that energy transfer occurs from slip-stacked H-aggregates with greater interplanar spacing to slip-stacked H-aggregates with smaller interplanar spacing. This is likely due to a slightly lower energy CT-HA state with stronger electronic coupling. These findings provide insight into the directionality and rate of energy flow within the distribution of molecular packing structures that form in a solution-cast thin film. The ICT Hamiltonian also reveals how the intermolecular charge transfer integral changes with packing providing a predictive tool for assessing charge transfer ability of other D-A-D or A-D-A molecules. Further exploration of the relationship between intermolecular charge transfer integral and charge mobility would provide valuable insight for optimizing OPVs. This model demonstrates strong potential for predicting both the species present and their excitonic behavior, making it a powerful tool for understanding aggregation-dependent optoelectronic properties. By integrating real-time spectroscopy with first-principles modeling, this approach enables the rational design of organic semiconductors with tunable electronic properties, exciton dynamics, and charge transport capabilities. These insights lay the groundwork for engineering materials that optimize both energy and charge transport, advancing the field of organic electronics and excitonic materials.

CHAPTER IV

FILM DEPOSITION

4.1 Copper Phthalocyanine

Includes material from:

Walbrun, Z. S.; Paulson, A. Y.; Bodle, W. L.; Frainey, N. F.; Wong, C. Y. Novel Intermediate Phase During Film Deposition of Copper Phthalocyanine Revealed with In Situ Spectroscopies. **2025**, In progress.

Organic semiconducting materials are a promising candidate for solar energy due to their lightweight nature, flexibility, and relative stability at high temperatures.[158–160] Organic photovoltaics (OPVs) offer manufacturing benefits with cheap production cost[161] and roll-to-roll processing.[162] The active layer of an OPV is composed of an electron donor and an electron acceptor, which lie between two electrodes. When a photon is absorbed by the active layer, an electron-hole pair (exciton) is generated. This exciton can diffuse throughout the active layer, potentially reaching a donor-acceptor interface. A charge transfer (CT) state is formed when the hole resides in the donor material proximal to the excited electron in the acceptor material. The generation of CT states can be optimized by increasing the interfacial area between the donor and acceptor materials.[163] However, to improve photocurrent and reduce exciton trapping, the domains formed within the donor and acceptor materials must be of considerable size and crystallinity. Optimizing the morphology of the active layer can lead to higher power conversion efficiency of OPVs.[164,165]

Phthalocyanines (Pcs) hold promise as electron donor molecules in OPVs owing to their strong absorption of the solar spectrum[166] and their thermal and photostability.[167] When deposited into a thin film, the morphology of Pcs is

dependent on its substituents[168] and the deposition conditions.[169,170] Ghani et al. used atomic force microscopy (AFM) to show that copper phthalocyanine (CuPc) molecules aggregate to form pyramidal nanoribbons when deposited into a thin film.[171,172] Deposition of an electron acceptor on top of this pyramidal CuPc structure may increase the donor-acceptor interfacial area while minimizing islands of molecules where charges could be trapped, ideal for increased charge transfer in OPVs. Ghani et al. found that thin films cast from low concentration solutions form a monolayer of CuPc nanoribbons lying on the substrate[171] comprised of slip-stacked molecules.[169,173] The parallel transition dipole moments in adjacent slip-stacked molecules within a column results in positive electronic coupling and so-called H-aggregation. When cast from solutions with increased concentration, the resulting thin films comprise wider and taller nanoribbons, with the nucleation of new columns of molecules first occurring on the sides of the original nanoribbons, then also occurring on top of the first monolayer (**Figure 1b**). These thicker nanoribbons are found to have a herringbone packing structure, with the slip-stacking angle alternating from one column of H-aggregated molecules to the next.

These non-parallel transition dipole moments between molecules causes Davydov splitting that is observed as two peaks in linear absorbance spectra where the blue- (red-) shifted peak is H- (J-) like in character.[115] The Davydov splitting energy and the oscillator strength of the resulting H-like and J-like states is dependent on the orientation and distance between monomers in an aggregate.[174] If the blue-shifted (red-shifted) feature has greater oscillator strength, the aggregate has greater H-like (J-like) character.[42] Tight packing of the herringbone aggregates leads to the formation of a nearly isoenergetic CT state that can couple with the two Davydov states to yield four mixed Davydov-CT states.[175] For

phthalocyanines, the $\pi - \pi^*$ transitions to these four states are referred to as the Q-band.[176]

The electronic structure[177–179] and excited state dynamics[180,181] of CuPc in the solution and film phases have been characterized. Here, we use single-shot transient absorption (SSTA) and in situ linear absorbance to provide insight into the evolution of the electronic properties during film deposition, revealing a novel intermediate stage that has not previously been reported. Inspired by our new understanding of the mechanism of molecular aggregation, we demonstrate how the molecular ordering along the length and width of the nanoribbons can be tuned and how this affects exciton diffusion. The strategy presented here may lead to the development of crystallization strategies that can improve crystallinity and OPV efficiency in other molecules.

4.1.1 Experimental Details. CuPc (Eastman) and trifluoroacetic acid (TFA, 99% purity, Alfa Aesar) were used without further purification. Solutions of 0.5 mg/mL CuPc in TFA were prepared by heating at 60°C and stirring at 800 RPM for 8 hours. Supersaturated CuPc solutions were made by blowing nitrogen onto the CuPc solution, while heating at 60°C, until the peak in its linear absorbance spectrum blue shifted to 608 nm (**Figure 39a**), this left approximately 10% of the TFA and resulted in an ∼5.8 mg/mL CuPc concentration. Glass substrates (75 mm × 25 mm × 1 mm) were cleaned with methanol and held at 40°C and 60°C prior to dropcasting regular and supersaturated CuPc solutions, respectively. These temperatures were used in both cases to have the film deposition take ∼3 minutes. In situ SSTA and linear absorbance were measured during the formation of films from 0.5 mg/mL solutions,

on a homebuilt electric heating stage with a slit in the center allowing light to pass through.

A description of the SSTA setup can be found in **Chapter 2.1**. Pump and probe pulse energies at the sample were 1.83 μJ and 10 nJ, respectively. Traditional TA measurements were collected for the regular films and films cast from supersaturated solutions using a scanning translation stage (Newport), with time resolution of ∼80 fs, and time delay range of ∼60 ps. Film surfaces were measured with a Bruker Dimension FastScan AFM using Bruker TESPA-V2 non-rotated tapping mode probes, with a scan size of 5.0 μm, scan rate of 1.01 Hz, and 496 samples per line.

4.1.2 Results. The linear absorbance spectra measured in situ during film deposition at 40°C (**Figure 35b**) indicate that the film formation process can be divided into three stages: solution (R1), intermediate (R2), and film (R3). R1 persists for the first ∼70 seconds of the deposition and is characterized by four peaks in the Q-band which arise from protonation of the nitrogen atoms on the Pc macrocycle.[178,182] R2 lasts for 20 seconds and only shows one peak at 608 nm. The spectrum during R3 is typical for Pc films and persists indefinitely, and thus is assigned to the final thin film. There are two main features at 623 nm and 702 nm ascribed to Davydov splitting,[175,181] with two shoulders at 576 nm and 760 nm arising owing to Frenkel-CT mixing.[175]

The single feature observed during R2 has yet to be reported in the literature for CuPc, to the best of our knowledge. We assign this feature to the initial formation of H-aggregates, as the absorption peak is blue-shifted relative to the monomer spectrum. A single absorbance feature at was previously observed for a derivative of ZnPc in a high hydrogen bonding solvent,[183] a substituted AlPc

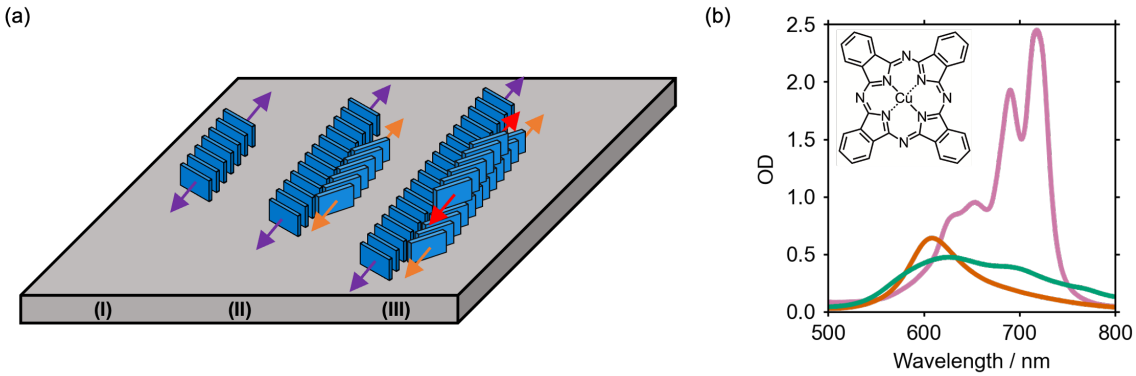


Figure 35. (a) Cartoon depiction of CuPc (blue rectangles) nanoribbon growth. Arrows represent face-on growth with different interactions with the edges of the CuPc molecules. Purple – glass interaction, orange – glass and side-side interaction, red – side-side interaction. (b) In situ linear absorption during the solution (pink), intermediate (orange), and film (green) stages. Chemical structure of CuPc inset.

in a phosphate buffer system,[184] and in substituted metal-free phthalocyanines in a mixed DMSO:H_2O system.[168] In each case, this single blue-shifted peak was ascribed to H-aggregates. This assignment is plausible in our system, as the nitrogen atoms of CuPc are protonated by the TFA solvent,[178,182] enabling hydrogen bonding and face-to-face aggregation in solution between Pcs.

SSTA (**Figure 36**) was also measured in situ, simultaneously with linear absorbance, during a ~3 minute deposition. Throughout the film formation process, a blue-shift of the excited state absorption (ESA) signal at ~550 nm is observed within the first 500 fs. This rapid blue-shift is consistent with intersystem crossing (ISC) in CuPc,[180] mediated by metal-to-ligand charge transfer.[185] Thus, all of the TA signal discussed below, after 500 fs, arises from triplets.[186] No fluorescence is observed at any stage during film formation, supporting this assignment. The strong negative TA signal at 608 nm measured during R2 must arise from ground state bleach (GSB) when the triplet state is populated. The ratio of GSB:ESA intensity was determined using the intensities at the peak maxima

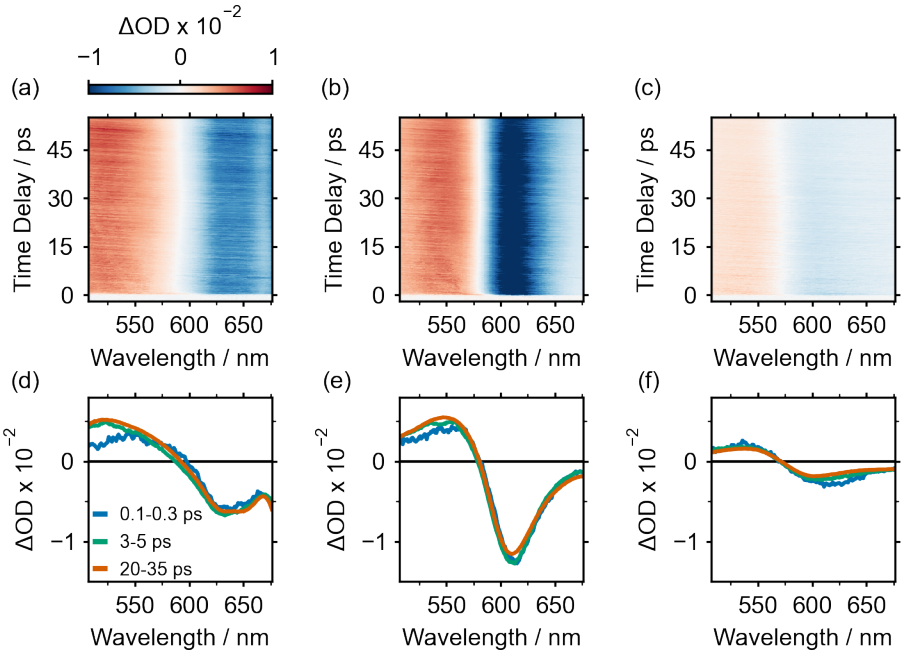


Figure 36. SSTA spectra from (a) 30 s, (b) 70 s, (c) 110 s during deposition binned over six pixels on the time delay axis. Spectral slices from (a), (b), and (c) shown in (d), (e), and (f), respectively.

for the 20-35 ps spectral slice. The relatively high intensity of GSB compared to ESA in R2 (2.1) compared to R3 (1.2) cannot be explained by the slightly larger optical density at 608 nm, the pump wavelength, during R2. Calculations using the pump spectrum and optical density (**Appendix A**) predict that the signal magnitude would only be 10.4% percent higher during R2 compared to R3 if the optical density were the only factor, but a difference of 144% is observed. Thus the origin of this strong GSB must be from triplets in CuPc H-aggregates.

Mass measured in situ simultaneously with linear absorbance revealed that solvent evaporation is significantly slower during R2 compared to R1 (**Figure 37**), which begins when ∼70% of solvent has evaporated. This suggests that solvation shells remain around the H-aggregate CuPc nanoribbons during R2, preventing the seeding of adjacent columns of H-aggregates, which would have been observed

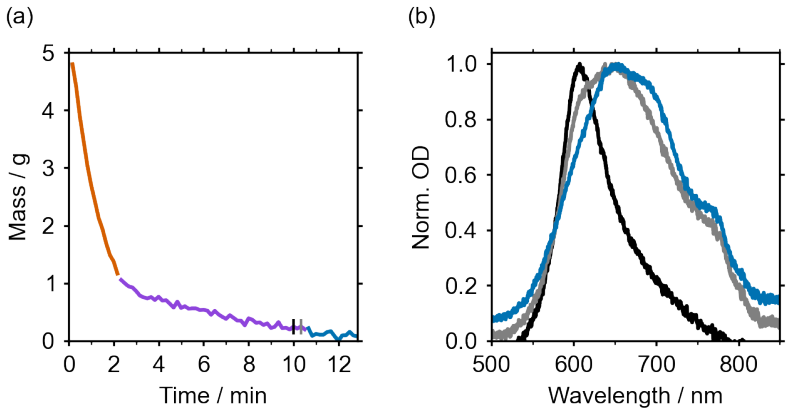


Figure 37. (a) In situ mass measurements during film deposition. A larger substrate and volume of solution was used, leading to a longer deposition time. Linear absorption spectra were taken concurrently to identify the stage as solution (orange), intermediate (purple), or film (blue). (b) Linear absorption spectra at times given by markers in (a) and for the film stage (blue).

as Davydov splitting in the absorbance spectra. When ~95% of the solvent has evaporated, or a concentration of ~9.5 mg/mL, Davydov splitting is observed in the absorbance spectra (**Figure 37b**).

In an effort to trap the intermediate and determine its morphology, supersaturated solutions of CuPc were prepared. The stark differences in film morphologies between regular films and films cast from supersaturated solutions are revealed by AFM images. A CuPc thin film deposited from a 0.5 mg/mL solution showed crinkly nanoribbons (**Figure 38a**), while a film deposited from a supersaturated CuPc solution had straighter nanoribbons that appear more ordered (**Figure 38b**).

Supersaturated solutions (C1) have a linear absorbance spectrum identical to R2, with a lack of Davydov splitting showing that the nanoribbons exist as single solvated strands. When the supersaturated solution is cast into a thin film (C2), the H-like peak in its absorbance spectrum appeared at the same wavelength as the single peak in C1 (**Figure 39a**). Comparing the spectra for C2 and R3, the

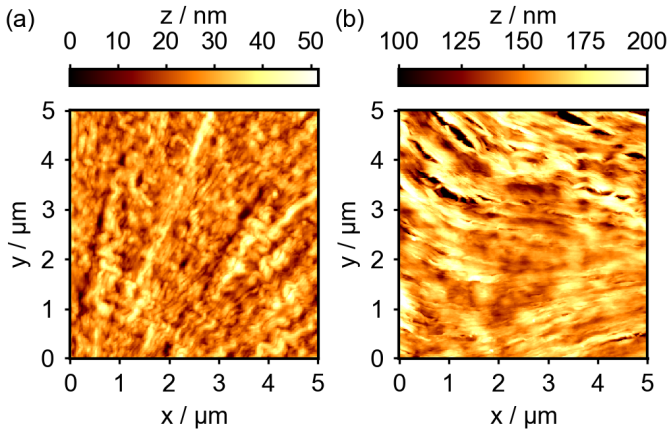


Figure 38. AFM images of CuPc films cast from (a) 0.5 mg/mL and (b) supersaturated solutions.

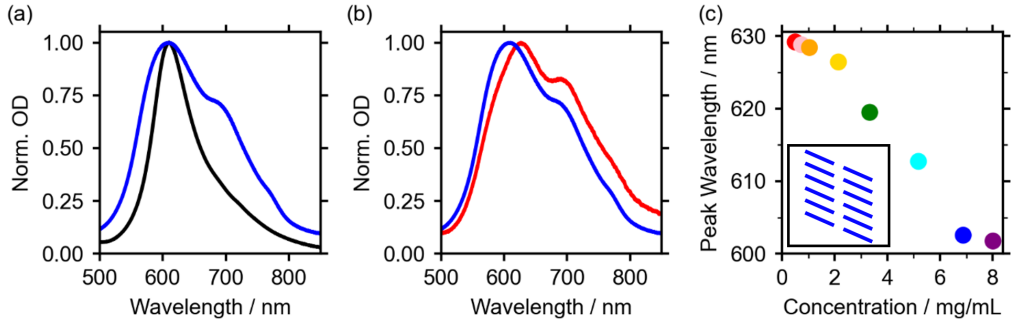


Figure 39. Linear absorbance spectra of (a) supersaturated solution (black) overlayed with the thin film cast from supersaturated solutions (blue) and (b) the regular thin film (red) and the thin film cast from supersaturated solutions (blue). (c) Relationship between the peak wavelength of the higher energy peak and the concentration of the CuPc solution prior to casting. Brickstone packing structure inset.

spectrum for C2 is blue-shifted and the higher energy feature has greater intensity (**Figure 39b**). This overall blue-shift and the increase in the lower energy peak intensity was previously observed for CuPc films containing a combination of herringbone and brickstone aggregates.[187] Brickstone aggregates have a smaller slip angle compared to herringbone aggregates and the slip-stacking angle does not alternate from one column of H-aggregated molecules to the next (**Figure 39c**), yielding the straighter nanoribbons observed in **Figure 38b**.

We hypothesize that H-aggregation occurs by a mechanism similar to the burst nucleation theories commonly used to explain nanocrystal growth: H-aggregate formation will occur when CuPc concentration exceeds the supersaturation threshold and reaches an even higher nucleation threshold. The initial formation of aggregates will lower the concentration below the nucleation threshold, But as the solution will still be supersaturated, molecules will continue to add to the existing H-aggregates through diffusion limited growth until the concentration of CuPc monomers in solution reaches the saturation threshold. In supersaturated solutions with less solvent, fewer monomers will be left in the solution when it reaches the saturation threshold. These concentrations appear to be below the nucleation threshold for seeding an adjacent column of molecules in a herringbone structure, as evidenced by the lack of Davydov splitting in the absorbance spectra. It is likely that this nucleation threshold is much higher when the H-aggregate is solvated as opposed to lying on a substrate. Instead, the solvated H-aggregate strands can further aggregate to form thicker nanoribbons until the solution is dropcast and solvent rapidly leaves the system. Meanwhile, there are fewer CuPc monomers in the solution that can become kinetically trapped in a disordered orientation. In comparison, when dropcasting a solution with a

lower concentration, the saturation threshold-limited H-aggregation stage leaves more CuPc monomers in solution and may not have time to complete before the rapid loss of solvent during casting causes the nucleation of adjacent columns of molecules in a herringbone configuration. There are many more CuPc monomers that can cause this seeding, or that can become kinetically trapped. Notably, when films are cast from supersaturated solutions of H-aggregates, without many monomers remaining to seed a herringbone structure, individual H-aggregate columns may be equally likely to further aggregate into a brickstone pattern as into a herringbone pattern. Brickstone and herringbone structure may co-exist within individual nanoribbons when there are less monomers available for side-on nucleation. The deposition of supersaturated solution into a film is able to separate the aggregation steps that elongate and widen the nanoribbons. Thus, the amount of solvent (and thus CuPc monomer) remaining in the solution prior to casting tunes the lengthwise and widthwise molecular order.

The TA spectra for supersaturated films (**Figure 40**) were globally fit to one exponential and a long-lived offset (**Equation 4.1**), assuming that the model only involves triplet excitons.

$$\Delta OD(t, \lambda) = A(\lambda)e^{-t/\tau} + B(\lambda) \tag{4.1}$$

As intersystem crossing occurs in <500 fs for CuPc and the triplet quantum yield is near 100%,[180] this is a reasonable assumption. The global fits reveal a time constant for regular CuPc films of 17.9±0.3 ps (**Figure 41**) that are similar to reports from Del Pino Rosendo et al.[181] Previous reports have attributed this time constant to exciton-exciton annihilation.[181,188] For the films cast from supersaturated solutions, the shorter time constant is 11.7±0.3 ps, compared to 17.9±0.3 ps for regular films. Since films cast from supersaturated solutions have

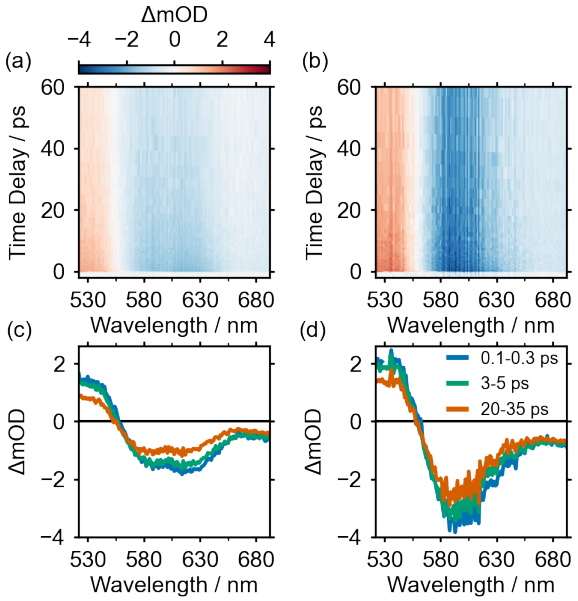


Figure 40. TA spectra of (a) normal CuPc films and (b) supersaturated CuPc films. (c) and (d) show spectral slices from (a) and (b), respectively.

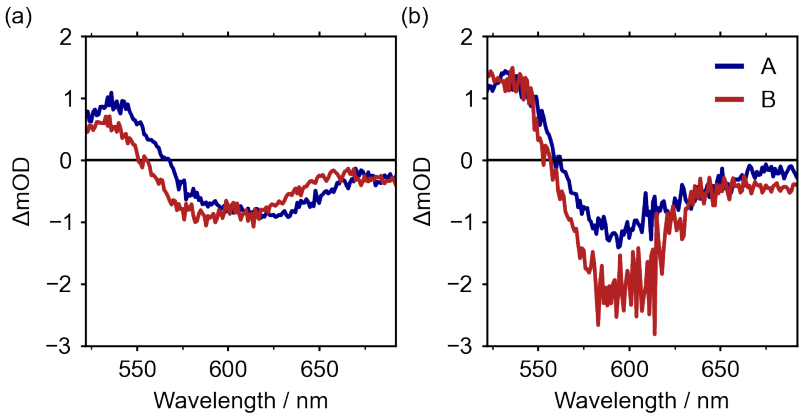


Figure 41. Global fit amplitudes for films cast from a (a) 0.5 mg/mL and (b) supersaturated solution.

greater crystallinity lengthwise along the nanoribbons, excitons are able to diffuse faster and further along the nanoribbons, leading to more rapid exciton-exciton annihilation.

4.1.3 Summary. In situ linear absorption measurements revealed a novel intermediate stage during CuPc film deposition with solvated H-aggregates. SSTA spectra from the intermediate stage exhibited a much larger GSB signal at 608 nm compared to thin films with thicker nanoribbons and Davydov splitting. Supersaturated solutions of CuPc in TFA were found to have similar absorption spectra to the intermediate stage during regular film depositions. The mechanism of CuPc aggregation using a solution of supersaturated CuPc can be separated out into H-aggregation, which happens during the solution preparation, and J-aggregation, which happens as the final solvent is evaporating. By separating the stages of aggregation, the film morphology can be carefully controlled and optimized for OPVs.

TA measurements revealed that exciton-exciton annihilation is faster in films cast from supersaturated solutions owing to more rapid exciton diffusion. AFM images showed that the CuPc nanoribbons appear to be straighter in films cast from supersaturated solutions. Since films cast from supersaturated solutions form H-aggregates before the film deposition occurs, the nanoribbons have more H-like character. This study shows the basis for how in situ spectroscopies can be used to explore new aggregate structures and control exciton dynamics for use in OPVs.

CHAPTER V

PHYSICAL CHEMISTRY LABORATORY STUDY

Includes material from:

Walbrun, Z. S.; Nawab, L.; Wong, C. Y. Pre-Lab Simulation of Microscope Building in Upper Division Laboratory Improves Student Confidence. **2025**, In progress.

While most faculty agree that undergraduate laboratories play an important role in scientific education[189–191], evidence suggests that labs often do not provide the intended educational benefits[192–195], and student reaction to labs tends to be negative.[195–197] The purpose and methodology of this aspect of a scientific education should be rigorously questioned, particularly as the cost of running teaching labs is very high in terms of space, materials, and personnel.[191,197] This cost can be prohibitive, particularly for smaller institutions like community colleges and high schools, so this pedagogical issue is of particular relevance in an environment of constrained funding for secondary and post-secondary education.[198]

Pre-laboratory activities have been identified as being critical to improving student learning outcomes.[199,200] Common pre-laboratory activities include lectures, online videos, quizzes, discussions, and computer simulations. Reports by Isom et al. and Davidowitz et al. showed that having a pre-laboratory discussion improved student understanding of laboratory concepts and improved scores on lab reports.[201,202] Pogacnik et al. reported using a combination of lecture and a pre-laboratory exam before the in-person laboratory and found that final exam grades increased. However, more time was dedicated by teaching assistants in lecturing and grading, while only lower level Bloom's taxonomy were assessed on the pre-lab examination.[203] Typically when assessing student learning objectives, they are

categorized using Bloom's taxonomy, which categorizes assessments based on the desired outcome.[204] Lower level outcomes would be asking students to remember, understand, or apply, whereas higher level outcomes are analyze, create, and evaluate. Lower level Bloom's taxonomy questions are also more easily answered using generative artificial intelligence (GenAI)[205], suggesting that the pre-lab focus should be moved toward higher level questions to promote student learning and engagement. This can easily be done with a shift toward modeling and more open-ended tasks for pre-lab activities.

Less research has been reported on the impact of pre-lab activities on students' affective experience. Affective experiences for undergraduates have been linked to sense of belonging and retention[206,207] and laboratory classes often have a negative response from students.[195–197] Barrie et al. found that student attitude in the laboratory is improved by clear assessment, motivation, and resources, such as pre-laboratory information.[208] The use of instructional videos before in-lab experiments were generally found to improve student attitudes and experience[209–211], but had no effect on grades.[210,212] In-lab experiments paired with interactive computer simulations have been shown to improve student understanding of laboratory concepts.[213–215] Students have responded positively to implementation of computer simulations[214,216] and report a preference for completing virtual work prior to in-lab experiments.[217] These findings indicate the value in using computer simulations as a pre-laboratory activity. All these reported studies have been with either high school or lower-division undergraduate laboratories. Upper-division laboratory courses, which generally cover more complex topics and have lower student enrollments, have not been studied extensively.

In this study, we aimed to measure the impact of computer simulations as a pre-laboratory activity for an upper-division chemistry laboratory. To our knowledge, this is the first report involving simulations of instrument assembly and operation for an upper-division chemistry laboratory. For this study we asked two primary questions: (1) How does engagement with a computer simulation of in-laboratory activities impact the expectations and experiences of students during the in-lab activity? (2) Does engagement with a computer simulation prior to performing in-laboratory activities improve student competence in the laboratory and understanding of the scientific concepts presented in the lab? Addressing these questions can also aid in designing pre-laboratory simulations that support higher level student learning without student use of GenAI.

5.1 Experimental

This research study was conducted in the second term of physical chemistry laboratory at a large public university in the Pacific Northwest over the course of three years. Year 1 (N=14) consisted of the control group that were not given access to the computer simulation. Students in year 2 (N=19) and year 3 (N=27) interacted with the computer simulation 1-2 weeks before the in-lab activities. Students in all years were given a 50-minute lecture on brightfield microscopy during the first week of the term. In addition to the lecture, students in the first year that did not have the simulation had a two-hour tutorial with a worksheet (**Appendix B.1**). In the second and third years, this two-hour tutorial was replaced with the simulation. The in-lab activities involved constructing a brightfield microscope using a procedure detailed in the lab manual (**Appendix B.2**). The building of the instrument was divided into seven sections. After completing the tasks in each section, students were asked to record their completion

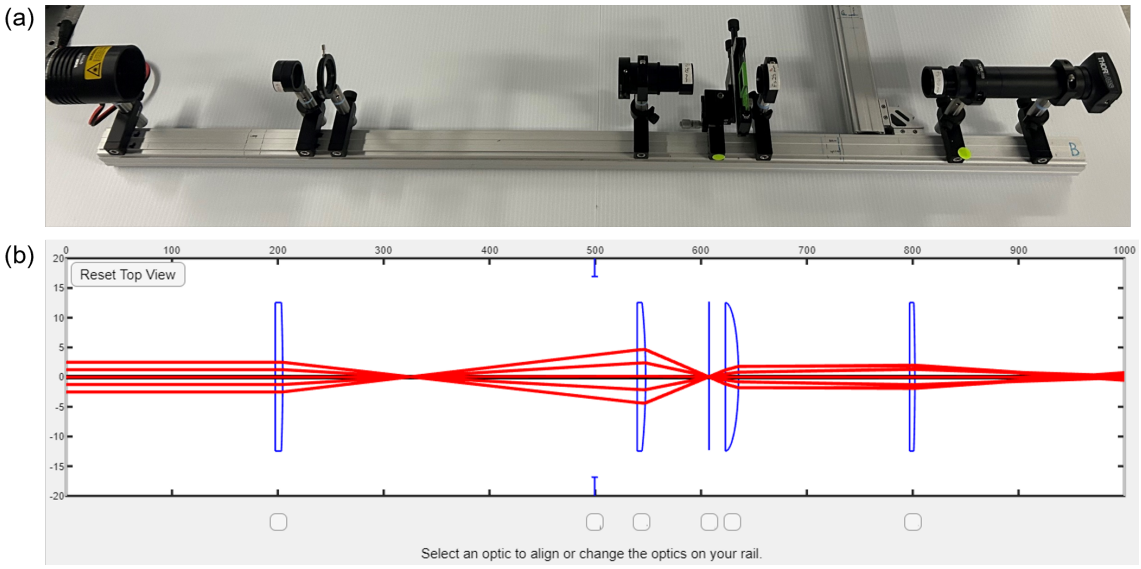


Figure 42. (a) Microscope from in-lab activity. (b) Image from microscopy simulation showing rays of light (red lines) after passing through lenses (blue). Sample plane shown as a blue line.

time and answer a few conceptual questions on the worksheet. Sections c, d, e, and g, involved tasks that were included in the computer simulation. Those sections focused on constructing a 4f imaging system, collecting light from the lamp, setting up Köhler illumination, and wavelength dependence of focal point and resolution, respectively. In addition to the total time taken to complete the worksheet, the completion times for these specific sections were analyzed. The total time taken to complete the laboratory refers to the hands-on activities and worksheet for sections c-i.

During the simulation, students completed activities that included creating and mounting optics to the simulated rail, and properly aligned optics by moving them on the simulated rail in each of the steps. Students compared different focal lengths of lenses, compared the effect of lenses on different wavelengths of light, built a 4f imaging system, switched between visualizations of the light rays

emerging from a collimated source and a point source, and built the microscope that they would later construct in the lab (**Figure 42**). Students who completed the computer simulation were given a worksheet with instructions and questions about the simulation (**Appendix B.3**). The procedure, in-lab worksheet, and teaching assistant (TA) for the laboratory were not changed over the course of the three years of the research study. The same TA was responsible for grading the in-lab worksheet for all three years.

Students were given surveys that implemented the Meaningful Learning in the Laboratory Instrument (MLLI)[208] before and after in the in-lab activities (**Appendix B.4**) that contained 31 questions that were categorized as cognitive, affective, or cognitive/affective. Seven additional questions were given after the in-lab activities for students who completed the simulation. Students completed the survey at the beginning and end of the laboratory session and were asked to rate each statement on a scale of 1-10 (1 = disagree, 10 = agree). IRB approval (STUDY00000265) was obtained from the office of Research Compliance Services at the university.

5.2 Results

The in-lab worksheet grade and overall time spent were analyzed from the groups with and without the simulation before the in-lab activities. No significant difference was found in the average or distribution of worksheet grades (**Figure 43a**). For the overall time spent, a slight decrease in the distribution of overall time spent was observed for the group with the simulation, but not significant (**Figure 43b**).

Although the overall time spent on the laboratory was nearly the same for the groups with no simulation versus with simulation, the start and end times

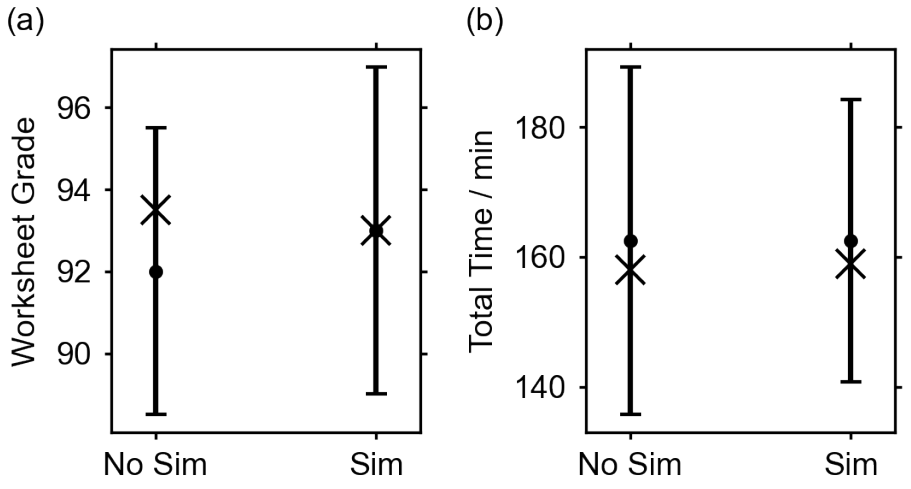


Figure 43. (a) Worksheet grade and (b) total time on in-lab activities for no simulation and simulation groups. Mean and median indicated with circle and x, respectively. Error bars represent one standard deviation from the mean.

of each section of the in-lab activity were analyzed. The only sections of the in-lab activity that have significantly different completion times between groups were sections c and e (**Figure 44**). Section c involved constructing a $4f$ imaging system. As this is the first time that the students are working with the optics and camera software, it is more difficult to attribute any changes to the computer simulation. Both groups of students did not have any hands-on experience with optics, however the group without the simulation saw the optics and talked about the theory before performing the in-lab activity. In part e, students have been working with the optics for ∼45 minutes at this point. Section e involved setting up Köhler illumination, which is the main focus of the computer simulation. For the group that had the computer simulation, the average time to complete the section decreased and the standard deviation significantly decreased. The computer simulation may have helped students who had minimal previous experience with

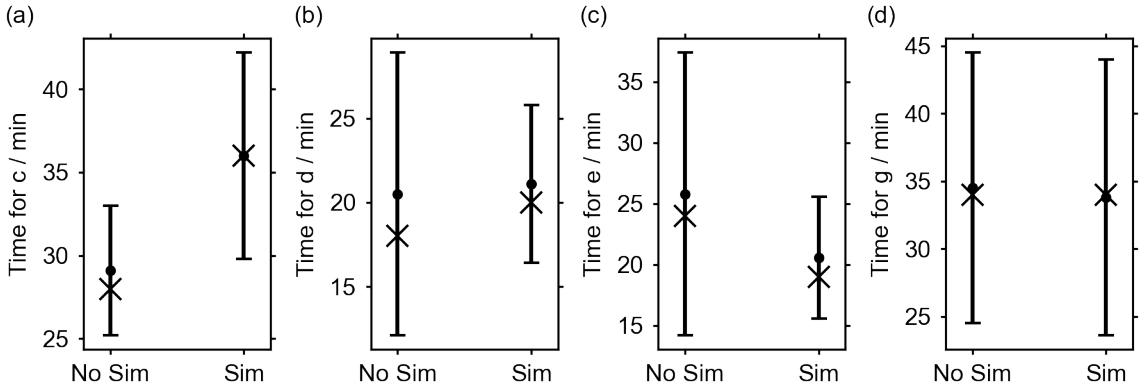


Figure 44. Time spent on sections c (4f imaging system), d (collecting light from the lamp), e (setting up Köhler illumination), and g (wavelength dependence of focal point and resolution) for no simulation versus simulation. Mean and median indicated with circle and x, respectively. Error bars represent one standard deviation from the mean.

optics understand how light interacts with these optics, making this section of the laboratory easier to complete.

Survey results from both groups before and after the in-lab activities were analyzed with the question categories as cognitive, affective, or both. Cognitive questions are related to how students think about their laboratory experiences and affective questions are how students feel about their laboratory experiences.[208] Comparisons were made using the survey results after the in-lab activities, comparing the groups with and without the simulation. Ratings from questions 2, 9, and 18 from the post-lab MLLI survey for the two groups are shown in **Figure 45**. Overall, students from the simulation group appear to be less worried about finishing on time, less nervous to make mistakes, and less nervous when handling equipment.

Ratings from the additional questions A-G (Table 1) from the simulation group are shown in **Figure 46**. Most student ratings were quite positive for all questions given. Question C corresponds to the simulation building confidence

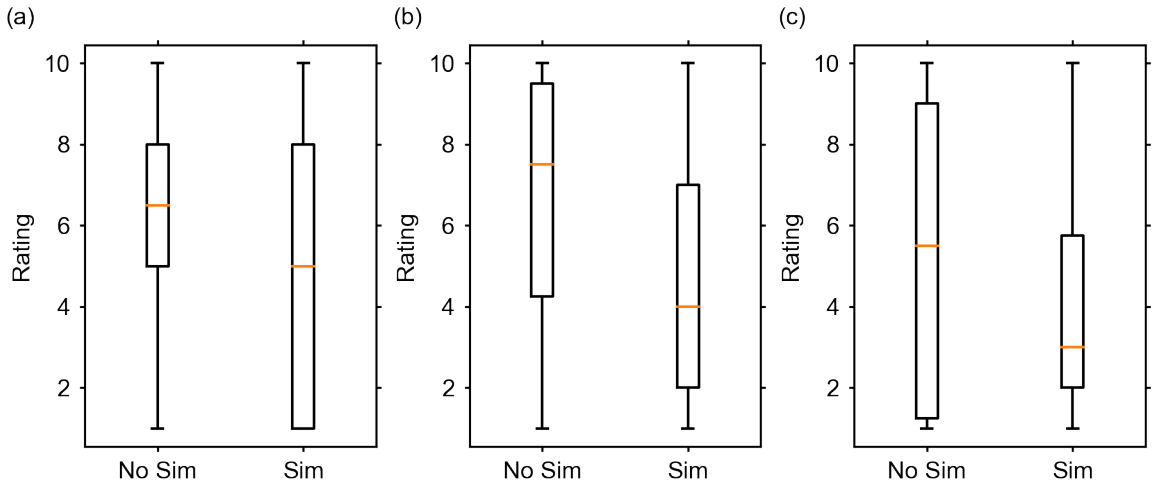


Figure 45. Box and whisker plots for (a) MLLI Q2 (to worry about finishing on time), (b) MLLI Q9 (to be nervous about making mistakes), and (c) MLLI Q18 (to get nervous when handling equipment) after the in-lab activity for the no simulation versus simulation group. Ratings are given as 1 = disagree and 10 = agree.

Letter	Question
A	The simulation helped me understand the concepts in this laboratory.
B	This simulation helped me feel more comfortable working with optics.
C	This simulation increased my confidence for the in-lab activity.
D	This simulation helped me visualize what is occurring while building a microscope.
E	This simulation made me more excited about performing the in-lab activity.
F	The simulation made the in-lab activity go more smoothly.
G	The simulation was a good use of my time.

Table 2. Additional questions given to simulation group after in-lab activity.

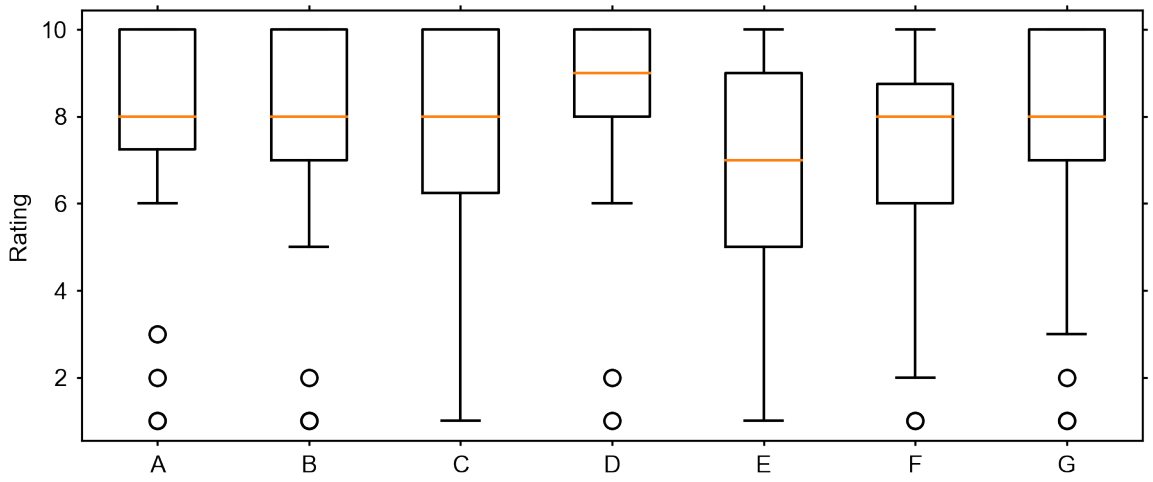


Figure 46. Box and whisker plots of additional survey questions A-G given after the in-lab activity for the simulation group. Outliers lie 1.5 times the interquartile range away from the edges of the box and are represented by circles.

in the laboratory, to which students mostly agreed. This agrees with the results presented in **Figure 45**, related to students worrying less about the laboratory activity. Question D had the smallest and highest distribution of ratings, which was related to visualization of what is occurring when the microscope is being built. As the simulation shows students what is happening to rays of light when lenses are added, this is quite beneficial for the in-lab activity, where they cannot see the rays of light.

5.3 Summary

This three-year research study in an upper division physical chemistry laboratory used a computer simulation that involved constructing a brightfield microscope. Compared to the control group with no simulation, the group that had the simulation did not see improved worksheet grades or faster overall completion time of laboratory activities. However, students who were in the simulation group reported feeling less nervous about building the microscope in-lab and were also less worried about finishing on time. The simulation group also had a smaller

distribution of completion times for the most significant section of the laboratory related to the simulation and students self-reported that the simulation helped them visualize what is happening when building a microscope. This study provides the basis for how a computer simulation involving instrument building impacts student learning and feeling in an upper-division laboratory course.

APPENDIX A

PUMP POWER CALCULATION

To verify that the high GSB signal was not due to the pump, the expected absorbed power was calculated at each phase of the deposition process. If the absorbed power was drastically different for the intermediate phase when compared to the other two phases, the high TA signal could be explained by the absorption spectrum and pump alone.

By integrating under the input pump spectrum and equating that to the overall pump power (1.83 μJ), the pump power as a function of wavelength was determined. Using the pump power as a function of wavelength, we were able to see how much of the pump power was absorbed at specific wavelengths. The transmitted power was subtracted from the input power at a specific wavelength to determine the power absorbed:

$$P_A = P_i - P_T \tag{A.1}$$

Where P_A is the power absorbed at a specific wavelength, P_i is the input pump power at a specific wavelength, and P_T is the transmitted power at a specific wavelength. The transmitted and input pump power are also related to the absorbance (A):

$$P_T = \frac{P_i}{10^A} \tag{A.2}$$

Substituting the transmitted power into **Equation A.1**:

$$P_A = P_i - \frac{P_i}{10^A} \tag{A.3}$$

The absorbance at each wavelength from the linear absorption spectrum for each phase of the CuPc deposition process was used to determine how much power was absorbed at each wavelength. By integrating under the curve, the total power

absorbed for each stage was determined to be 0.245 μJ, 0.262 μJ, and 0.236 μJ for R1, R2, and R3, respectively. The difference in SSTA signal between the intermediate and film stage that was predicted by the pump power code was 10.4%, whereas the difference in the SSTA signal was actually 144%. Therefore, the unusually high TA signal cannot be explained by the optical density and the pump.

APPENDIX B

SUPPLEMENTAL INFORMATION FOR MICROSCOPY STUDY

B.1 Year 1 Tutorial Worksheet

1. Label the following optics (camera, tube lens, lens tube, achromatic objective, non-achromatic objective, collector lens, condenser lens, collar, post, iris, lamp, color filter):



2. Circle which part of c) and d) is the lens. Box which part of c) and d) is the iris.

3. What does it mean for the camera to be infinity focused?

4. Why do we want to use an achromatic lens?

5. Why do we want to use color filters?

6. What is Köhler illumination? Why is it important?

7. Draw the part of the setup that is a "4f" microscope. Label each optic.

8. What is the equation for magnification? What is the magnification for the system in this lab? How would you increase it?

9. Collect spectra of the lamp and with the absorptive filters using OceanView. Save the files and send them to yourself.

B.2 In-Lab Procedure

Today you will identify all your parts, set their heights, roughly assemble the microscope, and then carefully align it for the best possible image.

(a) Camera and tube lens assembly

1. Your TA will show you the sensor of a camera and attach a lens tube (a hollow black tube that acts as a spacer) and a tube lens (a lens at the end of the lens tube). The length of the tube has been chosen so the tube lens is one focal length (150 mm) away from the camera's sensor.

2. Identify the identical assembly at your microscopy station. Label the sample camera and tube lens.

(b) Identify all the parts

Use gloves whenever handling optics. Use the photos below to identify the following items. They may be in your optics rack, optics box, parts box, or already on the table.

1. Main rail and side rail

2. Rail carriers

3. Collars

4. Posts

5. Irises (lever and ring controlled)

6. Lamp

7. Empty lens mount

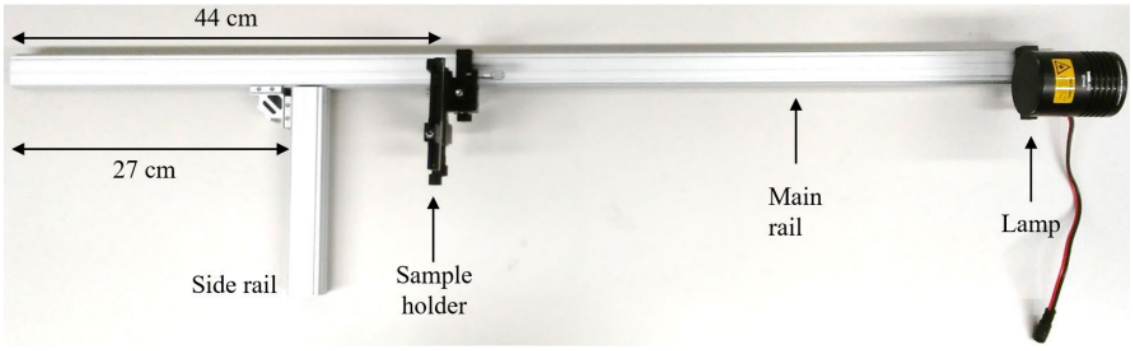


Figure B.1. Rail that ensures horizontal alignment of your optics, with lamp and sample holder.

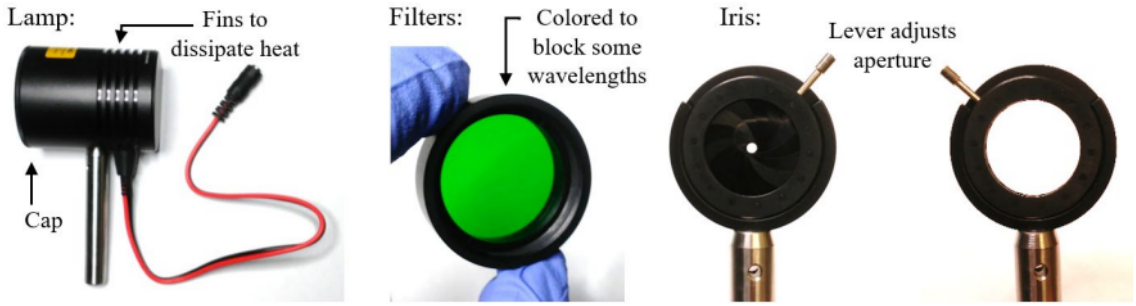


Figure B.2. Optical elements you will use in this lab.

8. Plano-convex lens (f=75 mm)

9. Plano-convex lens (f=25 mm)

10. Achromatic lens (f=25 mm) and iris

11. Plano-convex lens (f=50 mm) and iris

12. Sample mount on translation stage

13. Sample camera with lens (f=150 mm)

14. Filters (red, orange, green, and blue absorptive, green interference)

(c) Construct a basic $4f$ imaging system

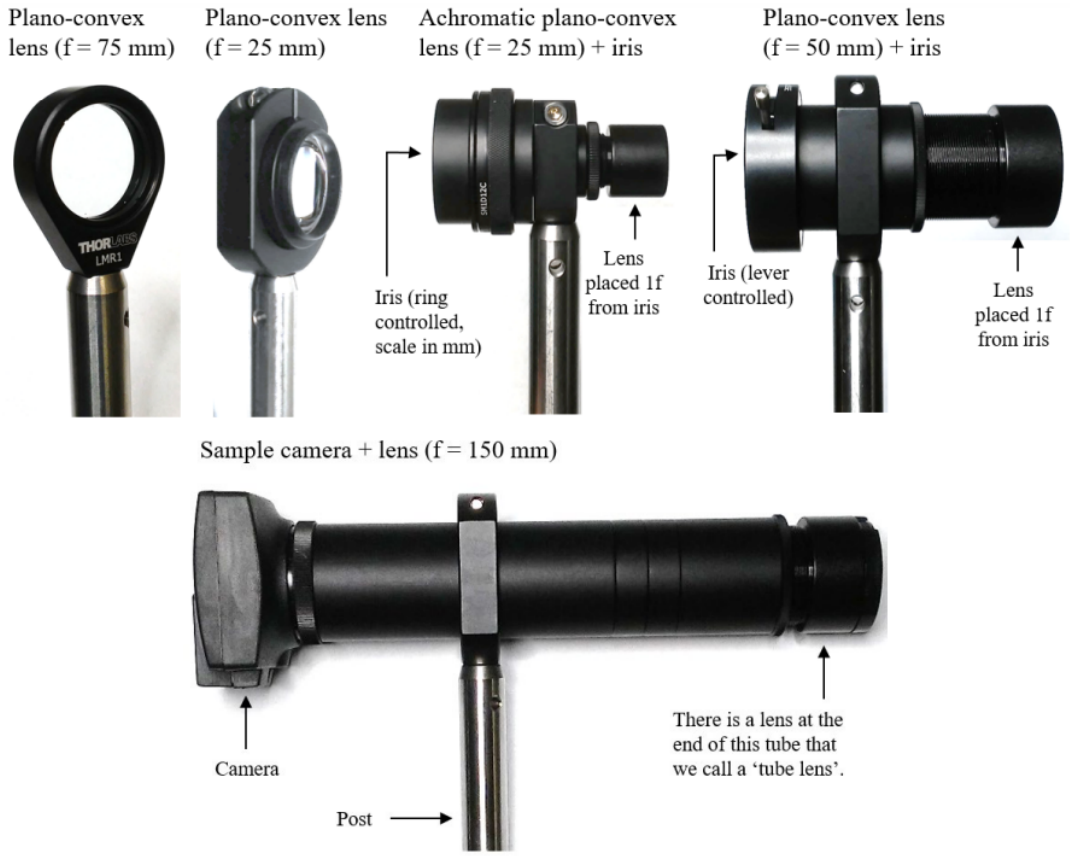


Figure B.3. Optical elements that include lenses that you will use in this lab.

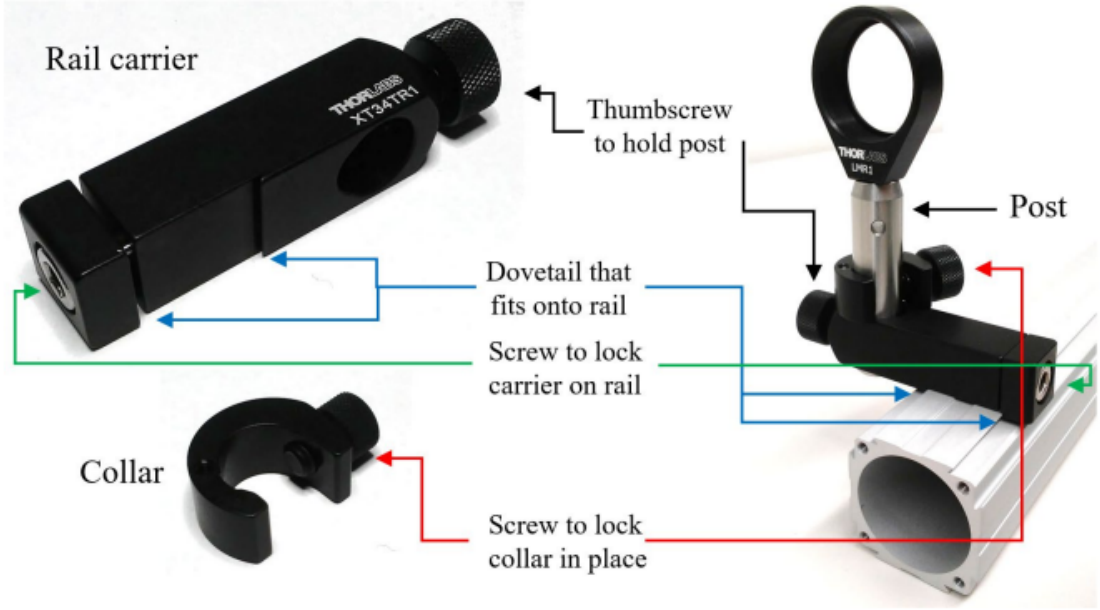


Figure B.4. Parts needed to install an optic on the rail.

Wear gloves while handling optics. Some of the posts will have a collar pre-installed on them. This sets the height of the optic when it is installed on the rail. Please do not move the collars. Label rail carriers with the name of each optic you install.

1. On your worksheet, note who is using the computer, who is working on the microscope, and your start time.

2. A test target is in your sample holder and a lamp is already installed ∼15 cm from the end of the rail. Plug in the lamp and make sure the lamp shines down the rail towards your sample.

3. Use two separate rail carriers to install the sample camera on the opposite end of the rail from the lamp. The 'Thorlabs' label on the camera should point up.

4. Install the f=25 mm plano-convex lens between the sample stage and the sample camera. It should be one focal length away from the sample stage. This is the **objective** lens - label it! It collects light after it has passed through the sample.

5. Move the camera on the rail so that the distance between the tube lens and objective lens is the sum of their two focal lengths. You have created a $4f$ imaging system. Make sure you can identify the four focal lengths in your imaging system.

6. Plug in the camera. Open the Thorcam software.

7. Start the camera by pressing the video button. Click the settings button to adjust the settings. Adjust exposure time such that the image is not

overexposed, but clearly visible. Wave your hand in front of the camera to make sure it is actually responding.

8. Move the objective lens on the rail until the image is close to being in focus.

9. Use the silver micrometer on the sample stage to fine tune the focusing.

10. Use the two black knobs on the sample stage to move the target so you are imaging the smallest lines you can resolve.

11. The scrolling wheel on your mouse can zoom in and out of the image. Zoom in on element 1 in group 4. Use the ruler tool (show icon) in Thorcam to measure the horizontal width of a horizontal line in this element. Each pixel of this camera is 5.2 μm wide.

12. Save your image and fill in your worksheet.

(d) Collect light from the lamp

Since we are not currently focusing the light from the lamp, most of its light does not hit the sample, so the camera's exposure time needs to be high. To fix this, we use a lens to collect the light after the lamp and direct it towards the sample. It will be easier to do this if we first install an absorptive, colored filter.

1. On your worksheet, note who is using the computer, who is working on the microscope, and your start time.

2. Install either the red or blue colored filter between the lamp and your sample.

3. Adjust your exposure time to get an optimal image. Note this on your worksheet.

4. The 125 mm lens is your **collector** lens. It collects light from the bulb and sends it towards the sample. Install the 125 mm lens somewhere between the lamp and your sample so it can collect a lot of light, and label it.

5. Gently press a piece of paper up against the sample so you can see the spot of light hitting it. Slide the collector lens along the rail until you can see the filament imaged onto your paper.

6. Optimize your exposure time. If your image is still over-exposed, even at the lowest possible exposure time, talk to your TA about installing a neutral density filter. This filter blocks all wavelengths of light equally.

7. While watching the image from the sample camera, optimize the position of the collector lens by moving it slightly along the rail until the filaments are in focus in your image.

8. Save your image and fill in your worksheet.

(e) Set up Köhler illumination

After Part d, both the sample and lamp filament (bulb) are imaged on the camera. We do not want the lamp filament to be imaged on the camera, so we will make sure the filament is perfectly out of focus at the sample by adding a condenser lens before the sample and focusing the filament one focal length before that condenser lens.

1. On your worksheet, note who is using the computer, who is working on the microscope, and your start time.

2. Install the 50 mm lens between the sample and collector lens, so that the lens is one focal lens away from the sample. This is the **condenser** lens - label it! It condenses (focuses) light onto the sample.

3. If we image the filament one focal length before the condenser lens, the filament will be perfectly out of focus one focal length after the condenser lens, at the sample. Before you installed the condenser lens, the filament was focused at the sample. How should you move the lamp and the collector lens so the filament is imaged one focal length before the condenser lens? Hold a piece of paper one focal length before the condenser lens and move the collector and lamp to test your theory. When you are successful, you should be able to see the coils of the filament on the paper.

4. Remove the piece of paper and optimize your exposure time.

5. Save your image and fill in your worksheet.

(f) Field stop prevents excess light from hitting sample

Light from the lamp may scatter off parts of the sample that aren't being imaged, and this might cause extra light to hit the detector and decrease your contrast. Extra light can also damage the living or fluorescent samples. A "field stop" is an iris found in most microscopes to block extra light from hitting the sample.

1. On your worksheet, note who is using the computer, who is working on the microscope, and your start time.

2. Place an iris ∼2 cm past your collector lens. This is your **field stop** - label it. This optic does not have a collar on it, as you will be adjusting its height.

3. Close the iris until you see the edges of the iris in your image, or your image starts to get dimmer.

4. Slide your condenser lens on the rail until the edges of your field stop are in focus.

5. Adjust the height of your field stop so it is vertically centered in your image.

6. Close your field stop enough so that all the edges are visible.

7. Save an image and fill in your worksheet. Congratulations, you have built a brightfield microscope!

(g) Wavelength dependence of focal point and resolution

1. On your worksheet, note who is using the computer, who is working on the microscope, and your start time.

2. Remove any colored filters and lower your exposure time.

3. Install a neutral density (ND) filter with the lowest ND. This filter blocks all wavelengths equally. Optimize your exposure time. Let your TA know if your image is still over-exposed. Record which ND filter you used on your worksheet.

4. Use the micrometer to focus on the test target.

5. Determine the group and element of the vertical lines that you can resolve. Repeat for the horizontal lines. Fill in your worksheet.

6. Remove your neutral density filter. Repeat steps 4-5 after installing the blue absorptive filter and optimizing your exposure time.

7. Remove the blue absorptive filter. Repeat steps 4-5 after installing the red absorptive filter and optimizing your exposure time.

8. Remove your filter and reinstall your ND filter.

9. Fill in your worksheet.

(h) Wavelength dependence of focal point using an achromative objective

1. On your worksheet, note who is using the computer, who is working on the microscope, and your start time.

2. Your current objective lens is not an achromatic lens. Replace it with the achromatic objective lens. There is an iris connected to this lens, which you'll use in the next activity. For now, make sure you can identify the lens, and place it one focal length away from the sample. Loosen the rail carrier and slowly slide the lens on the rail to bring the sample into focus.

3. Optimize the position of the sample using the micrometer. Note its position on your worksheet, as well as the group and element of the vertical and horizontal lines you can resolve.

4. Remove the neutral density filter. Install the red filter. Repeat step 3 and fill in worksheet. No need to find the resolution for this image.

5. Remove the red filter. Install the blue filter. Repeat step 3 and fill in worksheet. No need to find the resolution for this image.

(i) Numerical aperture

The iris connected to the achromatic lens is exactly one focal length away from the lens, and is called the 'back focal plane iris'. It is activated by the knurled ring, and there is a mm scale printed on the iris. This iris is very delicate. It is important that you do not exceed the range of the printed scale. If the iris cannot seem to turn all the way to some part of the scale, ask a TA. Do not force the iris to turn.

1. On your worksheet, note who is using the computer, who is working on the microscope, and your start time.
2. Remove any other filter, then install a red absorptive filter.
3. Use the micrometer to bring the sample into focus.
4. Set the iris to 12 mm and optimize your exposure time.
5. Note the vertical and horizontal resolution on your worksheet.
6. Repeat steps 4 and 5 for iris diameters of 6 mm, 3 mm, and 2 mm.
7. Answer the questions in your worksheet.

B.3 Simulation Procedure

The simulation is publically available for download here:
https://blogs.uoregon.edu/wonglab/microscopy-labs-for-undergraduates/

A. Create a lens

1. Go to the 'Create Optics' tab.
2. Give your first lens a name, e.g. 'Lens radius 100'.
3. Give your first lens an input radius of 0 and an output radius of 100. Leave the other options the same.
4. Click on 'Add Optic'.

B. Mount and align your new lens

1. Go to the 'Mount Optics' tab and scroll down to the bottom of the 'Optics rack' list to select the lens you created (e.g. 'Lens radius 100').
2. Click 'Mount to Rail', then click the button with the '∧' in the middle of the screen to mount the lens.
3. Click the little box underneath the lens to select it.
4. Use the slider in the middle of the screen (between the two View windows) to shift the lens along the rail (black line). Use the sliders on the left side of each View window to move the lens side-to-side (in the Top View) and adjust the height (in the Side View). Adjust to get the rays to converge on the rail (black line). *No need to make it perfect.* Click on 'Done' when you are finished.

Lens name	Lens radius	Distance from lens to focal point
	100 nm	
	25 nm	

Table B.1. Lens radius and distance from lens to focal point.

5. Make observations. What is the distance between the lens and the focal point? Fill in **Table B.1**.

C. Compare lenses

1. Create another lens, with a new name and an output radius of 25.
2. Remove the first lens by clicking on its name in the 'Mount Optics' tab, then clicking 'Move to Rack'.
3. Find your newly created lens and mount to rail. Align the lens. No need to be perfect. Click 'Done' when you are finished.
4. Make observations. What is the distance between the lens and the focal point? Fill in **Table B.1**.
5. Remove the lens from your rail.
6. Make a new lens that will focus the collimated rays 100 mm after the lens. Mount it to the rail and align it to confirm that it works. Fill in **Table B.1**.

D. Compare a few wavelengths

1. Go to the 'Rays' tab. By default, you currently have collimated 600 nm rays. Change the wavelength to 300 nm and click on 'Create Rays'.
2. Make observations. What happened to the focal length of the lens? Fill in **Table B.2**.

Wavelength	Lens radius	Distance from lens to focal point
600 nm		
300 nm		

Table B.2. Focal length dependence on wavelength

3. Try two more wavelengths to confirm your observation and fill in your chart. The effect you see is because the index of refraction for glass is different for each wavelength and causes the focal lengths of the lenses to change slightly.

4. Go back to 600 nm.

E. Build a 4f imaging system

1. In the 'Rays' tab, change 'Rays Shown' to 'Point Source' and click 'Create Rays'.

2. Shift and align your lens with 100 mm focal length so that it collimates the light.

3. How far is the lens from the point source when it collimates the light?

   _____

4. Mount your lens with a radius of 25 to the rail. What is its focal length? _____ Two '∧' buttons will appear, allowing you to place it between the point source and the first lens, or after the first lens. Choose the '∧' on the right to place the lens past the first lens.

5. Align the lens and move it so that the distance between the two lenses is sum of their two focal lengths.

6. Make observations. Where do the rays meet back at a point? If you placed a 1 mm sized circular sample at 0 mm (the point source), where would the image of the circle form? How big would the image of the circle be?

F. Simulate building the microscope you'll build in lab

1. Unmount all lenses from the rail.
2. All of the optics for the microscope have already been created and are on your optics rack. First, mount the sample to the rail. Center it and place it at 600 mm.
3. In the 'Rays' tab, change 'Rays shown' to 'Collimated', and click 'Create Rays'.
4. Mount your objective after the sample. Select the lens and read its description in the 'Info on Optics' tab. Look at its radius - what do you think the focal length is? Align it and position it one focal length after the sample.
5. Build the $4f$ imaging system by mounting the tube lens past the objective. Read its description. Align it and position it so that the distance between the objective and tube lens is the sum of the two focal lengths. Fine tune the position so that the rays after the tube lens are collimated.
6. Condense the light onto the sample by mounting the condenser lens before the sample. Read its description. Align it and place it one focal length before the sample. Fine tune the position so that the rays are focused at the sample.

7. Add an iris that is called the 'Aperture Stop' by mounting this optic before the condenser. Align it and position it one focal length behind the condenser. Notice that you can open and close the iris in the Side View. For now, open the aperture stop all the way so all the light rays can get through.

8. Next, we want to image the light source onto the aperture stop. Since the aperture stop is one focal length behind the condenser, whatever is imaged at the aperture stop will be completely out of focus at the sample plane. We can do this by changing our rays to be a point source and getting the rays to overlap at the aperture stop. In the Rays tab, change 'Rays shown' to be 'Point source' and click 'Create Rays'.

9. Mount the collector lens between the aperture stop and the light source. Align the lens and slide it on the rail until the rays overlap at the aperture stop.

10. If the rays are focused at the aperture stop, they should be collimated as they pass through the sample. You can fine tune the position of the condenser to make sure that's true. The rays should also be collimated after the tube lens. You can fine tune its position to make sure that's true. If the central ray is deviating off the main optical axis, you can fine tune the position of the lenses to try to straighten it out. Notice that rays that are overlapped at the light source are completely defocused at the sample and after the tube lens, where the camera would be. This means that the light source is evenly illuminating our sample and will not give us false features on our image.

11. Switch back to collimated light in the Rays tab. The rays should be focused at the sample, collimated after the objective lens, and come to a focus after

the tube lens, so that the sample is imaged wherever those rays overlap. If they're not perfect, adjust the position of your sample, then your objective lens.

12. You can switch back and forth between looking at rays from a point source or collimated rays to get your microscope's alignment to be as close to perfect as possible.

13. Once you have perfected your alignment, show the collimated rays. Look at the overlap of the rays after the tube lens. Notice that the overlap isn't perfect. This may partially be due to imperfect alignment of your optics, but even if you have perfect alignment, this overlap will still not be perfect. This is because of spherical aberrations: this simulation uses spherical lenses, and while they are cheaper to manufacture (in real life), they don't perfectly bend light to a focused spot. In a research-grade microscope, many of these lenses will be replaced with 'aspherical lenses' that are specially designed to give a tighter focus.

14. In the Rays tab, change your wavelength. Notice that the overlap changes. This is most apparent at bluer wavelengths. For example, the change in focus from 350-400 nm is much larger than the change from 650-700 nm. In lab, you'll first use lenses like those in this simulation, and then you'll try a type of lens called an achromat: they are comprised of two different types of materials, with different indices of refraction, so the focal lengths do not change as much for different wavelengths.

15. Go back to the best wavelength to showcase how well aligned your microscope is. Make sure your best microscope is shown on the screen. **Make sure you**

close the program so your work will be submitted. Note the date and time when you closed the program with your best microscope: _____ Submit this worksheet with your pre-lab.

B.4 Surveys

Survey adapted from J. Chem. Ed. 92, 1149 (2015) "Development of an Assessment Tool to Measure Students' Meaningful Learning in the Undergraduate Chemistry Laboratory". **Table B.5** lists the item classifications based on meaningful learning category (C= Cognitive; A=Affective; C/A=Cognitive/Affective) and how the item affects meaningful learning (+ = positive contribution to meaningful; - = hinders meaningful learning). These classifications are the same for both the pre and post.

When performing experiments in this chemistry laboratory, I expect... (1 = disagree to 10 = agree)		
Number	Score	Question
1		to learn science that will be useful in my life.
2		to worry about finishing on time.
3		to make decisions about what data to collect.
4		to feel unsure about the purpose of the procedures.
5		to experience moments of insight.
6		to be confused about how the instruments work.
7		to learn critical thinking skills.
8		to be excited to do the activity.
9		to be nervous about making mistakes.
10		to consider if my data makes sense.
11		to think about what the light is doing.
12		to feel disorganized.
13		to develop confidence in the laboratory.
14		to worry about getting good data.
15		the procedures to be simple to do.
16		to be confused about the underlying concepts.
17		to "get stuck" but keep trying.
18		to get nervous when handling equipment.
19		to think about concepts I already know.
20		to worry about the quality of my data.
21		to be frustrated.
22		to interpret my data beyond only doing calculations.
23		We use this statement to discard the survey of people who are not reading the questions. Please select forty percent for this question.
24		to focus on procedures, not concepts.
25		to use my observations to understand the behavior of light.
26		to make mistakes and try again.
27		to be intrigued by the instruments.
28		to feel intimidated.
29		to be confused about what my data mean.
30		to be confident when using equipment.
31		to learn problem solvent skills.

Table B.3. Survey before performing in-laboratory activities

When I performed experiments in this chemistry laboratory, I. . . (1 = disagree to 10 = agree)		
Number	Score	Question
1		learned science that will be useful in my life.
2		worried about finishing on time.
3		made decisions about what data to collect.
4		felt unsure about the purpose of the procedures.
5		experienced moments of insight.
6		was confused about how the instruments work.
7		learned critical thinking skills.
8		was excited to do the activity.
9		was nervous about making mistakes.
10		considered if my data makes sense.
11		thought about what the light is doing.
12		felt disorganized.
13		developed confidence in the laboratory.
14		worried about getting good data.
15		thought the procedures to be simple to do.
16		was confused about the underlying concepts.
17		"got stuck" but keep trying.
18		was nervous when handling equipment.
19		thought about concepts I already know.
20		worried about the quality of my data.
21		was frustrated.
22		interpreted my data beyond only doing calculations.
23		We use this statement to discard the survey of people who are not reading the questions. Please select sixty percent for this question.
24		focused on procedures, not concepts.
25		used my observations to understand the behavior of light.
26		made mistakes and try again.
27		was intrigued by the instruments.
28		felt intimidated.
29		was confused about what my data mean.
30		was confident when using equipment.
31		learned problem solvent skills.

Table B.4. Survey after performing in-laboratory activities

When performing experiments in this chemistry laboratory this semester, I expect... (1 = disagree to 10 = agree)			
Number	Type	Class	Question
1	C/A	+	to learn science that will be useful in my life.
2	A	-	to worry about finishing on time.
3	C	+	to make decisions about what data to collect.
4	C/A	-	to feel unsure about the purpose of the procedures.
5	C	+	to experience moments of insight.
6	C	-	to be confused about how the instruments work.
7	C	+	to learn critical thinking skills.
8	A	+	to be excited to do the activity.
9	A	-	to be nervous about making mistakes.
10	C	+	to consider if my data makes sense.
11	C	+	to think about what the light is doing.
12	C/A	-	to feel disorganized.
13	A	+	to develop confidence in the laboratory.
14	C/A	-	to worry about getting good data.
15	C	-	the procedures to be simple to do.
16	C	-	to be confused about the underlying concepts.
17	C	+	to "get stuck" but keep trying.
18	A	-	to get nervous when handling equipment.
19	C	+	to think about concepts I already know.
20	C/A	-	to worry about the quality of my data.
21	A	-	to be frustrated.
22	C	+	to interpret my data beyond only doing calculations.
23			We use this statement to discard the survey of people who are not reading the questions. Please select forty percent for this question.
24	C	-	to focus on procedures, not concepts.
25	C	+	to use my observations to understand the behavior of light.
26	C	+	to make mistakes and try again.
27	C/A	+	to be intrigued by the instruments.
28	A	-	to feel intimidated.
29	C	-	to be confused about what my data mean.
30	A	+	to be confident when using equipment.
31	C	+	to learn problem solvent skills.

Table B.5. Survey item classification

(1 = disagree to 10 = agree)		
Letter	Score	Question
A		The simulation helped me understand the concepts in this laboratory.
B		This simulation helped me feel more comfortable working with optics.
C		This simulation increased my confidence for the in-lab activity.
D		This simulation helped me visualize what is occuring while building a microscope.
E		This simulation made me more excited about performing the in-lab activity.
F		The simulation made the in-lab activity go more smoothly.
G		The simulation was a good use of my time.

Table B.6. Additional survey questions

REFERENCES CITED

(1) Mainville, M.; Leclerc, M. *ACS Energy Letters* **2020**, *5*, 1186–1197.

(2) Ng, L. W. T.; Lee, S. W.; Chang, D. W.; Hodgkiss, J. M.; Vak, D. *Advanced Materials Technologies* **2022**, 2101556.

(3) Sampaio, P. G. V.; González, M. O. A.; Oliveira Ferreira, P.; Cunha Jácome Vidal, P.; Pereira, J. P. P.; Ferreira, H. R.; Oprime, P. C. *International Journal of Energy Research* **2020**, *44*, 9912–9931.

(4) Salehi, A.; Fu, X.; Shin, D.; So, F. *Advanced Functional Materials* **2019**, *29*, 1808803.

(5) Wadsworth, A.; Hamid, Z.; Kosco, J.; Gasparini, N.; McCulloch, I. *Advanced Materials* **2020**, *32*, 2001763.

(6) Wadsworth, A.; Moser, M.; Marks, A.; Little, M. S.; Gasparini, N.; Brabec, C. J.; Baran, D.; McCulloch, I. *Chemical Society Reviews* **2019**, *48*, 1596–1625.

(7) Luscombe, C. K.; Maitra, U.; Walter, M.; Wiedmer, S. K. *Chemistry Teacher International* **2021**, *3*, 169–183.

(8) Chen, D.; Li, W.; Gan, L.; Wang, Z.; Li, M.; Su, S.-J. *Materials Science and Engineering: R: Reports* **2020**, *142*, 100581.

(9) Mahoro, G. U.; Fernandez-Cestau, J.; Renaud, J.; Coto, P. B.; Costa, R. D.; Gaillard, S. *Advanced Optical Materials* **2020**, *8*, 2000260.

(10) Hong, G.; Gan, X.; Leonhardt, C.; Zhang, Z.; Seibert, J.; Busch, J. M.; Bräse, S. *Advanced Materials* **2021**, *33*, 2005630.

(11) Song, J.; Lee, H.; Jeong, E. G.; Choi, K. C.; Yoo, S. *Advanced Materials* **2020**, *32*, 1907539.

(12) Huang, Y.; Hsiang, E.-L.; Deng, M.-Y.; Wu, S.-T. *Light: Science & Applications* **2020**, *9*, 105.

(13) Meredith, P.; Li, W.; Armin, A. *Advanced Energy Materials* **2020**, *10*, 2001788.

(14) Zhao, W.; Li, S.; Yao, H.; Zhang, S.; Zhang, Y.; Yang, B.; Hou, J. *Journal of the American Chemical Society* **2017**, *139*, 7148–7151.

(15) Zhu, L. et al. *Nature Materials* **2022**,

(16) Ryu, M. S.; Cha, H. J.; Jang, J. *Current Applied Physics* **2010**, *10*, S206–S209.

(17) Xian, K.; Liu, Y.; Liu, J.; Yu, J.; Xing, Y.; Peng, Z.; Zhou, K.; Gao, M.; Zhao, W.; Lu, G.; Zhang, J.; Hou, J.; Geng, Y.; Ye, L. *Journal of Materials Chemistry A* **2022**, *10*, 3418–3429.

(18) Wang, Z.; Li, J.; Du, J.; Ren, C.; Lu, F.; Deng, Q. *Dyes and Pigments* **2024**, *224*, 111984.

(19) Zhou, D.; Li, Y.; Zhang, H.; Zheng, H.; Shen, X.; You, W.; Hu, L.; Han, L.; Tong, Y.; Chen, L. *Chemical Engineering Journal* **2023**, *452*, 139260.

(20) Lin, Y.; Wang, J.; Zhang, Z.-G.; Bai, H.; Li, Y.; Zhu, D.; Zhan, X. *Advanced Materials* **2015**, *27*, 1170–1174.

(21) Yuan, J.; Zhang, Y.; Zhou, L.; Zhang, G.; Yip, H.-L.; Lau, T.-K.; Lu, X.; Zhu, C.; Peng, H.; Johnson, P. A.; Leclerc, M.; Cao, Y.; Ulanski, J.; Li, Y.; Zou, Y. *Joule* **2019**, *3*, 1140–1151.

(22) Diao, Y.; Shaw, L.; Bao, Z.; Mannsfeld, S. C. B. *Energy & Environmental Science* **2014**, *7*, 2145–2159.

(23) Larson, R. G. *Nature* **2017**, *550*, 466–467.

(24) Hall, D. B.; Underhill, P.; Torkelson, J. M. *Polymer Engineering & Science* **1998**, *38*, 2039–2045.

(25) Yang, F.; Huang, Y.; Li, Y.; Li, Y. *npj Flexible Electronics* **2021**, *5*, 30.

(26) Wang, G.; Adil, M. A.; Zhang, J.; Wei, Z. *Advanced Materials* **2019**, *31*, 1805089.

(27) Carlé, J. E.; Helgesen, M.; Hagemann, O.; Hösel, M.; Heckler, I. M.; Bundgaard, E.; Gevorgyan, S. A.; Søndergaard, R. R.; Jørgensen, M.; García-Valverde, R.; Chaouki-Almagro, S.; Villarejo, J. A.; Krebs, F. C. *Joule* **2017**, *1*, 274–289.

(28) Seifrid, M. T.; Oosterhout, S. D.; Toney, M. F.; Bazan, G. C. *ACS Omega* **2018**, *3*, 10198–10204.

(29) Rivnay, J.; Steyrleuthner, R.; Jimison, L. H.; Casadei, A.; Chen, Z.; Toney, M. F.; Facchetti, A.; Neher, D.; Salleo, A. *Macromolecules* **2011**, *44*, 5246–5255.

(30) Zhang, Y.; Sajjad, M. T.; Blaszczyk, O.; Parnell, A. J.; Ruseckas, A.; Serrano, L. A.; Cooke, G.; Samuel, I. D. W. *Chemistry of Materials* **2019**, *31*, 6548–6557.

(31) Serbenta, A.; Kozlov, O. V.; Portale, G.; van Loosdrecht, P. H. M.; Pshenichnikov, M. S. *Scientific Reports* **2016**, *6*, 36236.

(32) Markov, D. E.; Amsterdam, E.; Blom, P. W. M.; Sieval, A. B.; Hummelen, J. C. *The Journal of Physical Chemistry A* **2005**, *109*, 5266–5274.

(33) Miller, S.; Fanchini, G.; Lin, Y.-Y.; Li, C.; Chen, C.-W.; Su, W.-F.; Chhowalla, M. *Journal of Materials Chemistry* **2008**, *18*, 306–312.

(34) Marsh, R. A.; Hodgkiss, J. M.; Albert-Seifried, S.; Friend, R. H. *Nano Letters* **2010**, *10*, 923–930.

(35) Cui, C.; Li, Y. *Aggregate* **2021**, *2*.

(36) Zheng, C.; Penmetcha, A. R.; Cona, B.; Spencer, S. D.; Zhu, B.; Heaphy, P.; Cody, J. A.; Collison, C. J. *Langmuir* **2015**, *31*, 7717–7726.

(37) Zheng, C.; Bleier, D.; Jalan, I.; Pristash, S.; Penmetcha, A. R.; Hestand, N. J.; Spano, F. C.; Pierce, M. S.; Cody, J. A.; Collison, C. J. *Solar Energy Materials and Solar Cells* **2016**, *157*, 366–376.

(38) Wiegand, T.; Smith, H.; Ryczek, C.; Cruz, A.; Cody, J.; Collison, C. J.; Burson, K. *The Journal of Physical Chemistry C* **2022**, *126*, 14791–14800.

(39) Yamagata, H.; Spano, F. C. *The Journal of Chemical Physics* **2012**, *136*, 184901.

(40) Oleson, A.; Zhu, T.; Dunn, I. S.; Bialas, D.; Bai, Y.; Zhang, W.; Dai, M.; Reichman, D. R.; Tempelaar, R.; Huang, L.; Spano, F. C. *The Journal of Physical Chemistry C* **2019**, *123*, 20567–20578.

(41) Sosa, M. L.; Wong, C. Y. *The Journal of Chemical Physics* **2020**, *153*, 214902.

(42) Zhong, C.; Bialas, D.; Collison, C. J.; Spano, F. C. *The Journal of Physical Chemistry C* **2019**, *123*, 18734–18745.

(43) Hestand, N. J.; Zheng, C.; Penmetcha, A. R.; Cona, B.; Cody, J. A.; Spano, F. C.; Collison, C. J. *The Journal of Physical Chemistry C* **2015**, *119*, 18964–18974.

(44) Spano, F. C. *The Journal of Chemical Physics* **2005**, *122*, 234701.

(45) Spano, F. C. *Chemical Physics* **2006**, *325*, 22–35.

(46) Spano, F. C. *Accounts of Chemical Research* **2010**, *43*, 429–439.

(47) Stradomska, A.; Petelenz, P. *The Journal of Chemical Physics* **2009**, *131*, 044507.

(48) Abdelsamie, M.; Zhao, K.; Niazi, M. R.; Chou, K. W.; Amassian, A. *Journal of Materials Chemistry C* **2014**, *2*, 3373–3381.

(49) Buchhorn, M.; Wedler, S.; Panzer, F. *The Journal of Physical Chemistry A* **2018**, *122*, 9115–9122.

(50) Zomerman, D.; Kong, J.; McAfee, S. M.; Welch, G. C.; Kelly, T. L. *ACS Applied Energy Materials* **2018**, *1*, 5663–5674.

(51) van Franeker, J. J.; Turbiez, M.; Li, W.; Wienk, M. M.; Janssen, R. A. J. *Nature Communications* **2015**, *6*, 6229.

(52) Shin, N.; Richter, L. J.; Herzing, A. A.; Kline, R. J.; DeLongchamp, D. M. *Advanced Energy Materials* **2013**, *3*, 938–948.

(53) Gunkel, I.; Gu, X.; Sun, Z.; Schaible, E.; Hexemer, A.; Russell, T. P. *Journal of Polymer Science Part B: Polymer Physics* **2016**, *54*, 331–338.

(54) Sims, M.; Zheng, K.; Quiles, M. C.; Xia, R.; Stavrinou, P. N.; Bradley, D. D. C.; Etchegoin, P. *Journal of Physics: Condensed Matter* **2005**, *17*, 6307–6318.

(55) Engmann, S.; Bokel, F. A.; Ro, H. W.; DeLongchamp, D. M.; Richter, L. J. *Advanced Energy Materials* **2016**, *6*, 1502011.

(56) Campoy-Quiles, M.; Alonso, M. I.; Bradley, D. D. C.; Richter, L. J. *Advanced Functional Materials* **2014**, *24*, 2116–2134.

(57) Ando, M.; Yoneya, M.; Kehoe, T. B.; Ishii, H.; Minakata, T.; Kawasaki, M.; Duffy, C. M.; Phillips, R.; Sirringhaus, H. *Physical Review Materials* **2019**, *3*, 025601.

(58) Schönherr, H.; Frank, C. W. *Macromolecules* **2003**, *36*, 1188–1198.

(59) Kim, Y.-J.; Lee, S.; Niazi, M. R.; Hwang, K.; Tang, M.-C.; Lim, D.-H.; Kang, J.-S.; Smilgies, D.-M.; Amassian, A.; Kim, D.-Y. *ACS Applied Materials & Interfaces* **2020**, *12*, 36417–36427.

(60) Baran, D. et al. *Nature Materials* **2017**, *16*, 363–369.

(61) Jiang, X.; Chotard, P.; Luo, K.; Eckmann, F.; Tu, S.; Reus, M. A.; Yin, S.; Reitenbach, J.; Weindl, C. L.; Schwartzkopf, M.; Roth, S. V.; Müller-Buschbaum, P. *Advanced Energy Materials* **2022**, 2103977.

(62) Posselt, D.; Zhang, J.; Smilgies, D.-M.; Berezkin, A. V.; Potemkin, I. I.; Papadakis, C. M. *Progress in Polymer Science* **2017**, *66*, 80–115.

(63) Güldal, N. S.; Kassar, T.; Berlinghof, M.; Ameri, T.; Osvet, A.; Pacios, R.; Destri, G. L.; Unruh, T.; Brabec, C. J. *Journal of Materials Chemistry C* **2016**, *4*, 2178–2186.

(64) Berera, R.; van Grondelle, R.; Kennis, J. T. M. *Photosynthesis Research* **2009**, *101*, 105–118.

(65) Couairon, A.; Mysyrowicz, A. *Physics Reports* **2007**, *441*, 47–189.

(66) Bakulin, A. A.; Dimitrov, S. D.; Rao, A.; Chow, P. C. Y.; Nielsen, C. B.; Schroeder, B. C.; McCulloch, I.; Bakker, H. J.; Durrant, J. R.; Friend, R. H. *The Journal of Physical Chemistry Letters* **2013**, *4*, 209–215.

(67) Ohkita, H.; Cook, S.; Astuti, Y.; Duffy, W.; Tierney, S.; Zhang, W.; Heeney, M.; McCulloch, I.; Nelson, J.; Bradley, D. D. C.; Durrant, J. R. *Journal of the American Chemical Society* **2008**, *130*, 3030–3042.

(68) Kandada, A. R. S.; Grancini, G.; Petrozza, A.; Perissinotto, S.; Fazzi, D.; Raavi, S. S. K.; Lanzani, G. *Scientific Reports* **2013**, *3*, 2073.

(69) E. Hartnett, P.; M. Dyar, S.; A. Margulies, E.; E. Shoer, L.; W. Cook, A.; W. Eaton, S.; J. Marks, T.; R. Wasielewski, M. *Chemical Science* **2015**, *6*, 402–411.

(70) Falke, S. M.; Rozzi, C. A.; Brida, D.; Maiuri, M.; Amato, M.; Sommer, E.; De Sio, A.; Rubio, A.; Cerullo, G.; Molinari, E.; Lienau, C. *Science* **2014**, *344*, 1001–1005.

(71) Rana, A.; Sharma, C.; Prabhu, D. D.; Kumar, M.; Karuvath, Y.; Das, S.; Chand, S.; Singh, R. K. *AIP Advances* **2018**, *8*, 045302.

(72) Hinrichsen, T. F.; Chan, C. C. S.; Ma, C.; Paleček, D.; Gillett, A.; Chen, S.; Zou, X.; Zhang, G.; Yip, H.-L.; Wong, K. S.; Friend, R. H.; Yan, H.; Rao, A.; Chow, P. C. Y. *Nature Communications* **2020**, *11*, 5617.

(73) Dong, Y.; Cha, H.; Bristow, H. L.; Lee, J.; Kumar, A.; Tuladhar, P. S.; McCulloch, I.; Bakulin, A. A.; Durrant, J. R. *Journal of the American Chemical Society* **2021**, *143*, 7599–7603.

(74) Dimitriev, O. P.; Blank, D. A.; Ganser, C.; Teichert, C. *The Journal of Physical Chemistry C* **2018**, *122*, 17096–17109.

(75) Wilson, K. S.; Mapile, A. N.; Wong, C. Y.; Wong, C. Y.; Wong, C. Y. *Optics Express* **2020**, *28*, 11339–11355.

(76) Malley, M. M.; Rentzepis, P. M. *Chemical Physics Letters* **1969**, *3*, 534–536.

(77) Salin, F.; Georges, P.; Roger, G.; Brun, A. *Applied Optics* **1987**, *26*, 4528–4531.

(78) Dhar, L.; Fourkas, J. T.; Nelson, K. A. *Optics Letters* **1994**, *19*, 643–645.

(79) Fujimoto, M.; Aoshima, S.-i.; Tsuchiya, Y. *Measurement Science and Technology* **2002**, *13*, 1698–1709.

(80) Furukawa, N.; Mair, C. E.; Kleiman, V. D.; Takeda, J. *Applied Physics Letters* **2004**, *85*, 4645.

(81) Makishima, Y.; Furukawa, N.; Ishida, A.; Takeda, J. *Japanese Journal of Applied Physics* **2006**, *45*, 5986.

(82) Ferrari, R.; D'Andrea, C.; Bassi, A.; Valentini, G.; Cubeddu, R. Time-gated real-time pump-probe imaging spectroscopy. Novel Optical Instrumentation for Biomedical Applications III (2007), paper 6631_46. 2007; p 6631_46.

(83) Wilson, K. S.; Scott, M. N.; Wong, C. Y. *MRS Advances* **2018**, *3*, 3453–3457.

(84) Topp, M. R.; Rentzepis, P. M.; Jones, R. P. *Journal of Applied Physics* **1971**, *42*, 3415–3419.

(85) Wakeham, G. P.; Nelson, K. A. *Optics Letters* **2000**, *25*, 505–507.

(86) Wakeham, G. P.; Chung, D. D.; Nelson, K. A. *Thermochimica Acta* **2002**, *384*, 7–21.

(87) Poulin, P. R.; Nelson, K. A. *Science* **2006**, *313*, 1756–1760.

(88) Katayama, I.; Sakaibara, H.; Takeda, J. *Japanese Journal of Applied Physics* **2011**, *50*, 102701.

(89) Minami, Y.; Yamaki, H.; Katayama, I.; Takeda, J. *Applied Physics Express* **2014**, *7*, 022402.

(90) Shin, T.; Wolfson, J. W.; Teitelbaum, S. W.; Kandyla, M.; Nelson, K. A. *Review of Scientific Instruments* **2014**, *85*, 083115.

(91) Yang, J.; Zhou, W.; Wang, F.; Deng, K.; Yi, T.; Shen, L.; Fang, Y.; Yang, Y.; Song, Y. *Applied Physics B* **2020**, *126*, 98.

(92) Wilson, K. S.; Walbrun, Z. S.; Wong, C. Y. *Spectrochimica Acta Part A: Molecular and Biomolecular Spectroscopy* **2021**, *253*, 119557.

(93) Whaley, K. B.; Kocherzhenko, A. A.; Nitzan, A. *The Journal of Physical Chemistry C* **2014**, *118*, 27235–27244.

(94) Piris, J.; Dykstra, T. E.; Bakulin, A. A.; Loosdrecht, P. H. v.; Knulst, W.; Trinh, M. T.; Schins, J. M.; Siebbeles, L. D. *The Journal of Physical Chemistry C* **2009**, *113*, 14500–14506.

(95) Stevens, M. A.; Silva, C.; Russell, D. M.; Friend, R. H. *Physical Review B* **2001**, *63*, 165213.

(96) Zarrabi, N.; Burn, P. L.; Meredith, P.; Shaw, P. E. *The Journal of Physical Chemistry Letters* **2016**, *7*, 2640–2646.

(97) Guo, J.; Ohkita, H.; Benten, H.; Ito, S. *Journal of the American Chemical Society* **2009**, *131*, 16869–16880.

(98) Kaake, L. G.; Moses, D.; Heeger, A. J. *The Journal of Physical Chemistry Letters* **2013**, *4*, 2264–2268.

(99) Uteza, O.; Bussière, B.; Canova, F.; Chambaret, J.-P.; Delaporte, P.; Itina, T.; Sentis, M. *Applied Surface Science* **2007**, *254*, 799–803.

(100) Fork, R. L.; Tomlinson, W. J.; Shank, C. V.; Hirlimann, C.; Yen, R. *Optics Letters* **1983**, *8*, 1.

(101) Tcypkin, A. N.; Putilin, S. E.; Melnik, M. V.; Makarov, E. A.; Bespalov, V. G.; Kozlov, S. A. *Applied Optics* **2016**, *55*, 8390.

(102) Dharmadhikari, J. A.; Steinmeyer, G.; Gopakumar, G.; Mathur, D.; Dharmadhikari, A. K. *Optics Letters* **2016**, *41*, 3475.

(103) Corkum, P. B.; Rolland, C.; Srinivasan-Rao, T. *Physical Review Letters* **1986**, *57*, 2268–2271.

(104) Kosma, K.; Trushin, S. A.; Fuß, W.; Schmid, W. E. *Journal of Modern Optics* **2008**, *55*, 2141–2177.

(105) Wilson, K. S.; Scott, M. N.; Wong, C. Y. *Synthetic Metals* **2019**, *250*, 115–120.

(106) Riede, M.; Spoltore, D.; Leo, K. *Advanced Energy Materials* **2021**, *11*, 2002653.

(107) Ma, W.; Yang, C.; Gong, X.; Lee, K.; Heeger, A. J. *Advanced Functional Materials* **2005**, *15*, 1617–1622.

(108) Zhang, J.; Tan, H. S.; Guo, X.; Facchetti, A.; Yan, H. *Nature Energy* **2018**, *3*, 720–731.

(109) Yan, C.; Barlow, S.; Wang, Z.; Yan, H.; Jen, A. K.-Y.; Marder, S. R.; Zhan, X. *Nature Reviews Materials* **2018**, *3*, 1–19.

(110) Chatterjee, S.; Jinnai, S.; Ie, Y. *Journal of Materials Chemistry A* **2021**, *9*, 18857–18886.

(111) Verploegen, E.; Mondal, R.; Bettinger, C. J.; Sok, S.; Toney, M. F.; Bao, Z. *Advanced Functional Materials* **2010**, *20*, 3519–3529.

(112) Holliday, S. et al. *Nature Communications* **2016**, *7*, 11585.

(113) Kaake, L. G.; Barbara, P. F.; Zhu, X.-Y. *The Journal of Physical Chemistry Letters* **2010**, *1*, 628–635.

(114) Du, B.; Yi, J.; Yan, H.; Wang, T. *Chemistry – A European Journal* **2021**, *27*, 2908–2919.

(115) Kasha, M. *Radiation Research* **1963**, *20*, 55–70.

(116) Spano, F. C.; Silva, C. *Annual Review of Physical Chemistry* **2014**, *65*, 477–500.

(117) Rahimi, K.; Botiz, I.; O. Agumba, J.; Motamen, S.; Stingelin, N.; Reiter, G. *RSC Advances* **2014**, *4*, 11121–11123.

(118) Wu, T.; Pfohl, T.; Chandran, S.; Sommer, M.; Reiter, G. *Macromolecules* **2020**, *53*, 8303–8312.

(119) Niles, E. T.; Roehling, J. D.; Yamagata, H.; Wise, A. J.; Spano, F. C.; Moulé, A. J.; Grey, J. K. *The Journal of Physical Chemistry Letters* **2012**, *3*, 259–263.

(120) Hellmann, C.; Paquin, F.; Treat, N. D.; Bruno, A.; Reynolds, L. X.; Haque, S. A.; Stavrinou, P. N.; Silva, C.; Stingelin, N. *Advanced Materials* **2013**, *25*, 4906–4911.

(121) Agumba, J. O. **2016**,

(122) Thiessen, A.; Vogelsang, J.; Adachi, T.; Steiner, F.; Vanden Bout, D.; Lupton, J. M. *Proceedings of the National Academy of Sciences* **2013**, *110*.

(123) Oh, J. Y.; Lee, T. I.; Myoung, J.; Jeong, U.; Baik, H. K. *Macromolecular Rapid Communications* **2011**, *32*, 1066–1071.

(124) Oh, J. Y.; Shin, M.; Lee, T. I.; Jang, W. S.; Min, Y.; Myoung, J.-M.; Baik, H. K.; Jeong, U. *Macromolecules* **2012**, *45*, 7504–7513.

(125) Li, G.; Shrotriya, V.; Yao, Y.; Yang, Y. *Journal of Applied Physics* **2005**, *98*, 043704.

(126) Mihailetchi, V. D.; Xie, H. X.; deBoer, B.; Koster, L. J. A.; Blom, P. W. M. *Advanced Functional Materials* **2006**, *16*, 699–708.

(127) Hwang, I.-W.; Moses, D.; Heeger, A. J. *The Journal of Physical Chemistry C* **2008**, *112*, 4350–4354.

(128) Kirkpatrick, J.; Keivanidis, P. E.; Bruno, A.; Ma, F.; Haque, S. A.; Yarstev, A.; Sundstrom, V.; Nelson, J. *The Journal of Physical Chemistry B* **2011**, *115*, 15174–15180.

(129) Oyewole, D. O.; Oyewole, O. K.; Kushnir, K.; Shi, T.; Oyelade, O. V.; Adeniji, S. A.; Agyei-Tuffour, B.; Evans-Lutterodt, K.; Titova, L. V.; Soboyejo, W. O. *AIP Advances* **2021**, *11*, 045304.

(130) Agostinelli, T.; Lilliu, S.; Labram, J. G.; Campoy-Quiles, M.; Hampton, M.; Pires, E.; Rawle, J.; Bikondoa, O.; Bradley, D. D. C.; Anthopoulos, T. D.; Nelson, J.; Macdonald, J. E. *Advanced Functional Materials* **2011**, *21*, 1701–1708.

(131) Joshi, S.; Pingel, P.; Grigorian, S.; Panzner, T.; Pietsch, U.; Neher, D.; Forster, M.; Scherf, U. *Macromolecules* **2009**, *42*, 4651–4660.

(132) Pingel, P.; Zen, A.; Abellón, R. D.; Grozema, F. C.; Siebbeles, L. D.; Neher, D. *Advanced Functional Materials* **2010**, *20*, 2286–2295.

(133) Treat, N. D.; Shuttle, C. G.; Toney, M. F.; Hawker, C. J.; Chabinyc, M. L. *Journal of Materials Chemistry* **2011**, *21*, 15224–15231.

(134) Walbrun, Z. S.; Wong, C. Y. In Situ Transient Absorption During Thermal Annealing of a Polymer: Fullerene Blend. Frontiers in Optics + Laser Science 2023 (FiO, LS). Tacoma, Washington, 2023; p JTu5A.8.

(135) Inganäs, O.; Gustafsson, G.; Salaneck, W.; Österholm, J.; Laakso, J. *Synthetic Metals* **1989**, *28*, 377–384.

(136) Onoda, M.; Tada, K. *Thin Solid Films* **2003**, *438-439*, 187–194.

(137) Ogata, Y.; Kawaguchi, D.; Tanaka, K. *Scientific Reports* **2015**, *5*, 8436.

(138) Zen, A.; Pflaum, J.; Hirschmann, S.; Zhuang, W.; Jaiser, F.; Asawapirom, U.; Rabe, J.; Scherf, U.; Neher, D. *Advanced Functional Materials* **2004**, *14*, 757–764.

(139) Cho, S.; Lee, K.; Yuen, J.; Wang, G.; Moses, D.; Heeger, A. J.; Surin, M.; Lazzaroni, R. *Journal of Applied Physics* **2006**, *100*, 114503.

(140) Gu, K.; Wang, Y.; Li, R.; Tsai, E.; Onorato, J. W.; Luscombe, C. K.; Priestley, R. D.; Loo, Y.-L. *ACS Applied Materials & Interfaces* **2021**, *13*, 999–1007.

(141) Grancini, G.; Polli, D.; Fazzi, D.; Cabanillas-Gonzalez, J.; Cerullo, G.; Lanzani, G. *The Journal of Physical Chemistry Letters* **2011**, *2*, 1099–1105.

(142) Dimitriev, O. P. *Nanoscale Research Letters* **2017**, *12*, 510.

(143) Zhao, J.; Swinnen, A.; Van Assche, G.; Manca, J.; Vanderzande, D.; Mele, B. V. *The Journal of Physical Chemistry B* **2009**, *113*, 1587–1591.

(144) Chen, G.; Sasabe, H.; Sasaki, Y.; Katagiri, H.; Wang, X.-F.; Sano, T.; Hong, Z.; Yang, Y.; Kido, J. *Chemistry of Materials* **2014**, *26*, 1356–1364.

(145) Lynch, D. E.; Byriel, K. A. *Crystal Engineering* **1999**, *2*, 225–239.

(146) Spencer, S. D.; Bougher, C.; Heaphy, P. J.; Murcia, V. M.; Gallivan, C. P.; Monfette, A.; Andersen, J. D.; Cody, J. A.; Conrad, B. R.; Collison, C. J. *Solar Energy Materials and Solar Cells* **2013**, *112*, 202–208.

(147) Balzer, F.; Kollmann, H.; Schulz, M.; Schnakenburg, G.; Lützen, A.; Schmidtmann, M.; Lienau, C.; Silies, M.; Schiek, M. *Crystal Growth & Design* **2017**, *17*, 6455–6466.

(148) Tristani-Kendra, M.; Eckhardt, C. J.; Bernstein, J.; Goldstein, E. *Chemical Physics Letters* **1983**, *98*, 57–61.

(149) Zheng, C.; Mark, M. F.; Wiegand, T.; Diaz, S. A.; Cody, J.; Spano, F. C.; McCamant, D. W.; Collison, C. J. *The Journal of Physical Chemistry C* **2020**, *124*, 4032–4043.

(150) Walbrun, Z. S.; Leibfried, L. C.; Hoban, R.; Rasmussen, B. C.; Wiegand, T. J.; Collison, C. J.; Wong, C. Y. *MRS Advances* **2022**, *7*, 239–244.

(151) Zheng, C.; Zhong, C.; Collison, C. J.; Spano, F. C. *The Journal of Physical Chemistry C* **2019**, *123*, 3203–3215.

(152) Yu, H.; Fu, M.; Xiao, Y. *Physical Chemistry Chemical Physics* **2010**, *12*, 7386–7391.

(153) Wiegand, T. J.; Sandoval, J. S.; Cody, J. A.; McCamant, D. W.; Collison, C. J. *The Journal of Physical Chemistry C* **2024**, *128*, 4616–4630.

(154) van Stokkum, I. H. M.; Larsen, D. S.; van Grondelle, R. *Biochimica et Biophysica Acta (BBA) - Bioenergetics* **2004**, *1657*, 82–104.

(155) Terenziani, F.; Painelli, A.; Katan, C.; Charlot, M.; Blanchard-Desce, M. *Journal of the American Chemical Society* **2006**, *128*, 15742–15755.

(156) Shafeekh, K. M.; Das, S.; Sissa, C.; Painelli, A. *The Journal of Physical Chemistry B* **2013**, *117*, 8536–8546.

(157) Balzer, F.; Hestand, N. J.; Zablocki, J.; Schnakenburg, G.; Lützen, A.; Schiek, M. *The Journal of Physical Chemistry C* **2022**, *126*, 13802–13813.

(158) Solak, E. K.; Irmak, E. *RSC Advances* **2023**, *13*, 12244–12269.

(159) Liu, C.; Xiao, C.; Xie, C.; Li, W. *Nano Energy* **2021**, *89*, 106399.

(160) Beaumont, N.; Hancox, I.; Sullivan, P.; Hatton, R. A.; Jones, T. S. *Energy & Environmental Science* **2011**, *4*, 1708.

(161) Dash, B. P.; Kumar Beriha, S.; Naik, B.; Kumar Sahoo, P. *Materials Today: Proceedings* **2022**, *67*, 1057–1063.

(162) Søndergaard, R. R.; Hösel, M.; Krebs, F. C. *Journal of Polymer Science Part B: Polymer Physics* **2013**, *51*, 16–34.

(163) Coropceanu, V.; Chen, X.-K.; Wang, T.; Zheng, Z.; Brédas, J.-L. *Nature Reviews Materials* **2019**, *4*, 689–707.

(164) Suzuki, F.; Kubo, S.; Fukushima, T.; Kaji, H. *Scientific Reports* **2018**, *8*, 5203.

(165) Gu, K. L.; Zhou, Y.; Gu, X.; Yan, H.; Diao, Y.; Kurosawa, T.; Ganapathysubramanian, B.; Toney, M. F.; Bao, Z. *Organic Electronics* **2017**, *40*, 79–87.

(166) Feng, X.; Ding, X.; Chen, L.; Wu, Y.; Liu, L.; Addicoat, M.; Irle, S.; Dong, Y.; Jiang, D. *Scientific Reports* **2016**, *6*, 32944.

(167) Urbani, M.; Ragoussi, M.-E.; Nazeeruddin, M. K.; Torres, T. *Coordination Chemistry Reviews* **2019**, *381*, 1–64.

(168) Bian, Y.; Chen, J.; Xu, S.; Zhou, Y.; Zhu, L.; Xiang, Y.; Xia, D. *New Journal of Chemistry* **2015**, *39*, 5750–5758.

(169) Cranston, R. R.; Lessard, B. H. *RSC Advances* **2021**, *11*, 21716–21737.

(170) Schünemann, C.; Elschner, C.; Levin, A.; Levichkova, M.; Leo, K.; Riede, M. *Thin Solid Films* **2011**, *519*, 3939–3945.

(171) Ghani, F.; Gojzewski, H.; Riegler, H. *Applied Surface Science* **2015**, *351*, 969–976.

(172) Gojzewski, H.; Ghani, F.; Szybowicz, M. *Materials Science-Poland* **2020**, *38*, 79–90.

(173) Iwatsu, F. *The Journal of Physical Chemistry* **1988**, *92*, 1678–1681.

(174) Roy, D.; Das, N. M.; Shakti, N.; Gupta, P. S. *RSC Advances* **2014**, *4*, 42514–42522.

(175) Bondarev, I. V.; Popescu, A.; Younts, R. A.; Hoffman, B.; McAfee, T.; Dougherty, D. B.; Gundogdu, K.; Ade, H. W. *Applied Physics Letters* **2016**, *109*, 213302.

(176) Gouterman, M. *Journal of Molecular Spectroscopy* **1961**, *6*, 138–163.

(177) Farag, A. A. M. *Optics & Laser Technology* **2007**, *39*, 728–732.

(178) Ghani, F.; Kristen, J.; Riegler, H. *Journal of Chemical & Engineering Data* **2012**, *57*, 439–449.

(179) Lucia, E. A.; Verderame, F. D. *The Journal of Chemical Physics* **1968**, *48*, 2674–2681.

(180) Caplins, B. W.; Mullenbach, T. K.; Holmes, R. J.; Blank, D. A. *Physical Chemistry Chemical Physics* **2016**, *18*, 11454–11459.

(181) Rosendo, E. d. P.; Yildiz, O.; Pisula, W.; Marszalek, T.; Blom, P. W. M.; Ramanan, C. *Physical Chemistry Chemical Physics* **2023**, *25*, 6847–6856.

(182) Yamanouchi, H.; Irie, K.; Saji, T. *Chemistry Letters* **2000**, *29*, 10–11.

(183) Kakade, S.; Ghosh, R.; Palit, D. K. *The Journal of Physical Chemistry C* **2012**, *116*, 15155–15166.

(184) Alonso, L.; Sampaio, R. N.; Souza, T. F. M.; Silva, R. C.; Neto, N. M. B.; Ribeiro, A. O.; Alonso, A.; Gonçalves, P. J. *Journal of Photochemistry and Photobiology B: Biology* **2016**, *161*, 100–107.

(185) Ha-Thi, M.-H.; Shafizadeh, N.; Poisson, L.; Soep, B. *The Journal of Physical Chemistry A* **2013**, *117*, 8111–8118.

(186) Yoshino, K.; Hikida, M.; Tatsuno, K.; Kaneto, K.; Inuishi, Y. *Journal of the Physical Society of Japan* **1973**, *34*, 441–445.

(187) Cruickshank, A. C.; Dotzler, C. J.; Din, S.; Heutz, S.; Toney, M. F.; Ryan, M. P. *Journal of the American Chemical Society* **2012**, *134*, 14302–14305.

(188) Ma, Y.-Z.; Xiao, K.; Shaw, R. W. *The Journal of Physical Chemistry C* **2012**, *116*, 21588–21593.

(189) ACS Guidelines for Bachelor's Degree Programs. `https://www.acs.org/education/policies/acs-approval-program/guidelines.html`.

(190) Hofstein, A.; Lunetta, V. N. *Science Education* **2004**, *88*, 28–54.

(191) Reid, N.; Shah, I. *Chem. Educ. Res. Pract.* **2007**, *8*, 172–185.

(192) Meester, M. A. M.; Maskill, R. *International Journal of Science Education* **1995**, *17*, 575–588.

(193) Wieman, C.; Holmes, N. G. *American Journal of Physics* **2015**, *83*, 972–978.

(194) Bruck, L. B.; Towns, M.; Bretz, S. L. *Journal of Chemical Education* **2010**, *87*, 1416–1424.

(195) Hawkes, S. J. *Journal of Chemical Education* **2004**, *81*, 1257.

(196) Kirschner, P.; Meester, M.; Middelbeek, E.; Hermans, H. *International Journal of Science Education* **1993**, *15*, 175–197.

(197) Shah, I. Making university laboratory work in chemistry more effective. PhD, University of Glasgow, 2004.

(198) Leachman, M.; Masterson, K.; Figueroa, E. *A Punishing Decade for School Funding*; 2017.

(199) Agustian, H. Y.; Seery, M. K. *Chemistry Education Research and Practice* **2017**, *18*, 518–532.

(200) Seery, M. K.; Agustian, H. Y.; Christiansen, F. V.; Gammelgaard, B.; Malm, R. H. *Chemistry Education Research and Practice* **2024**, *25*, 383–402.

(201) Isom, F. S.; Rowsey, R. E. *Journal of Research in Science Teaching* **1986**, *23*, 231–235.

(202) Davidowitz, B.; Rollnick, M.; Fakudze, C. *South African Journal of Chemistry* **2003**, *56*.

(203) Pogacnik, L.; Cigic, B. *Journal of Chemical Education* **2006**, *83*, 1094.

(204) Krathwohl, D. R. *Theory Into Practice* **2002**, *41*, 212–218.

(205) Thanh, B. N.; Vo, D. T. H.; Nhat, M. N.; Pham, T. T. T.; Trung, H. T.; Xuan, S. H. *Australasian Journal of Educational Technology* **2023**, *39*, 59–81.

(206) Scheidt, M.; Major, J.; Ge, J.; Godwin, A.; Chen, J.; Self, B.; Widmann, J.; Berger, E. Exploring the Relationship Between Non-Cognitive and Affective (NCA) Factors and First-Year Retention of Undergraduates in Engineering. 2019 IEEE Frontiers in Education Conference (FIE). 2019; pp 1–5, ISSN: 2377-634X.

(207) Geisinger, B. N.; Raman, D. R. *International Journal of Engineering Education* **2013**, *29*, 914–925.

(208) Galloway, K. R.; Bretz, S. L. *Journal of Chemical Education* **2015**, *92*, 1149–1158.

(209) Campbell, J.; Macey, A.; Chen, W.; Shah, U. V.; Brechtelsbauer, C. *Journal of Chemical Education* **2020**, *97*, 4001–4007.

(210) Jolley, D. F.; Wilson, S. R.; Kelso, C.; O'Brien, G.; Mason, C. E. *Journal of Chemical Education* **2016**, *93*, 1855–1862.

(211) Schmidt-McCormack, J. A.; Muniz, M. N.; Keuter, E. C.; Shaw, S. K.; Cole, R. S. *Chemistry Education Research and Practice* **2017**, *18*, 749–762.

(212) Lewis, R. A. *American Journal of Physics* **1995**, *63*, 468–470.

(213) Liu, X. *Journal of Science Education and Technology* **2006**, *15*, 89–100.

(214) Taibu, R.; Mataka, L.; Shekoyan, V. *International Journal of Education in Mathematics, Science and Technology* **2021**, *9*, 353–370.

(215) Burewicz, A.; Miranowicz, N. *Chemistry Education Research and Practice* **2006**, *7*, 1–12.

(216) Clark, T. M.; Chamberlain, J. M. *Journal of Chemical Education* **2014**, *91*, 1198–1202.

(217) Erdosne Toth, E.; Morrow, B. L.; Ludvico, L. R. *Innovative Higher Education* **2009**, *33*, 333–344.